Title
Network community-based analysis of complex vortical flows: Laminar and turbulent flows

Author
Gopalakrishnan Meena, Muralikrishnan

Publication Date
2020

Peer reviewed|Thesis/dissertation

UNIVERSITY OF CALIFORNIA
Los Angeles

Network community-based analysis of complex vortical flows: Laminar and turbulent flows

A dissertation submitted in partial satisfaction of the
requirements for the degree Doctor of Philosophy
in Mechanical Engineering

by

Muralikrishnan Gopalakrishnan Meena

2020

ABSTRACT OF THE DISSERTATION

Network community-based analysis of complex vortical flows:
Laminar and turbulent flows

by

Muralikrishnan Gopalakrishnan Meena
Doctor of Philosophy in Mechanical Engineering
University of California, Los Angeles, 2020
Professor Kunihiko Taira, Chair

The nonlinear interactions amongst vortical structures in fluid flows make their characterization and control a challenge, particularly in turbulence. In this work, a network (graph) community-based framework is introduced to formulate reduced-order models and perform flow-modification of complex laminar and turbulent vortical flows. The present framework represents the vortical interactions on a network, where the vortical elements are viewed as the nodes and the vortical interactions are regarded as edges weighted by induced velocity from the Biot–Savart law. This formulation enables the use of circulation and spatial arrangement of vortical elements for structure extraction from a flow field. The network-based community detection algorithm is used to identify closely interacting vortical elements, called communities. The methodology is used to extract communities of vortical elements in two- and three-dimensional flows, namely for a collection of discrete point vortices, laminar cylinder and airfoil wakes, and decaying two- and three-dimensional isotropic turbulence.

We introduce a community-based reduced-order modeling formulation to capture key interactions amongst coherent structures in high-dimensional unsteady vortical flows. The overall interaction-based physics of the high-dimensional flow field is distilled into the vortical community centroids, considerably reducing the system dimension. Taking advantage of the vortical interactions, the proposed methodology is applied to formulate reduced-order models for the inter-community dynamics of vortical flows and predict lift and drag forces on bodies

in wake flows. We demonstrate the capabilities of these models by accurately capturing the macroscopic dynamics of a collection of discrete point vortices, and the complex unsteady aerodynamic forces on a circular cylinder and an airfoil with a Gurney flap. The present formulation is found to be robust against simulated experimental noise and turbulence due to its integrating nature of the system reduction.

Furthermore, we show that the inter- and intra-community interactions can be used to identify the communities which have the strongest and weakest interactions amongst them. These vortical communities are referred to as the connector and peripheral communities, respectively. We demonstrate the influence of the network-based structures to modify the dynamics of a collection of discrete point vortices. Taking advantage of the strong inter-community interactions, connector community can significantly modify the collective dynamics of vortices through the application of multiple impulse perturbations. We then apply the community-based framework to extract influential structures in isotropic turbulence. The connector and peripheral communities extracted from turbulent flows resemble shear-layer and vortex-core like structures, respectively. The influence of the connector structures on the flow field and their neighboring vortical structures is analyzed by adding impulse perturbations to the connectors in direct numerical simulations. The findings are compared with the cases of perturbing the strongest vortex tube and shear-layer regions. We find that perturbing the connector structures enhances local turbulent mixing beyond what are achieved by the other cases.

The dissertation of Muralikrishnan Gopalakrishnan Meena is approved.

Jeffrey D. Eldredge

Hossein Pirouz Kavehpour

James C. McWilliams

Kunihiko Taira, Committee Chair

University of California, Los Angeles

2020

To Amma, Achan and Nanu.

TABLE OF CONTENTS

LIST OF FIGURES

ACKNOWLEDGMENTS

I am immensely thankful to my mentor, Professor Kunihiko Taira, for supporting me through this great endeavor in my life. My perseverance to complete this study would not have been possible without his tenacious guidance and patience. I will always be in debt to him for giving me this once in a lifetime opportunity and guiding me to be an independent researcher. I am honored to call him my *guru*. I believe that a student's excellence and contributions to society are a personification of the *guru*'s virtue. I sincerely hope that my contributions to the scientific world do justice to his pioneering work as a researcher and mentor.

I thank my committee members Professors Jeff Eldredge, Pirouz Kavehpour, and James McWilliams, for encouraging me and giving insightful suggestions to strengthen the outcome of this work. I sincerely appreciate the support from Professors Eldredge and Kavehpour through my transition to UCLA. The discussions I had with Professor McWilliams on turbulent flows have been very helpful for this work and inspirational for me to pursue various aspects of the field in my career. Furthermore, I wish to show my gratitude to Professors Rajan Kumar, Farrukh Alvi, and Louis Cattafesta at Florida State University for their guidance and support, which have been important for my progress through these years. I would also like to mention my gratitude to my undergraduate mentor, Mr. Madhu Anantharajan, who inspired me to pursue a career in fluid mechanics.

I am thankful to the US Army Research Office (Grant: W911NF-17-1-0118 and W911NF-19-1-0032, Program Manager: Dr. Matthew Munson), the National Science Foundation (Grant number: 1632003, Program Manager: Drs. Dimitrios V. Papavassiliou and Ronald D. Joslin), and the Air Force Office of Scientific Research (Grant number: FA9550-16-1-0650, Program Manager: Dr. Douglas R. Smith) for supporting this work. I would like to extend my regards to Professors Steven L. Brunton and Keisuke Asai, and Dr. Zhe Bai for fruitful collaborations and discussions. I am grateful to my physical therapists, Tyressa Judge (FSU) and Aggie Postman Kuchta (UCLA), for helping me through the various physical challenges.

My life and research work at UCLA and FSU have been made more exciting and fun by my lab mates. I have had the distinguished honor to work with various people in the lab,

who are pioneering in their own field of expertise. I wish to express my deepest gratitude to Drs. Aditya Nair, Chi-An Yeh, Yiyang Sun, Qiong Liu, and Kai Zhang for their invaluable advice inside and outside the lab and the everlasting bond as my academic elder brothers and sisters. I would also like to sincerely thank my other labmates as well, a few of them to particularly mention are Dr. Phillip Munday, Dr. Byungjin An, Jean Helder Marques Ribeiro, Dr. Calum Skene, Vedasri Godavarthi, and Tulio Rodarte Ricciardi. I thank all my colleagues and staff members at UCLA MAE and FSU AME for the wonderful discussions and support, which also played a pivotal role in my progress in graduate studies.

My life in the U.S. would not have been fun and fruitful without my friends. I thank Aditya, Roya, Abiola, Supadha, Harsha, and Harsh for being partners in the various eventful times. Finally, I am in debt to my family for being there for me through these challenging years. I thank my partner, Dr. Mojgan Aghakhanloo (Moju), for her love and support through the difficult times. I look forward to an adventurous life ahead with Moju, who made me see life and work in an invigorating perspective. I extend my deepest thanks to my brother, Gopikrishnan (Nanu), who has always had my back. He is the one who motivated and inspired me to pursue a career in science, dating back to our backyard experiments when we were young. My parents, Meena (Amma) and Gopalakrishnan (Achan) have been perennial to my story and success, and I reserve my final words for them. For teaching me to strive hard for attaining anything in life, the value of having principles in life, trying to do the right and be a good human being, and most of all their sacrifices, they require my deepest acknowledgment for whichever heights I reach. I thank God for having these wonderful people in my life!

VITA

2014 Bachelor of Technology (Mechanical Engineering), Cochin University of Science and Technology, India.

2018 Master of Science (Mechanical Engineering), Florida State University, U.S.A.

2015–2018 Graduate Research Assistant, Mechanical Engineering Department, Florida State University.

2019–present Graduate Research Assistant, Department of Mechanical and Aerospace Engineering, University of California, Los Angeles.

JOURNAL PUBLICATIONS

2018 M. Gopalakrishnan Meena, K. Taira, and K. Asai, "Airfoil wake modification with Gurney flap at low-Reynolds number", AIAA Journal, 56(4), 1348-1359.

2018 M. Gopalakrishnan Meena, A. G. Nair, and K. Taira, "Network community-based model reduction for vortical flows", Physical Review E, 97, 063103.

2019 Z. Bai, N. B. Erichson, M. Gopalakrishnan Meena, K. Taira, and S. L. Brunton, "Randomized methods to characterize large-scale vortical flow network", PLOS One, 14(11), e0225265 (*Parts of this work was motivated from the current dissertation*).

2020 M. Gopalakrishnan Meena and K. Taira, "Identifying vortical network connectors for turbulent flow modification", *in review.*

CONFERENCE PUBLICATIONS & PRESENTATIONS

2017 M. Gopalakrishnan Meena, K. Taira, and K. Asai, "Low Reynolds number wake modification using a Gurney flap," 55th AIAA Aerospace Sciences Meeting, Grapevine, TX, Jan. 9-13 (AIAA 2017-0543).

M. Gopalakrishnan Meena, K. Taira, and K. Asai, "Low Reynolds number wake modification using a Gurney flap," 55th AIAA SciTech, Grapevine, TX, Jan. 9-13.

M. Gopalakrishnan Meena, A. G. Nair, and K. Taira, "Network representation and analysis of bluff body wake," SIAM Conference on Computational Science and Engineering, Atlanta, GA, Feb. 27-Mar. 3.

M. Gopalakrishnan Meena, A. G. Nair, and K. Taira, "Vortex network community based reduced-order force model," 70th Annual Meeting of the APS Division of Fluid Dynamics, Denver, CO, Nov. 19-21.

2018 *M. Gopalakrishnan Meena and K. Taira, "High-dimensional turbulence network characterization and modeling", NetSci Conference, Paris, France, June 13-15.*

2019 M. Gopalakrishnan Meena and K. Taira, "Characterizing influential networked structures in isotropic turbulence," 11th International Symposium on Turbulence and Shear Flow Phenomena, Southampton, UK, July 30 - Aug. 2 (TSFP 11 235).

M. Gopalakrishnan Meena and K. Taira, "Characterizing three-dimensional homogenous isotropic turbulence network", SoCal Fluids XIII, UC Santa Barbara, April 20.

M. Gopalakrishnan Meena and K. Taira, "Characterizing influential networked structures in isotropic turbulence," 11th International Symposium on Turbulence and Shear Flow Phenomena, Southampton, UK, July 30 - Aug. 2.

M. Gopalakrishnan Meena and K. Taira, "Network-based identification of influential structures to modify turbulent flows," 72th Annual Meeting of the APS Division of Fluid Dynamics, Seattle, WA, Nov. 23-26.

CHAPTER 1

Introduction

1.1 Motivation

Analysis of turbulence remains as one of the most complex problems in science and engineering due to the strong nonlinear dynamics and multi-scale properties of fluid flows [59]. As turbulence is ubiquitous in nature and engineering problems, the modification of its dynamics has been an active field of study [20]. For modeling and controlling their dynamics, it is important to understand the interactions amongst the vortical structures. Insights from such endeavors can support applications including flow separation control [13] and mixing enhancement [126]. What makes this control problem challenging is that a large amount of energy is generally required to modify large-scale vortical structures to achieve flow modification.

To achieve flow modification with low level of energy input, it is critical to identify important vortical structures in the flow. Various techniques have been introduced to extract flow structures. Reduced representation of the flow field using approaches such as the proper orthogonal decomposition (POD; [83]) and dynamic mode decomposition (DMD; [122]), are tools which have shown great ability to extract the dominant features of the flow [129, 132]. Measures like Q-criterion [57], λ_2-criterion [64], Γ-criterion [43], and finite-time Lyapunov exponent [50, 51], can be used to identify highly rotational and strained regions of the flow [31, 22]. Recently, machine learning inspired methods have also been used to extract the dominant vortical structures in turbulence [65].

Even with the available strategies to identify coherent structures, the quantification and analysis of vortical interactions is a challenge as every element in the flow field interact with

others. If the given flow field is spatially discretized into n discrete cells, the number of interactions amongst the cells to be accounted for will be $n(n-1)$. This is particularly crucial in turbulence with high dimensions. The field of network science has paved the way for analyzing complex interactions amongst a set of connected elements [16, 99, 9]. Theoretical and computational tool-sets developed in this field have inspired in-depth studies on the structural and dynamical characteristics of various networks, including biological, social, transportation, information, and power-grid networks [140, 127, 111, 1]. In general, these networks have well-defined graph structures comprised of sets of discrete nodes. With such graph structure at hand, graph theory, linear algebra, data science, dynamical systems theory, and control theory can be applied in harmony to study complex networked dynamics [15, 106]. For example, one can examine problems such as disease and information transmission on social networks [119], and development of cyber-security strategies for combating attacks on the world wide web, while maintaining key connectivity [2, 30].

Complex interactions prevalent in fluid flows also exhibit great richness in their dynamics, as seen in unsteady vortical and turbulent flows. Nonetheless, the application of network-theoretic techniques on the analysis of fluid flows remains fairly limited. One of the major challenges in extending network analysis to fluid flows is the extraction of the underlying network structure that can appropriately describe their high-dimensional kinematics and dynamics. In recent years, network formulations have been introduced to quantify and capture the interactions in fluid flows. The induced velocity among vortical elements [94], Lagrangian motion of fluid elements [124, 49], oscillator-based representation of the energy fluctuations [93], time series of fluid flow properties [120], and triadic interactions in turbulence [46] have been studied using a network-theoretic framework. The formulations have been extended to characterize various turbulent flows, including two-dimensional isotropic turbulence [133], turbulent premixed flames and combustors [125, 37, 76], wall turbulence [62], mixing in turbulent channel flow [60, 61], and isotropic magnetohydrodynamic turbulence [47, 48].

Various network-based clustering techniques have been used in the past to extract closely connected nodes. Community detection of networks has received attention in various data-rich fields [103, 90, 34]. Aggregating nodes of a network with high density of intra-group

interactions into communities has a lot of implications in reduction of system complexity. Each community or cluster can then be utilized to describe characteristics of the global system [135]. In the field of fluid mechanics, image sequences have been used to reconstruct the flow field using the Frobenius–Perron operator and community detection is implemented to identify key structures in the phase space [17]. In another work, spectral clustering has been considered for vortex detection in a Lagrangian-based framework of fluid flow networks [49]. A coherent structure coloring technique also builds on a Lagrangian framework to identify coherent structures in complex flows [121, 58]. The methodology presented in the current work complements these efforts in extracting communities in fluid flows from the underlying vortical connectivity structure, instead of fluid trajectories. The current work does not strive towards an alternative definition for identifying a vortex.

The characterization of interactions among the vortical elements is challenging due to the high-dimensional nature of system. Thus, there is a need to reduce the dimension of the system, while preserving the overall interaction structure and dynamics. In the present work, we reduce the order of a complex nonlinear system, particularly of unsteady wake flows, by identifying communities in the fluid flow network representing interactions amongst the vortical elements [38]. Furthermore, we model their dynamical characteristics and other system outputs in a computationally tractable manner. In a recent work, we have utilized randomized linear algebraic techniques to form reduced dimensional representation and measures of the vortical network [7], further extending the dimension reduction endeavor. While several works in literature take advantage of the community structure to describe system behavior like evolving networks and mobility models [137, 92], studies focusing on a community-based reduced-order formulation to describe the dynamics and other outputs of a system are limited in literature and the fluid mechanics community.

Moreover, a key attribute missing in clustering approaches is to take advantage of the inter- and intra-cluster interactions to identify the important interactions and clusters in the flow. Moreover, modifying the system dynamics by taking advantage of the interactions amongst the clusters have not yet been explored. In the present study, we use the intra- and inter-cluster interactions extracted from a network-based framework for identify-

ing important flow-modifying vortical structures. We use the community detection algorithm [38] to extract closely connected vortical elements in two- and three-dimensional isotropic turbulence. The interactions amongst the communities are used to identify key turbulent flow-modifying structures [39, 40]. The goal of this network-based framework is not to alter the global turbulent flow, but to influence certain key vortical structures in the complex background of isotropic turbulence.

An alternate approach for system order reduction and imposing control of complex dynamical systems considers discretizing the phase-space through clustering. Recently, clustering and deflation operations have been performed to capture flipping dynamics in mixing layers [70, 95] and turbulent shear flows [123]. These approaches are founded on analyzing time-series data. This differs from the current approach where network-based physical structures (communities) are extracted and low-dimensional models are deduced based on these communities. Furthermore, the interactions amongst the communities are evaluated to identify key flow modifying structures. In the current work, the community detection procedure focuses on extracting coherent structures in vortical flows purely from specification of a network representing physical interactions between vortical elements. The use of network theory and community-based concepts to describe the complex nature of fluid flows is novel and attractive, especially since they can capture the interactive dynamics and lead to models that are amicable to preserving key interactions in a reduced order manner. While the present work discusses the formulation in the context of vortical flows, the overall approach is applicable to a wide range of networked dynamics and continuum mechanics problems.

1.2 Overview

An overview of the community-based analysis, illustrated using to a model point-vortex problem, is presented in figure 1.1. In what follows, we first introduce the network representation of vortical interactions in section 2.1. We introduce the network-based measures of node strength and community detection to identify closely connected nodes in sections 2.2 and 2.3, respectively. The network-based measures are demonstrated in a model fluid flow

problem of ideal point-vortex dynamics. We discuss the general approach for the community-based dimension reduction of networked systems in section 2.3.1. We describe the procedure for modeling the overall networked dynamics of the system and predicting observable (auxiliary) variables of the system. We then introduce the intra- and inter-community interaction strengths to identify important flow modifying nodes in section 2.3.2. We demonstrate the community-based framework for modeling and modifying vortical flows in chapter 3. With a reduced community-based representation of the vortical flows, we develop a nonlinear reduced-order model to predict the overall dynamics of the communities and the aerodynamic forces, which are described in section 3.1. We demonstrate the capability of the present community-based reduced-order model using canonical two-dimensional vortical flows and discuss its robustness against perturbations in the flow field data. The influence of the extracted nodes to modify the dynamics of a collection of discrete point vortices is assessed in section 3.2.1. We then employ the community-based formulation to extract influential structures in two- and three-dimensional isotropic turbulence, described in section 3.2.2. The vortical network of two- and three-dimensional isotropic turbulence is characterized. We then demonstrate the use of community-based influential structures to modify the turbulent flows. Finally, concluding remarks and future works for the present formulations are provided in chapter 4.

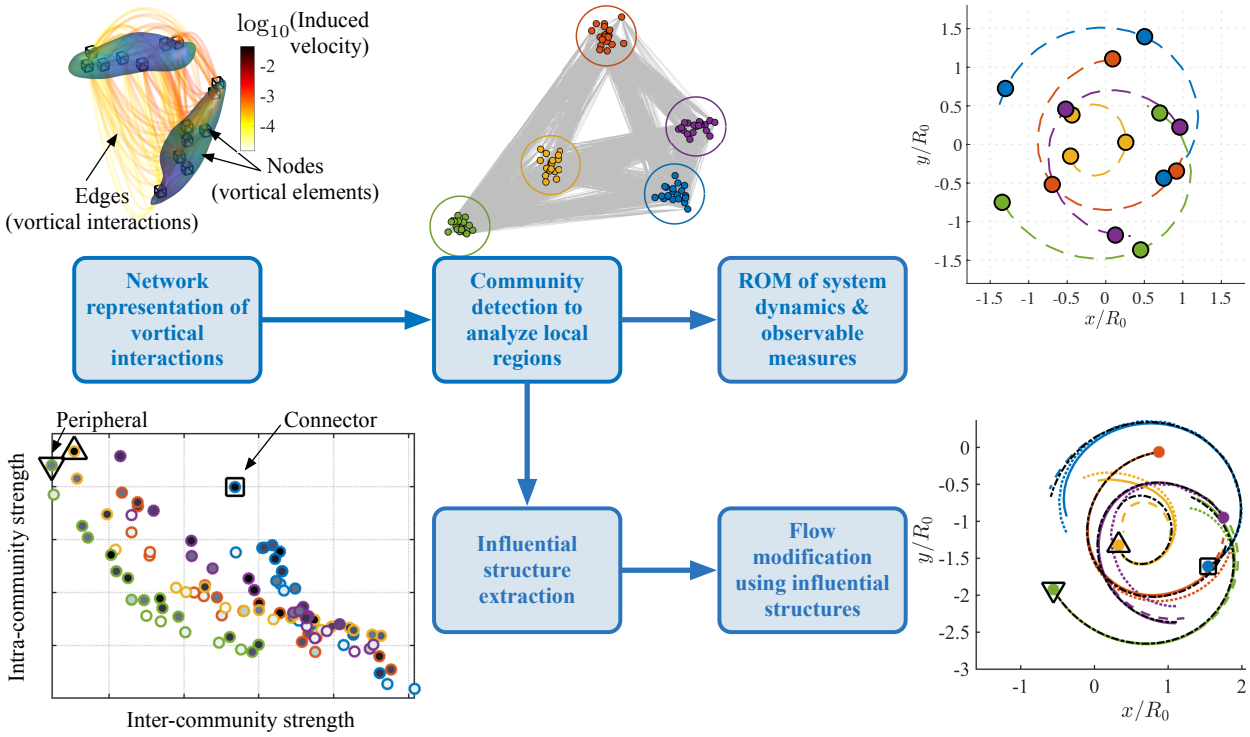

Figure 1.1: An overview of the community-based procedure for reduced-order modeling and flow modification.

CHAPTER 2

Theory and methods

Fluid flows pose one of the most nonlinear, multi-scale phenomena in nature. The Navier–Stokes equations that describe the high-dimensional dynamics of incompressible flows are

$$\boldsymbol{u}_t + \boldsymbol{u} \cdot \nabla \boldsymbol{u} = -\nabla p + Re^{-1} \nabla^2 \boldsymbol{u}, \tag{2.1}$$

$$\nabla \cdot \boldsymbol{u} = 0, \tag{2.2}$$

where $\boldsymbol{u}$ represents the velocity, p denotes the pressure, and Re is the Reynolds number. The above formulation can be equivalently represented for the vorticity field $\boldsymbol{\omega} = \nabla \times \boldsymbol{u}$ with

$$\boldsymbol{\omega}_t + \boldsymbol{u} \cdot \nabla \boldsymbol{\omega} = \boldsymbol{\omega} \cdot \nabla \boldsymbol{u} + Re^{-1} \nabla^2 \boldsymbol{\omega}. \tag{2.3}$$

As the vorticity field describes unsteady motion of fluid flows, we take the viewpoint that key flow features are represented as vortical elements in the present study and examine the interactions among the vortical elements.

We discretize the vorticity field in a Lagrangian and Eulerian perspective. The discrete vortical elements are referred to as nodes in the present work. To quantify the interactions amongst the vortical nodes, we consider the induced velocity imposed upon each other. The Biot–Savart law provides the induced velocity from a vortical element as a function of circulation and relative position of the vortical elements, expressed as

$$\boldsymbol{u}(\boldsymbol{r}, t) = \frac{1}{2(n_\mathrm{d} - 1)\pi} \int_V \frac{\boldsymbol{\omega}(\boldsymbol{r}', t) \times (\boldsymbol{r} - \boldsymbol{r}')}{\|\boldsymbol{r} - \boldsymbol{r}'\|_2^{n_\mathrm{d}}} \mathrm{d}V', \tag{2.4}$$

where $\boldsymbol{u}(\boldsymbol{r}, t)$ is the induced velocity at location $\boldsymbol{r}$ in the domain from a collection of vortical

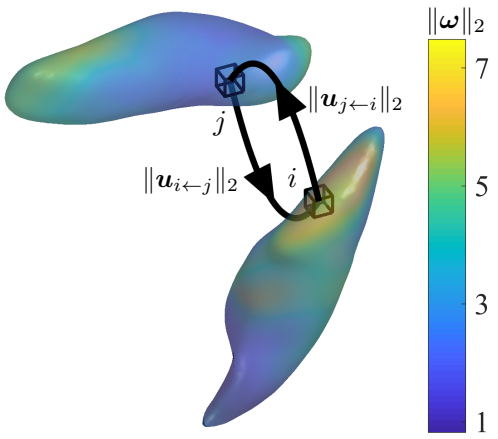

Figure 2.1: Interactions between two vortical elements in vortical structures extracted from three-dimensional isotropic turbulent flow. The vortical structures are visualized by isosurface of Q-criterion [57] coloured with $\|\boldsymbol{\omega}\|_2$. The vortical elements are shown for the spatial grid cells.

elements enclosed in volume V with a vorticity distribution of $\boldsymbol{\omega}(\boldsymbol{r}', t)$ at positions $\boldsymbol{r}'$. Here, n_d is the spatial dimension of the flow field. Furthermore, the influence of a vortical node (element) i on node j can be written as

$$\boldsymbol{u}_{j\leftarrow i} = \frac{\Gamma_i \mathrm{d}l}{2(n_\mathrm{d}-1)\pi} \frac{\sin\theta}{\|\boldsymbol{r}_j - \boldsymbol{r}_i\|_2^{n_\mathrm{d}-1}}, \tag{2.5}$$

where $\Gamma = \|\boldsymbol{\omega}(\boldsymbol{r}, t)\|_2 \mathrm{d}S$ is the circulation of a vortical element of area $\mathrm{d}S$ and length $\mathrm{d}l$, and θ is the angle between the vorticity and distance vectors. As an example, we illustrate the interactions between two vortical nodes in figure 2.1. Here, element i has higher vorticity magnitude compared to element j. Thus, the velocity induced by i onto j is higher than that imposed by j onto i, yielding an asymmetric interaction.

2.1 Network theoretic description of vortical interactions

The Navier–Stokes equations governing the dynamics of the vortical elements in a flow are complex to solve due to the presence of the nonlinear terms, requiring a full computational fluid dynamics solver [71]. Resolving the full dynamics through numerical as well as experimental methods requires resources and sometimes pose major challenges, especially when

the Reynolds number is high, giving rise to turbulence. Furthermore, characterizing the interaction-based behavior of vortical elements can be a challenge in high-Reynolds number turbulence, particularly with high degrees of freedom needed to discretize the flows. To facilitate the analysis of high-dimensional dynamics, we leverage the analytical approaches in graph theory [16] and network science [104]. Here, we establish a network-theoretic representation of the vortical interactions in a flow field. We construct a network (graph) $\mathscr{G}$ comprised of vortical nodes $\mathscr{V}$ connected by edges $\mathscr{E}$ holding edge weights $\mathscr{W}$ based on induced velocity. Given this definition $\mathscr{G} = \mathscr{G}(\mathscr{V}, \mathscr{E}, \mathscr{W})$ for the network, we can quantify the important nodes in vortical flows.

Vortical elements on the network can be described through a Lagrangian or Eulerian perspective as shown in figure 2.2. In the Lagrangian description, the vortical elements are approximated using a collection of discrete point vortices (line vortices). The motion of the vortical structures can be captured by modeling the dynamics of these point vortices. The number of nodes depend on the number of point vortices used to discretize the vortical structures in the flow field. The strength of each point vortex is given by the circulation corresponding to the local area covered by the point vortex while discretizing the vortical structure.

A continuous representation of the flow field can also adopt an Eulerian description, where Cartesian discretization of the flow with vortical elements within the grids correspond to nodes of the network, as shown in figure 2.2. The vortical elements within each grid cell keep changing with time according to the flow dynamics. The circulation over the grid cell is used as the circulation of the node. To highlight the generality of our current approach, we include discussions on both network formulations in sections 3.1 and 3.2. Furthermore, the demonstration of the current methodology for both Lagrangian and Eulerian description of flow fields extends the applicability of fluid trajectory-based vortex identification methods [49, 121] to formulate reduced-order models and extract influential structures.

In the current method, a snapshot of the velocity or vorticity field of any incompressible fluid flow problem is solely required to represent the flow field in the above network formulation, as shown in figure 2.2. We have observed that the inviscid approximation of

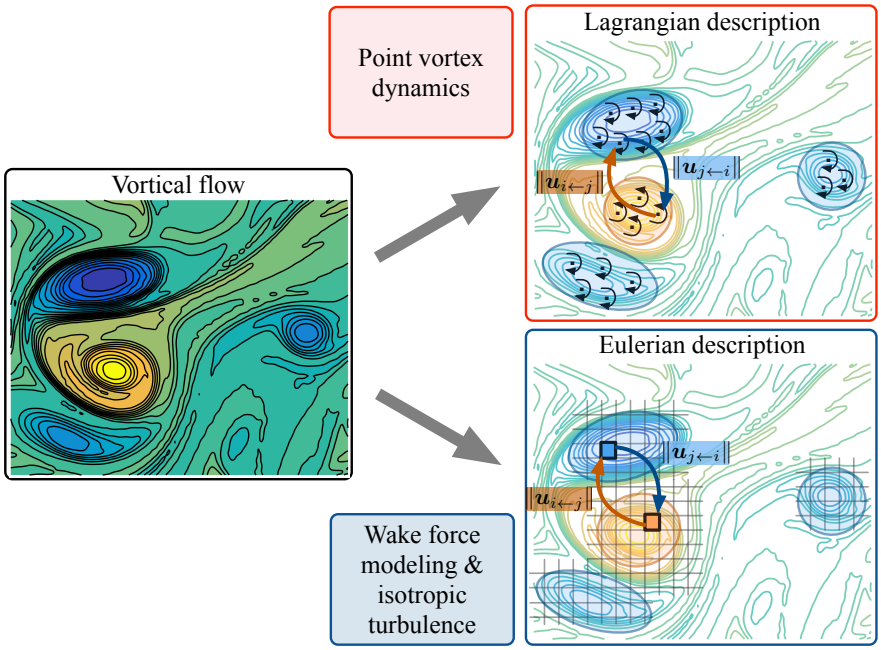

Figure 2.2: Lagrangian and Eulerian network descriptions of a flow field. Nodes (discrete point vortices and Cartesian cells) and edges (magnitude of induced velocity $\|\boldsymbol{u}_{j\leftarrow i}\|$) of the vortical network in each descriptions are also shown.

the Biot–Savart law is able to capture the interaction physics in viscous flows effectively through this network definition [94, 133]. Also, the network representations of time series of snapshots can describe the time evolution of interactions among the vortical structures.

The collection of connectivity amongst the nodes can be represented by the adjacency matrix $\boldsymbol{A}$, which holds the edge weights as its elements. For the vortical interaction network, $\boldsymbol{A}$ can be defined using the normalized induced velocity [94, 133] as

$$A_{ij} = \frac{\|\boldsymbol{u}_{i\leftarrow j}\|_2}{u^*}, \tag{2.6}$$

where u^* is a characteristic velocity of the flow. For a flow field with n vortical nodes, the adjacency matrix $\boldsymbol{A} \in \mathbb{R}^{n\times n}$. The above formulation gives an asymmetric adjacency matrix, representing a directed network. Adding directions to the links helps differentiate between the influential and influenced nodes. Non-dimensionalization is important for the analysis of turbulent flows over a range of Reynolds number. The details of the non-dimensionalization will be discussed in section 3.2.2.1.

Let us discuss the role of $\boldsymbol{A}$ on network dynamics and appropriate measures to identify influential nodes. Consider a general dynamical system for n state vectors $\boldsymbol{x}_i \in \mathbb{R}^{p_\mathrm{v}}$ holding p_v variables over a network. The general interaction-based dynamics of the elements can be expressed as

$$\dot{\boldsymbol{x}}_i = \boldsymbol{f}(\boldsymbol{x}_i) + \sum_{j=1}^{n} A_{ij}\boldsymbol{g}(\boldsymbol{x}_i, \boldsymbol{x}_j), \quad i = 1, 2, \ldots, n, \tag{2.7}$$

where function $\boldsymbol{f}(\boldsymbol{x}_i)$ represents the intrinsic dynamics of node i and function $\boldsymbol{g}(\boldsymbol{x}_i, \boldsymbol{x}_j)$ describes the interactive dynamics between nodes i and j. We consider the model fluid flow problem of ideal point-vortex dynamics [5, 108] to demonstrate the interaction-based dynamics of vortical elements and identify important vortical nodes using the network-based approach.

Let us take a collection of $n = 100$ discrete point vortices, initialized on an infinite two-dimensional domain as shown in figure 2.3. These vortices are arranged into five groups at the initial time. The vortices are coloured by their circulations Γ_i, which is kept constant over time in the inviscid flow. The circulations have a normal distribution about a mean of $\overline{\Gamma} = 0.1$ and a standard deviation of $\sigma_\Gamma = 0.008$. This canonical model problem portrays the nonlinear dynamics of vortical structures found in various flows [94]. The transparent gray edges visualize all interactions amongst the nodes, based on equation 2.6. Here, we use $u^* = \Gamma_\mathrm{tot}/(2\pi R_0)$ where $\Gamma_\mathrm{tot} = \sum_i^n \Gamma_i$ is the total circulation of the system and R_0 is the average radial distance of the centroid of the clusters from the geometric center of the overall system at initial condition. The spatial variables are non-dimensionalized by R_0. The Biot–Savart law governs the dynamics of the point vortices, which can be expressed in terms of equation 2.7 for which $\boldsymbol{f}(\boldsymbol{r}_i) = 0$ and $\boldsymbol{g}(\boldsymbol{r}_i, \boldsymbol{r}_j) = u^*\hat{\boldsymbol{k}} \times (\boldsymbol{r}_i - \boldsymbol{r}_j)/\|\boldsymbol{r}_i - \boldsymbol{r}_j\|_2$. Here, $\hat{\boldsymbol{k}}$ is the out-of-plane unit normal vector. We use this dynamical systems example to demonstrate the evaluation of important network measures pertinent to the interactive dynamics of the vortical elements.

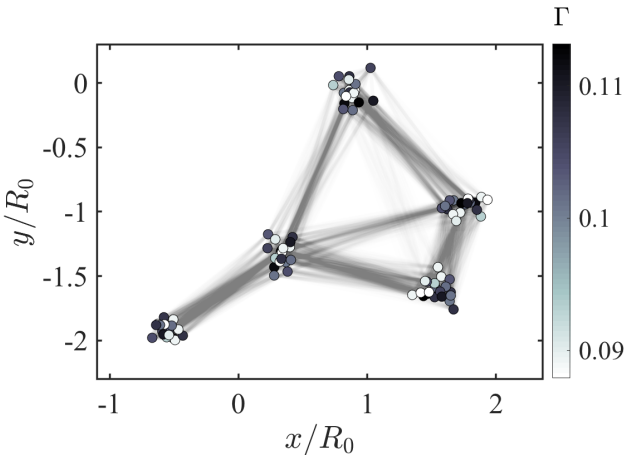

Figure 2.3: A collection of discrete point vortices. The gray shade represents their circulation. The gray lines denote the web of interactions amongst them, with the transparency indicating the normalized magnitude of induced velocity.

2.2 Node strength

The node strength measures the ability of a node to be influential (out-strength) or be influenced (in-strength) in the network. The out- and in-strengths of a node are defined by

$$s_i^{\text{out}} = \sum_j A_{ji} \quad \text{and} \quad s_i^{\text{in}} = \sum_j A_{ij}, \tag{2.8}$$

respectively. These measures are useful to identify the node with collection of significant connections in a network.

For the vortical networks, the present definition of edge weight from equation 2.6 is based on the out-strength. Herein, the node strength, s_i, is taken to be the out-strength, unless specified. A relation between the node strength and enstrophy $\Omega(\boldsymbol{r}, t)$ of a vortical element can be obtained using equation 2.5 as

$$s_i = \frac{\Gamma_i \mathrm{d}l}{2(n_\mathrm{d}-1)\pi} \sum_j \frac{\sin\theta}{\|\boldsymbol{r}_j - \boldsymbol{r}_i\|_2^{n_\mathrm{d}-1}} = \frac{C}{2(n_\mathrm{d}-1)\pi} \sqrt{\Omega_i} \mathrm{d}V, \tag{2.9}$$

where the sum of distance components C is constant in a fully periodic domain or can be inferred given the location of the nodes. This relationship reveals that $s_i \propto \sqrt{\Omega_i}$. This is particularly useful to determine the node strength distribution $p(s)$ of a vortical network.

The distribution is dependent on the enstrophy distribution $p(\Omega)$. The latter is usually a known or measurable flow statistics. The relation applied to an analytical vortex solution is shown in Appendix A. Distribution $p(s)$ gives a global picture of the nature of connectivity in the network and is used to identify the type of the network [9]. The distribution is also useful to identify nodes with high s, which is referred to as the hub nodes. These nodes have been found to be important to assess the robustness of the network dynamics against random and targeted perturbations [2, 133].

2.3 Community detection

Identifying closely connected vortical nodes is important towards revealing key local groups on the network. Such modular groups of nodes with high connectivity amongst each other are referred to as communities [107, 101, 103]. In the discussion herein, a network community is considered as a group of nodes that are strongly connected and behave collectively in a dynamically similar manner. Nodes in a particular community interact in a similar manner compared to the rest of the nodes or communities in the network. One approach to find the communities is to measure the overall modular nature of a network using modularity. Modularity is a measure representing the difference between the fraction of edges within a community and the expected value for a randomly generated network with same size and degree distribution. Modularity M for a directed network given by [79]

$$M = \frac{1}{2n_\mathrm{e}} \sum_{ij} \left[A_{ij} - \gamma_\mathrm{M} \frac{s_i^\mathrm{in} s_j^\mathrm{out}}{2n_\mathrm{e}} \right] \delta(c_i, c_j), \tag{2.10}$$

where n_e is the total number of edges in the network, γ_M is the modularity resolution parameter to weigh the presence of small or large communities in the network [115, 35], $\delta(c_i, c_j)$ is the Kronecker delta, $c_i \in \hat{C}_k$ is the label of the community to which element i is assigned and $\hat{C}_k$ is the set of k-th network community. Here, $k = 1, 2, \ldots, m$, with m being the total number of communities. Higher positive values of modularity indicate more edges within communities than what is expected on the basis of chance, portraying a high modu-

lar structure of the network. Thus, the communities can be identified by maximizing M by regrouping the nodes. Here, the number of communities m is unspecified and determined by the algorithm. Various algorithms are available to identify the communities in a network [34]. In the present study, we adopt the method by Blondel *et al.* [14] to identify the communities in large vortical networks with accuracy and low computational cost [34]. We herein refer to these network communities on vortical networks as the vortical communities [38]. Also, for vortical flows, γ_{M} can be set based on the plateau effect on the number of vortical communities identified with change in γ_{M} for a given Reynolds number. Note that community detection defers from graph partitioning [104]. While modularity maximization is only one of the techniques to perform community detection, other techniques such as using eigenvectors of matrices, spectral methods, and using random walks [102, 105, 113, 139] can be applied to detect community structure depending on the problem at hand.

The extraction of vortical elements behaving or interacting in similar manner to form a vortex structure or cluster can be defined as a vortical community from a network-theoretic perspective. Although these communities are key flow features, important in capturing the interactions that govern the vortical flow dynamics, we do not propose the current methodology as an alternative definition for identifying a vortex. In this study, the definition of a vortical community need not necessarily align with the definition of a vortex in the fluid dynamics literature, since the present objective is to construct a network-based reduced dynamical model and extract influential regions of the flow. The Biot–Savart law used to describe the interaction physics can be applied to any fluid flow in general, provided it is used to describe the induced velocity among vortical structures kinematically. This physical interaction-based definition of the network supplements the properties of the community detection methodology to define a networked structure in the fluid flow system. This might be limited when using other graph partitioning techniques [49, 121] based on fluid trajectories to extract the vortical structures.

2.3.1 Community-based reduced order modelling

For many problems, networks are comprised of a large number of nodes (i.e., $n \gg 1$). The analysis, simulation, and modeling of dynamics on such large networks requires significant computational resources and calls for techniques to reduce the computational complexity of the problem, while retaining the essence of the key physics. In the present approach, we classify the nodes into network communities based on the adjacency matrix A and reduce the state dynamics of the overall system to the community-based (centroid-based) dynamics.

We illustrate the overall procedure of the present community-based model reduction technique in figure 2.4. Let us consider an aggregate state vector $\boldsymbol{x}$ comprised of the state vectors from all nodes $\{\boldsymbol{x}_i\}_{i=1}^n$:

$$\boldsymbol{x} \equiv \begin{pmatrix} \boldsymbol{x}_1 \\ \boldsymbol{x}_2 \\ \vdots \\ \boldsymbol{x}_n \end{pmatrix} \in \mathbb{R}^{n_{\mathrm{P}}}. \tag{2.11}$$

With the network communities identified, we can order the above aggregate state variable to sort the entries based on the communities to which they belong. It is possible to construct a permutation matrix P equivalently that would take the left vector $\boldsymbol{x}$ to the middle vector $P\boldsymbol{x}$ in figure 2.4. The main objective here is to determine the reduced graph $\tilde{\mathscr{G}}$ representing the interactions amongst the communities.

With the elements of $\boldsymbol{x}$ grouped into respective communities, we can reduce the state variables of each communities to their respective centroids. That is, we define a centroid of community k based on an appropriate weighing variable of the system, κ_i,

$$\boldsymbol{\xi}_k \equiv \frac{\sum_{i \in C_k} \kappa_i \boldsymbol{x}_i}{\sum_{i \in C_k} \kappa_i}, \quad k = 1, 2, \ldots, m, \tag{2.12}$$

where $m \ll n$. Accordingly, we can define an aggregate community centroid-based state

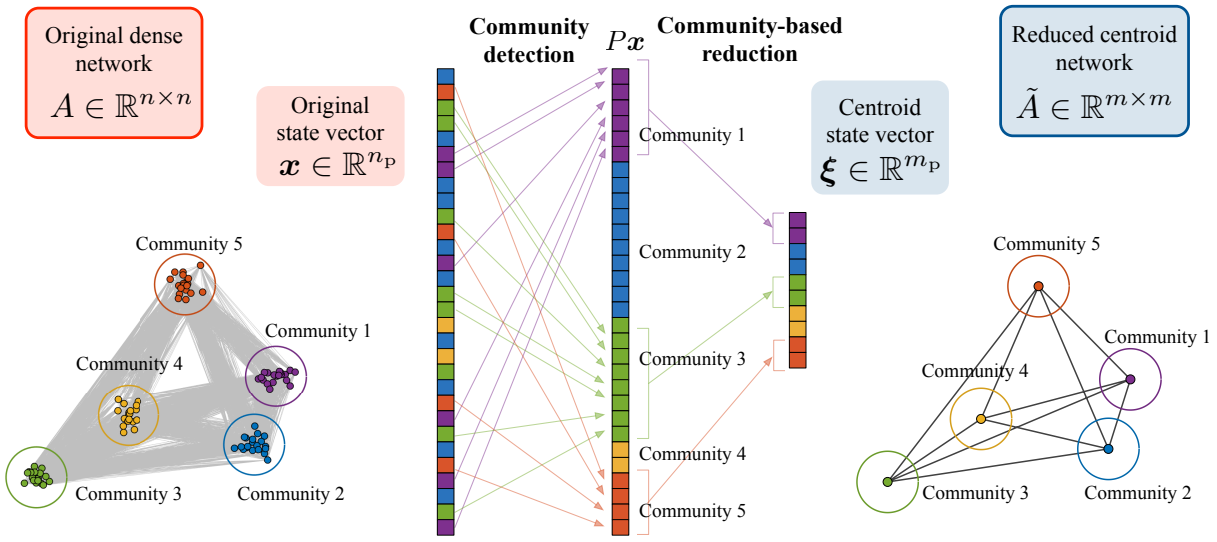

Figure 2.4: Overview of the community-based reduction of a networked dynamical system.

vector $\boldsymbol{\xi}$

$$\boldsymbol{\xi} \equiv \begin{pmatrix} \boldsymbol{\xi}_1 \\ \boldsymbol{\xi}_2 \\ \vdots \\ \boldsymbol{\xi}_m \end{pmatrix} \in \mathbb{R}^{m_\mathrm{P}}, \tag{2.13}$$

which is reduced from $P\boldsymbol{x}$ in figure 2.4. We now intend to capture the overall dynamics of the system by tracking the community centroids in a macroscopic manner, instead of being concerned of each and every member of the community.

Let us now perform a community-based average (equation 2.12) of the governing equation 2.7 to find

$$\dot{\boldsymbol{\xi}}_k = \frac{\sum_{i \in C_k} \kappa_i \boldsymbol{f}(\boldsymbol{x}_i)}{\sum_{i \in C_k} \kappa_i} + \sum_{j=1}^{n} \frac{\sum_{i \in C_k} \kappa_i A_{ij} \boldsymbol{g}(\boldsymbol{x}_i, \boldsymbol{x}_j)}{\sum_{i \in C_k} \kappa_i} \tag{2.14}$$

for $k = 1, \ldots, m$. It is further desirable to have the right hand side of the above equation be dependent on $\boldsymbol{\xi}$ instead of $\boldsymbol{x}$. The reduction can further be simplified if $\boldsymbol{f}$ is a linear

function, in which case, we have

$$\begin{aligned}\dot{\boldsymbol{\xi}}_k &= \boldsymbol{f}(\boldsymbol{\xi}_k) + \sum_{j=1}^{n} \frac{\sum_{i\in C_k} \kappa_i A_{ij} \boldsymbol{g}(\boldsymbol{x}_i, \boldsymbol{x}_j)}{\sum_{i\in C_k} \kappa_i} \\ &= \boldsymbol{f}(\boldsymbol{\xi}_k) + \sum_{p=1}^{m} \frac{\sum_{j\in C_p}\sum_{i\in C_k} \kappa_i A_{ij} \boldsymbol{g}(\boldsymbol{x}_i, \boldsymbol{x}_j)}{\sum_{i\in C_k} \kappa_i}.\end{aligned} \tag{2.15}$$

We note that the averaging of the nonlinear term $\boldsymbol{g}$ in general cannot be further simplified. However, we can approximate this nonlinear term as a function of $\boldsymbol{\xi}$. That is, we can reduce the governing equation to the form of

$$\dot{\boldsymbol{\xi}}_k = \boldsymbol{f}(\boldsymbol{\xi}_k) + \sum_{p=1}^{m} \tilde{A}_{kp} \tilde{\boldsymbol{g}}(\boldsymbol{\xi}_k, \boldsymbol{\xi}_p) \tag{2.16}$$

based on the centroid-based state variable $\boldsymbol{\xi}$.

The governing equation of the above form can be derived using two approaches. If the networked dynamics is well known from theory, we can use the same interaction function $\boldsymbol{g}$ for $\tilde{\boldsymbol{g}}$ and the same form of the network edge weights. This implicitly assumes that the edge weight can be quantified in the same manner. It should be noted that reduced adjacency matrix $\tilde{A} \in \mathbb{R}^{m\times m}$ is much smaller in size compared to the original matrix $A \in \mathbb{R}^{n\times n}$. While this approach appears simple, the use of the original forms for $\tilde{\boldsymbol{g}}$ and $\tilde{A}$ generally leads to an approximate model.

An alternative approach is to determine $\tilde{A}$ and $\tilde{\boldsymbol{g}}$ numerically through system identification [96]. For systems with no a priori knowledge of the network structure, one can find the adjacency matrix A based on system identification or network inference [75, 55, 28, 96]. Data-based techniques can be used to find the reduced adjacency matrix and the interaction function if time-series data of the dynamical systems are available for $\boldsymbol{\xi}(t)$. One can pursue algorithms that minimizes the L_2 measure or the L_1 norm to promote sparsity within the derived model. Nonlinear system identification method, such as SINDy (sparse identification of nonlinear dynamics), has enabled the sparse identification of governing equations [21]. In the examples we consider later, we use both of the aforementioned approaches.

By establishing the community-based model of the networked dynamics, we can extend the present approach to model an observable or auxiliary variable $\boldsymbol{y} \in \mathbb{R}^q$ that is dependent on the state dynamics. That is, for such variables that satisfies

$$\boldsymbol{y} = \boldsymbol{h}(\boldsymbol{x}) \quad \text{or} \quad \dot{\boldsymbol{y}} = \boldsymbol{h}(\boldsymbol{x}, \boldsymbol{y}), \tag{2.17}$$

we seek a reduced-order model

$$\boldsymbol{y} = \tilde{\boldsymbol{h}}(\boldsymbol{\xi}), \quad \text{or} \quad \dot{\boldsymbol{y}} = \tilde{\boldsymbol{h}}(\boldsymbol{\xi}, \boldsymbol{y}) \tag{2.18}$$

based on the centroid variable $\boldsymbol{\xi}$. The function $\tilde{\boldsymbol{h}}$ can be modeled through nonlinear regression analysis [11]. Again, it is possible to develop a model based on the use of different norms as mentioned above. To fit an appropriate model, a library of the possible nonlinear basis functions $\boldsymbol{\Theta}(\boldsymbol{\xi}, \boldsymbol{y})$ can be constructed so that

$$\dot{\boldsymbol{y}} = \boldsymbol{\Theta}(\boldsymbol{\xi}, \boldsymbol{y})\boldsymbol{B}. \tag{2.19}$$

For example, $\boldsymbol{\Theta}$ can consist of a library of polynomials and trigonometric terms of $\boldsymbol{\xi}$ and $\boldsymbol{y}$ [96, 21]. These terms, along with $\dot{\boldsymbol{y}}$, are compiled from a time series of data for a training period of $-T \leq t \leq 0$. From such a library, the regression coefficients $\boldsymbol{B}$ can be determined by a matrix solver. Moreover, it is possible to consider sparse regression for solving $\boldsymbol{B}$ following the sequential thresholding least-squares algorithm implemented in SINDy [21], further simplifying the governing equation in the case of $\dot{\boldsymbol{y}} = \tilde{\boldsymbol{h}}(\boldsymbol{\xi}, \boldsymbol{y})$. Once these models are developed, they can be used to estimate the output variable $\boldsymbol{y}$ or predict it based on training data and a given initial condition.

The implications of the formulations discussed above pertains towards analyzing the overall dynamics of high-dimensional systems with an intrinsic community structure. Also, this is achieved solely through utilizing data inspired network-based techniques taking advantage of the interaction-based physics. With such techniques, one need not track all elements involved in the system, whereas just capture the community centroids in the system to uncover

the overall networked dynamics and other auxiliary variables of the system.

2.3.1.1 Community-based reduction of vortical flows

To reduce the dimension of the fluid flow system, we distill the vortical communities (coherent network structures) to their controids. We use the community detection methodology described in section 2.3 to identify these coherent structures or vortical communities from the given data. The procedure for identifying communities in the vortical network of a collection of discrete point vortices is portrayed in figure 2.4. Once the communities are detected from the flow field, the centroid of each identified community is calculated by

$$\boldsymbol{\xi}_k \equiv \frac{\sum_{i \in C_k} \Gamma_i \boldsymbol{r}_i}{\sum_{i \in C_k} \Gamma_i}, \quad k = 1, 2, \ldots, m \tag{2.20}$$

and the total circulation of each community, $\sum_{i \in C_k} \Gamma_i$, is concentrated to the community centroid, distilling the vortical community into a point vortex at the community centroid. The vortical network is redefined using the circulation and position vector of each community centroid, thus reducing the dimension of the system significantly. Although it is not performed here, it is possible to consider a bipartite graph to relate the reduced centroid-based network to the original dense vortical network using an incidence matrix [104].

With the formulation established for vortical flows, we can model the overall dynamics of the original high-dimensional networked fluid flow system using the present community-based approach. In section 3.1.1, we demonstrate the effectiveness of the present formulation to capture the macroscopic motion of vortices in nonlinear flows. Furthermore, we can formulate other auxiliary variables in fluid flow problems, like unsteady lift and drag forces on bodies, solely using the properties of the community centroid variable $\boldsymbol{\xi}$. Two examples are considered to highlight the ability to develop models that can capture aerodynamic forces on bodies imposed by the unsteady wake flows based on extracted vortical communities. These applications are presented in section 3.1.2.

2.3.2 Community-based extraction of influential structures

The identification of vortical communities allows us to use various community-based measures to analyze the connectivity within and amongst the communities. The community information can then be used to decompose the term with the adjacency matrix in equation 2.7 as

$$\dot{\boldsymbol{x}}_i = \boldsymbol{f}(\boldsymbol{x}_i) + \sum_{j,c_j=c_i} A_{ij}\boldsymbol{g}(\boldsymbol{x}_i, \boldsymbol{x}_j) + \sum_{j,c_j\neq c_i} A_{ij}\boldsymbol{g}(\boldsymbol{x}_i, \boldsymbol{x}_j). \tag{2.21}$$

The second term on the right-hand side represents the interaction of node i with the nodes in its own community and the third term denotes the interaction of node i with the nodes in the other communities. The former represents the intra-community interactions and the latter term captures the inter-community interactions of node i. This gives a community-based dynamical systems equation for the elements of a network, emphasizing local influences of the communities. An illustration of the above procedure applied to the system of point vortices is shown in figure 2.5. The network with no distinction of the weighted edges is shown in figure 2.5 (left). The community detection algorithm classifies the nodes into several communities, highlighted by the coloured circles in figure 2.5 (right). The intra- and inter-community edges are shown in red and blue, respectively.

Let us quantify the local influence of a node using the above formulation. Similar to how the node strength is defined in equation 2.8, the strength of node i to influence all nodes in community k can be defined as

$$s_{i,k} = \sum_{j,c_j\in\hat{C}_k} A_{ji}. \tag{2.22}$$

Moreover, the strength of a node on the network can be separated into intra- and inter-community strengths as

$$s_i^{\text{intra}} = \sum_{j,c_j=c_i} A_{ji} = s_{i,c_i} \quad \text{and} \quad s_i^{\text{inter}} = \sum_{j,c_j\neq c_i} A_{ji} = \sum_{k,k\neq c_i} s_{i,k}, \tag{2.23}$$

respectively. These community-based strengths can be used to quantify the interactions with respect to communities.

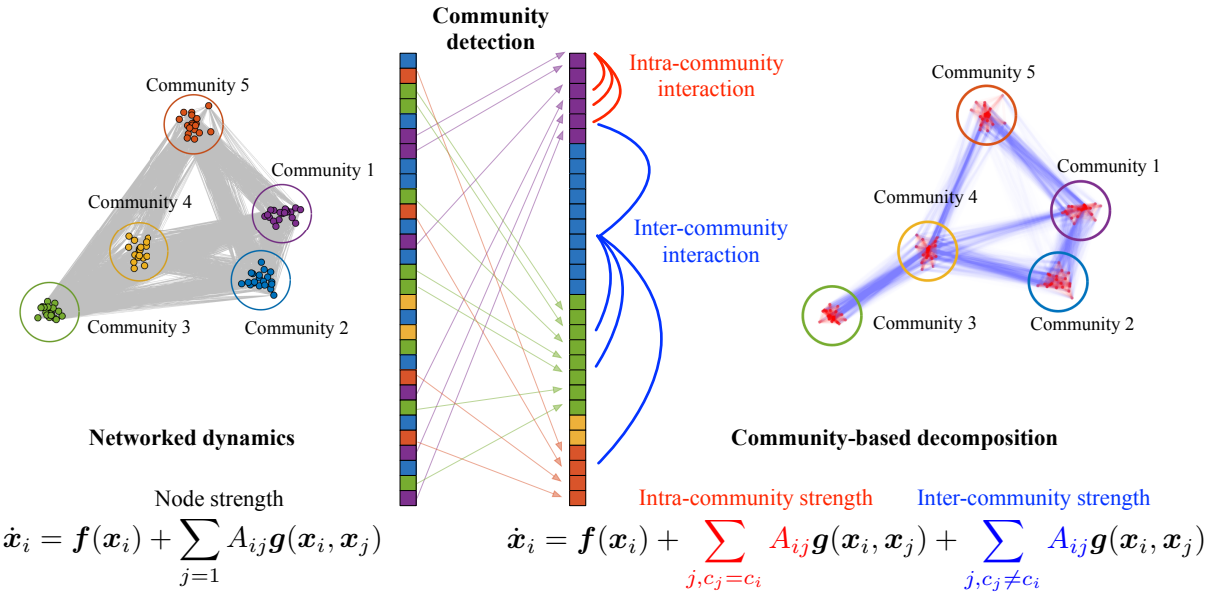

Figure 2.5: Overview of the community-based decomposition of networked dynamics using intra- and inter-community interactions.

The intra-community strength can be normalized as the within-module z-score [44] given by

$$Z_i = \frac{s_i^{\text{intra}} - \overline{s_i^{\text{intra}}}}{\sigma_{s_i^{\text{intra}}}}, \tag{2.24}$$

where $\overline{s_i^{\text{intra}}}$ and $\sigma_{s_i^{\text{intra}}}$ are the mean and standard deviation of s_i^{intra} over all nodes in the community of i. The within-module z-score identifies the most well-connected node inside a community or the hub node of a community. Note that the hub node of a community need not be well-connected with the other communities in the network.

A relative measure of inter-community strength of a node, quantified by how well-distributed its edges are amongst communities, can be given by the participation coefficient [44]

$$P_i = 1 - \left[\left(\frac{s_i^{\text{inter}}}{s_i} \right)^2 + \left(\frac{s_i^{\text{intra}}}{s_i} \right)^2 \right]. \tag{2.25}$$

When $P_i \approx 1$, edge weights of node i are equally connected among all communities and $P_i = 0$ when the node is only connected to its own community. Note that $s_{i,k}$, Z_i, and P_i can be evaluated for both in- and out-edges. In the present study, we evaluate the out-edge based measures following the definition of edge weight from equation 2.6.

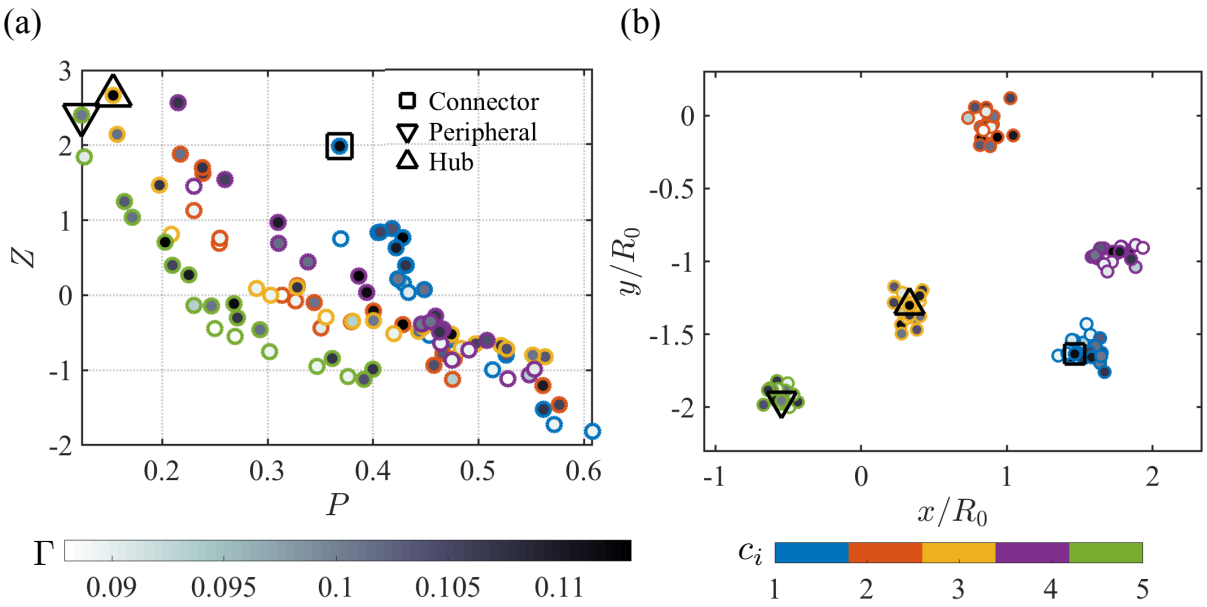

Figure 2.6: (a) Distribution of the discrete point vortices in the $P - Z$ map. (b) Position of the important nodes in physical space.

The $P - Z$ map of the nodes is an important feature space for revealing key elements within and amongst the communities [45, 117, 34]. The $P - Z$ map for the system of point vortices is shown in figure 2.6 (a). The nodes on the left side of the $P - Z$ map have very low inter-community interactions and are isolated groups, called *peripherals*. On the other hand, the nodes on the right side have high inter-community interactions making them well-connected to most communities and are called *connectors*. The nodes on the top region with high Z value have the strongest interactions within the respective communities. Note that the name peripheral need not refer to nodes at the physical perimeter of the domain. The strongest peripheral nodes will have high influence within their communities but the least influence on other communities. In contrast, the strongest connector nodes will have the highest influence amongst communities, particularly on the neighbouring communities, and high influence within their own community.

We use the $P - Z$ feature space to search for the strongest peripheral and connector nodes in a network, herein referred to as simply peripheral and connector nodes. We find the average P_i of each community k, denoted as $\overline{P_k}$. The peripheral node of a network is the node i given by $\max_{i,c_i=k} Z_i$, belonging to the community k with $\min_k \overline{P_k}$. The connector

node i is given by $\max_{i,c_i=k} Z_i$, belonging to community k with $\max_k \overline{P_k}$. The connector, peripheral, and hub nodes of the discrete point vortex system are indicated in figure 2.6 (a). The $P - Z$ values for the nodes suggest that the hub node would have similar characteristics as the peripheral node. The three important nodes are also highlighted in the physical space as shown in figure 2.6 (b). The positions of the peripheral and connector nodes suggest that an influential node need not be located at the geometric center of the community. The observations signify the need to consider inter- and intra-community interactions for identifying important nodes. Let us now demonstrate how the behavior of the networked system can be modified using these measures.

CHAPTER 3

Applications

3.1 Community-based reduced-order modelling

In this section, we take the network community-based reduced-order modeling technique described in section 2.3.1 to study two types of vortical flows. First, we consider a group of discrete point vortices and model their collective motion based on the community centroids. Second, we consider unsteady wake flows behind a circular cylinder and an airfoil with a flap, whose wakes are described by the motion of vortical communities. The properties of these communities are then used to derive reduced-order models to predict the forces imposed on the bodies. These flows, familiar in the field of fluid dynamics, are chosen to validate the present approach. These model problems highlight the capabilities of the network community-based modeling technique to significantly reduce the dimensions of the complex nonlinear flow physics, while retaining the important interactions present in the flows.

3.1.1 Reduced-order point-vortex dynamics

We first study the unsteady dynamics of a collection of discrete point vortices as shown in figure 3.1 (also in figure 2.4). As we aim to capture the time-varying behavior of a collection of vortices, the Lagrangian description is apt to construct the community-based reduced order model. We consider the same model problem setup with $n = 100$ discrete point vortices used in section 2.1. This forms a complete graph (dense network) of vortical interactions as shown in figure 3.1 (top left) resulting from velocity induced by the vortices on each other. The vortical network does not contain any self-loops as a vortex does not induce velocity upon

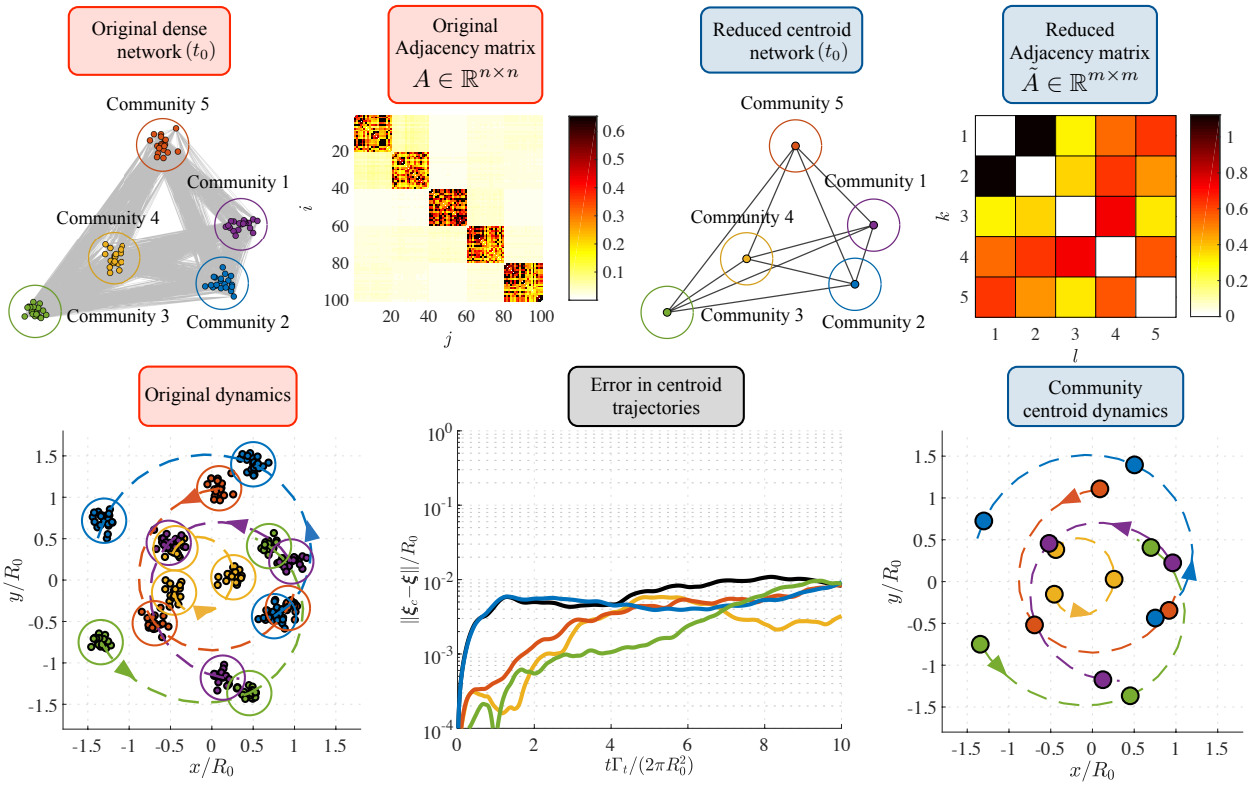

Figure 3.1: Community-based networked dynamics of point vortices. The network structure and adjacency matrix at initial time (t_0), overall dynamics, and error between the community centroid dynamics for both the original dense $(n = 100)$ and the community-based reduced $(m = 5)$ point vortex systems are shown.

itself. Thus, the total number of interactions in the original vortical network is $n(n-1)$. The adjacency matrix corresponding to the vortical interactions is shown adjacent to the dense network in figure 3.1. The colors in the adjacency matrix denote the edge weights.

Using modularity maximization algorithm described in section 2.3, the set of point vortices are separated into $m = 5$ communities. In this problem, there are strong intra-community ties in the original adjacency matrix, which enables a clear decomposition of the group of vortices into communities. For each community, we can determine the vortical community centroid using equation (2.20). The resulting reduced network of these community centroids is shown in figure 3.1 (top right). The number of interactions have been reduced to $m(m-1)$.

The adjacency matrix for the reduced community network is given by

$$\tilde{A}_{kp} = \frac{\sum_{j \in C_p} \Gamma_j}{2\pi \left\| \boldsymbol{\xi}_k - \boldsymbol{\xi}_p \right\|_2}, \tag{3.1}$$

where the state vector $\boldsymbol{\xi}$ contains only the position information of the community centroids. The circulation Γ of the vortices do not change in time as the flow is inviscid. Here, the edge weights for the reduced graph are quantified in the same manner as in the original network, but now for the community centroids. Note that the reduced network weights conserve the total circulation of the system, as all circulations within the community are summed. The reduced adjacency matrix is shown in figure 3.1 next to the reduced centroid network. As the communities with strong intra-community ties are reduced to their representative centroids, the reduced adjacency matrix highlights the interactions between communities. We see a strong interaction between communities 1 and 2. Community 3 experiences weak influence from all other communities, except from community 4, due to community 3 being placed far from the rest of the communities.

The interaction-based dynamics of the discrete point vortex system is governed by the Biot-Savart law given by equation 2.4. This can be treated as a networked dynamical system given by equation 2.7 with a time-varying network, as previously mentioned in section 2.1. As the position of the point vortices changes over time, the adjacency matrix can be updated accordingly. Trajectories based on the full nonlinear dynamics of the full system with $n = 100$ vortices are shown in figure 3.1 (bottom left). Shown in figure 3.1 (bottom left) are the vortical positions for the communities at representative times. Also superposed in dashed lines are the trajectories of the community centroids ($\boldsymbol{\xi}_c$) to track their bulk motion. Although, these centroids are defined according to equation 2.20, these are computed *a posteriori* considering updated positions of all the vortices within the communities.

Reducing the system to the community centroid-based representation, we can solve for the dynamics of the community centroids using equation 2.16. For the community centroid

dynamics of vortical flows, $\boldsymbol{f}(\boldsymbol{\xi}_k) = 0$ and the interaction function $\tilde{\boldsymbol{g}}$ takes the form of

$$\tilde{\boldsymbol{g}}(\boldsymbol{\xi}_k, \boldsymbol{\xi}_p) = \frac{\hat{\boldsymbol{k}} \times (\boldsymbol{\xi}_k - \boldsymbol{\xi}_p)}{\|\boldsymbol{\xi}_k - \boldsymbol{\xi}_p\|_2}. \tag{3.2}$$

Note that $\boldsymbol{g}$ and $\tilde{\boldsymbol{g}}$ are of the same form. Using equations 3.1 and 3.2 in equation 2.16, we can solve for the dynamics of the community centroids as shown in figure 3.1 (bottom right). Here again, time-varying reduced adjacency matrices are computed for the dynamics of the centroids. Upon comparing the dynamics of the original system and the community-based reduced-order model, it can be seen that the community-based model accurately tracks the bulk motion of the communities. The errors in the centroid trajectories ($\|\boldsymbol{\xi}_c - \boldsymbol{\xi}\|_2/R_0$) determined by the community-based reduced-order model are shown in figure 3.1 (bottom center). The error level is limited to $\mathscr{O}(10^{-2})$ for all communities over the course of the rotational motion. The community-based model tracks the unsteady dynamics of all discrete vortex communities in an accurate manner.

The application of the network community-based reduced-order model to the analysis of point vortex dynamics has shown its effectiveness to accurately capture the inter-community interactions and the macroscopic dynamics of the overall system. The fact that the present model can handle the nonlinear flow dynamics its shows potential to capture the essential physics for a variety of vortex dominated flows in a computationally tractable manner. In the next example, we demonstrate that the present formulation can be used for unsteady wake flows that have a continuous flow field representation over the spatial domain. Even with the added complexity, we show that this network-based model can serve as a basis to develop a nonlinear model to predict unsteady forces on the body.

3.1.2 Reduced-order wake force modeling

Fluid flow past solid bodies leads to the formation of complex, unsteady, nonlinear flow modifications in the wake. The laminar or turbulent wake gives rise to the formation and interaction of vortical structures, causing unsteady aerodynamic forces on the body. Here, the objective is to understand the dynamics of these flows based on network-theoretic ap-

proaches to model and predict the forces on the body. Thus, we formulate reduced-order models for these observable (auxiliary) variables of the flow. In particular, we consider the modeling of aerodynamic lift and drag forces (C_L and C_D, respectively), using the properties of the community-based centroids, as outlined in section 2.3.1.

As an example, we choose to model as $\boldsymbol{y}$ in equation (2.18) the lift and drag coefficients ($C_L,\ C_D$), defined as

$$C_L \equiv \frac{F_y}{\frac{1}{2}\rho u_\infty^2 S} \quad \text{and} \quad C_D \equiv \frac{F_x}{\frac{1}{2}\rho u_\infty^2 S}, \tag{3.3}$$

respectively. In the above non-dimensionalization, F_y and F_x are the lift and drag forces on the body, ρ is the fluid density, u_∞ is the freestream velocity, and S is the characteristic body surface area. The formation and interaction of the vortical structures lead to action of impulsive forces on the body [118, 108]. Thus, following the definition of induced velocity in equation 2.5, it is sensible to select the circulation Γ and inverse of the position $1/\|\boldsymbol{\xi}\|_2$ of the vortex community centroids, as the basis functions in equation 2.19 to model $\dot{\boldsymbol{y}}$. Note that the state vector $\boldsymbol{\xi}$ contains only the position vector of the community centroids. The circulation of each community is measured over time and varies in time due to the vorticity profile diffusing across the community boundary. We also consider the equivalent circulation on the body (Γ_0) to be a basis function, which is related to the unsteady lift force through the Kutta–Joukowski theorem [10, 3].

A polynomial combination of the aforementioned basis functions, summed over the m centroids, forms a library $\boldsymbol{\Theta}$ to solve for $\boldsymbol{B}$ in equation 2.19. The order of polynomial library depends on the complexity of the vortical community dynamics of the wake. Stronger the nonlinearity in the wake caused by vortical communities, more complex the unsteady force on the body, and thus higher order combination of the basis functions is required to construct the reduced-order model. For all problems discussed in the current study, the third-order polynomial library is found sufficient to capture both the vortical interactions as well as the multiple frequencies appearing in the forces. As such, we arrive at the reduced-order model

for $\boldsymbol{y}$ as,

$$\dot{\boldsymbol{Y}} = \boldsymbol{\Theta}\boldsymbol{B} = \begin{bmatrix} \boldsymbol{\Theta}_1 & \boldsymbol{\Theta}_2 & \boldsymbol{\Theta}_3 \end{bmatrix} \begin{bmatrix} \boldsymbol{B}_1 \\ \boldsymbol{B}_2 \\ \boldsymbol{B}_3 \end{bmatrix} \tag{3.4}$$

where

$$\dot{\boldsymbol{Y}}^T = \left[\dot{\boldsymbol{y}}^T(t_1),\ \dot{\boldsymbol{y}}^T(t_2) \dots \dot{\boldsymbol{y}}^T(t_q)\right] \tag{3.5}$$

and

$$\boldsymbol{\Theta}_1 = \sum_{i=0}^{m} \begin{bmatrix} f_i^1,\ f_i^2 \end{bmatrix} \tag{3.6}$$

$$\boldsymbol{\Theta}_2 = \sum_{i,j=0}^{m} \begin{bmatrix} f_i^1 f_j^1,\ f_i^1 f_j^2,\ f_i^2 f_j^2 \end{bmatrix} \tag{3.7}$$

$$\boldsymbol{\Theta}_3 = \sum_{i,j,k=0}^{m} \begin{bmatrix} f_i^1 f_j^1 f_k^1,\ f_i^1 f_j^1 f_k^2,\ f_i^1 f_j^2 f_k^2,\ f_i^2 f_j^2 f_k^2 \end{bmatrix} \tag{3.8}$$

given

$$f_i^1 = \frac{1}{\|\boldsymbol{\xi}_i(t)\|_2}, \quad f_i^2 = \Gamma_i(t), \quad \Gamma_0 = -\frac{C_L(t)}{\rho u_\infty}. \tag{3.9}$$

where Γ_0 is the equivalent circulation on the body due to lift force and $\boldsymbol{\xi}_0$ is the position of the body. In the current work, we set $\boldsymbol{\xi}_0 = 0$ and exclude terms that contain $1/\|\boldsymbol{\xi}_0\|_2$.

We construct matrices $\dot{\boldsymbol{Y}} \in \mathbb{R}^{q\times 2}$ and $\boldsymbol{\Theta} \in \mathbb{R}^{q\times 9}$ using q discrete time-series data over a training period. The coefficient matrix $\boldsymbol{B} \in \mathbb{R}^{9\times 2}$ is determined in this study using the Moore–Penrose inverse. One can alternatively use a sparse matrix solver such as LASSO [134, 54]. For the problems we consider below, the flow fields are reduced to a small number of community centroids, and does not necessitate the use of sparse solvers. For the wake flow problems analyzed in the current work, a training period of three cycles is found to result in convergence of the coefficients. To predict the forces, equation 3.4 can then be time integrated with Γ and $1/\|\boldsymbol{\xi}\|_2$ of the vortex community centroids provided from corresponding time-series snapshots. Below, we apply these reduced-order formulations to predict lift and drag forces due to fluid flow over a two-dimensional circular cylinder and an airfoil with a flap.

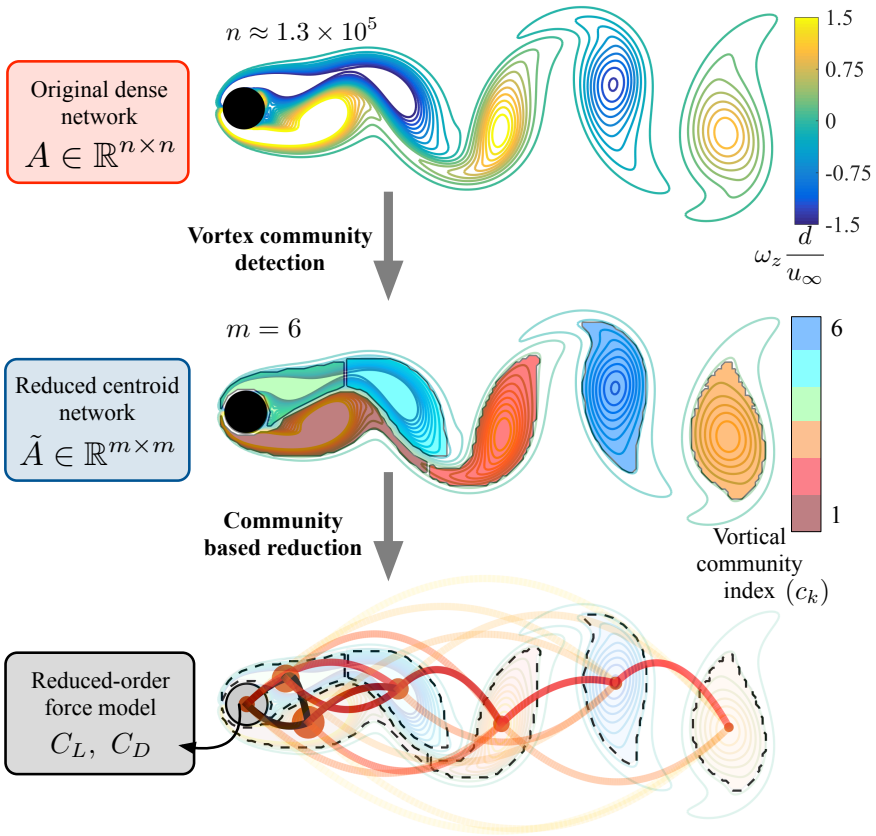

Figure 3.2: Network community-based reduction of the vortices in the von Kármán vortex street and force modeling.

3.1.2.1 Unsteady force generated by wake of a circular cylinder

One of the fundamental phenomena in fluid dynamics is the formation of the von Kármán vortex street in bluff body wakes. In particular, the wake of a circular cylinder, as depicted in figure 3.2, serves as a canonical nonlinear problem in unsteady fluid dynamics. Even for a laminar regime, the shedding of the wake vortices leads to generation of large amplitude unsteady forces on the cylinder. Although there have been extensive discussions on the mechanism of vortex shedding and its implication on unsteady forces [116], we focus here on simply feeding the flow field data to extract the vortical communities and use the centroid vector to develop a network-based force model. That is, we rely on the network-based framework to decipher important vortical interactions and centroid quantities without depending on the full Navier–Stokes equations, as depicted in figure 3.2.

The unsteady vortical flow field data to be used in this analysis is derived from two-dimensional direct numerical simulations (DNS), using the immersed boundary projection method [130, 25, 71]. We consider incompressible flow over a circular cylinder at a diameter-based Reynolds number of $Re = 100$. Extensive validation of this code and cylinder flow simulations have been performed and are reported in [91]. Time resolved vorticity field snapshots are captured, and following the formulations in section 2.1, the network of interactions among the vortical elements are defined for each snapshot using equation 2.6. Here, the edge weights are non-dimensionalized by the freestream velocity, $u^* = u_\infty$. In this example, following the Eulerian description discussed in figure 2.2 to represent the continuous flow field, we take each and every Cartesian grid cell of size $\Delta x \times \Delta y$ to represent a network node with a circulation over the cell being denoted by Γ. For the grid resolution chosen in the current study, the number of nodes and edges in the network scales to $\mathscr{O}(10^5)$ and $\mathscr{O}(10^{10})$ (following a vorticity threshold of 95% of the maximum vorticity of original data, the number of nodes reduces to ≈ 4000) respectively, as mentioned in figure 3.2. The strength distribution of the cylinder wake network, and other laminar wakes, follow a power-law distribution, as shown in figure A.1 in Appendix A. We concentrate on using the community-based formulations to for reduced-order models for lift and drag.

Following the community detection procedure discussed in section 2.3, we identify different vortical communities in the wake as illustrated in figure 3.2 (middle). For a given snapshot of the two-dimensional flow field, we decompose the flow field into positive and negative vorticity fields. A directed version of the modularity maximization algorithm [100, 24, 79] is applied to the two data sets comprising of vortical elements with clockwise (negative) and counter-clockwise (positive) vorticity. Due to the unsigned edge weight, we need to separate the two data sets as the current community detection procedure is unable to distinguish spatially close vortical communities, usually the positive and negative vortical structures, especially for wake flows. The resolution effects in the modularity maximization algorithm [35, 114, 115] are also taken into consideration. We then create a community-based network using the community centroids as shown in figure 3.2 (bottom). This reduces the number of nodes and edges to 6 and 30 (no self-loops), respectively. We also consider the cylinder itself

as a node since the Kutta–Joukowski theorem relates lift to the circulation of the cylinder.

Different vortical communities are shown in figure 3.2 (bottom) along with the centroids. Here the nodes have varied sizes corresponding to their total network degree. The color and transparency of the lines connecting the nodes depict the strength of connection between them. The strong connection between adjacent communities in the wake is clearly depicted through this reduced dimensional network. Also, the high influence of the near-field vortical communities on the cylinder is evident.

To predict lift and drag on the cylinder, instantaneous training data of $\dot{\boldsymbol{y}}$ and the community-based vortical centroids from the flow fields are used to determine the nine coefficients in $\boldsymbol{B}$ in equation 3.4. Due to the high influence of the near-field vortical communities and the time-periodic shedding of a positive vortex and a negative vortex, we only use the information of the first two community centroids ($m = 2$) to model the forces even though we show six vortical communities in the cylinder wake for visual clarity (figure 3.3 top). With coefficients $\boldsymbol{B}$ determined, equation 3.4 is time integrated by providing time series of input data ($\boldsymbol{\xi}$ and Γ) to predict C_L and C_D on the cylinder. The predicted forces from this model are compared to the forces obtained from DNS in figure 3.3 (bottom), exhibiting agreement where predictions are on top of the reference forces.

The reduced-order force model, relying solely on the information of the community-based reduced vortical centroids, is able to accurately capture the effect of the vortex shedding phenomena on the forces. The results from figure 3.3 (bottom) show that the reduced-order force model accurately predicts the lift force with an error of 5.6% for L_2 in time. The lift force is predicted over more than twice the training period while maintaining this accuracy, without any divergence later in time. The drag force, even with smaller level of fluctuations, is also accurately predicted over a considerable period of time with an error of 0.2%. Although the basis functions used depends on the vortical community formation (shedding) frequency, the nonlinear combinations of the basis functions chosen to arrive at equation 3.4 is able to model the fluctuations in the drag force, which are twice the vortex shedding frequency for flow over a circular cylinder.

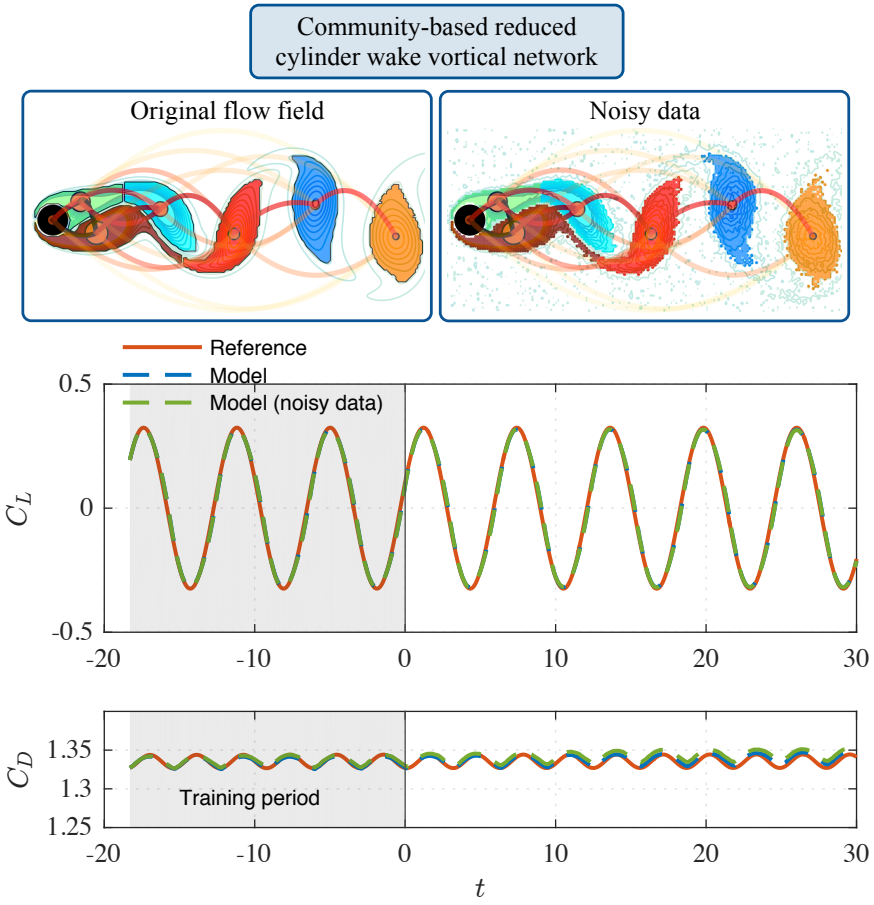

Figure 3.3: Community-based reduced representation of a cylinder wake, and lift (C_L) and drag (C_D) forces on the cylinder predicted using the centroid-based reduced-order model. Resilience of the methodologies are tested using noisy flow field data.

The resilience of the present model to perturbations or noise in the flow field (input data) is also examined. Artificial noise with a signal-to-noise ratio of $SNR = 0.1$ is added to the original vorticity field data to simulate noise in experiments or turbulence in the flow. The community detection algorithm identifies the vortical communities from the noisy data as shown in figure 3.3 (top right). The network structures of the communities in the wake are still identified robustly even with the presence of noise. The forces are predicted using this noisy data as shown in figure 3.3 (bottom). The shown results also exhibit the resilience of the force-model towards noisy input data. The lift force prediction with the noisy input hardly deviates form that obtained using the original clean data with an error of 6.1%. The drag force is also predicted accurately with an error of 0.4%. The resilience of the model attributes to effects of both the vortical community detection and computation of the centroid-based properties acting as an integration filter, effectively removing the influence of external noise on the vorticity field. As demonstrated above, the use of the reduced-order model allows for the unsteady vortical flow over a circular cylinder to be represented simply through the information distilled to the vortical centroids.

3.1.2.2 Unsteady force on an airfoil with a Gurney flap

Next, we extend the application of the present community-based formulation to a more complex flow. The intricate flow phenomena produced by the flow over an airfoil with a flow modification device, Gurney flap [81], attached to the trailing edge is explored [41]. Flow modification and control of airfoil wakes have been studied extensively for lift enhancement and drag reduction [69]. Low-Reynolds number flows over airfoils with Gurney flaps at high angles of attack generate a variety of strongly nonlinear, unsteady vortical flows posing complex effects on lift and drag forces in both two- and three-dimensional settings [41]. Such two-dimensional incompressible flows over NACA 0012 airfoils can produce a wake classified under the 2P regime [136, 42, 41], with periodic shedding of two pairs of positive and negative vortices as depicted in figure 3.4 (top left). The vortex shedding attributes to a nonlinear aerodynamic force characteristics on the airfoil. Detailed analysis of the various wake regimes and associated aerodynamic forces generated by two- and three-dimensional

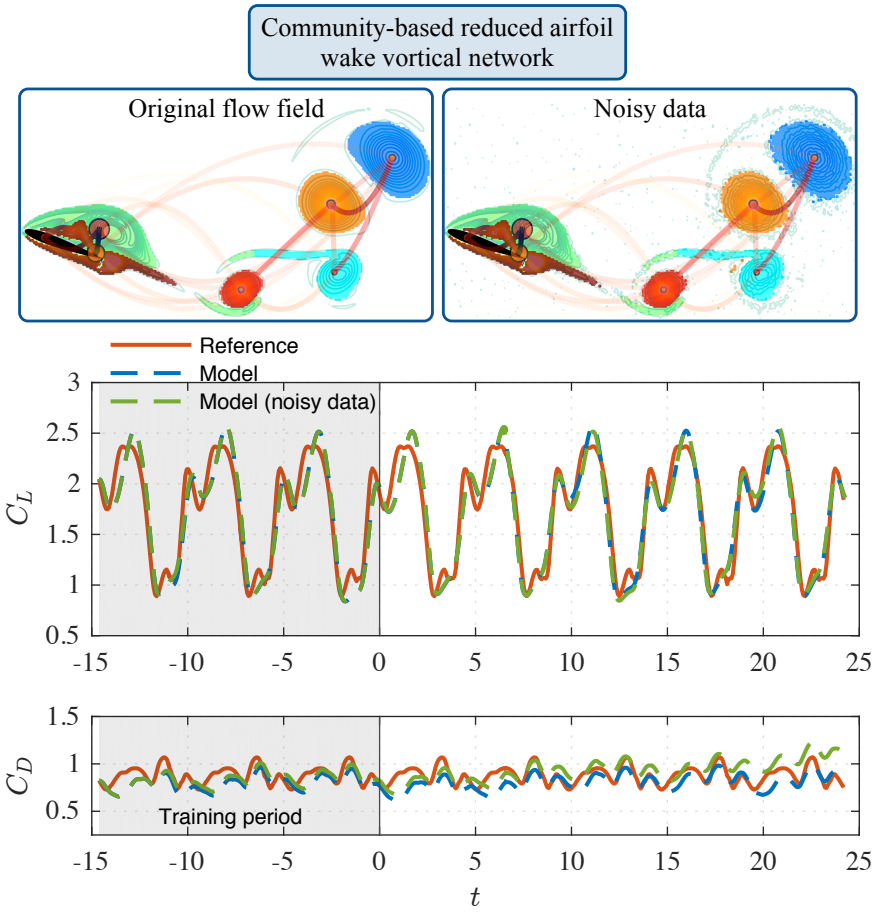

Figure 3.4: Community-based reduced representation of a NACA 0012 airfoil wake classified under the 2P regime, and lift (C_L) and drag (C_D) forces on the airfoil predicted using the centroid-based reduced-order model. Resilience of the methodologies are tested using noisy flow field data.

flows over the airfoil is provided in Appendix B.

We perform two-dimensional DNS of the flow over a NACA 0012 airfoil at an angle of attack of 20° and flap height of $0.1c$ (c: chord length) with a chord-based Reynolds number of $Re = 1,000$ [41] using the immersed boundary projection method mentioned in section 3.1.2.1. Details of the computational setup are provided in Appendix B. Following the procedure used to analyze the cylinder wake, we capture time-resolved vorticity field snapshots of the flow, and form the full dense vortical network for the 2P wake flow. Through the community-based formulation, vortical communities are extracted from the full network and vortical centroids are defined as shown in figure 3.4 (top). Along with the considerable reduction in dimension attained, the complex nonlinear 2P wake with the two main and two

secondary vortical structures are effectively captured by the network-theoretic techniques. The high influence of the two near-field vortical communities being formed on the airfoil is clearly depicted through the reduced network. The strong influence among the vortical communities in the far-field is also revealed through the community-based network.

The effect of this vortical flow on lift and drag forces are modeled following the procedure discussed for the cylinder problem. We use the position vector and circulation of the time periodically shedding four vortical centroids ($m = 4$) to model the forces using equation 3.4. We present the results of the lift and drag prediction compared to that from the DNS in figure 3.4 (bottom). The complex 2P wake imposes highly fluctuating forces on the airfoil with multiple peaks. The reduced-order model predicts this highly nonlinear time-periodic lift curve accurately with an error of 8.8% for L_2 in time. The multiple peaks with varying amplitudes imposed by the shedding of the primary and secondary vortical communities are effectively captured by the current community-based model. The drag force, with comparatively less magnitude and small-scale fluctuations, is also captured with an error of 12.7%. These results highlight the importance of effectively identifying the vortical communities in the flow field.

To test the resilience of the force model to noise, we follow the same procedure as in the cylinder problem by adding artificial noise to the flow field. Again, the voritcal communities are effectively captured by the community detection procedure as shown in figure 3.4 (top right), preserving the network structure observed for the original noiseless flow field. A time series of this data is used to predict the forces and the results are depicted in figure 3.4 (bottom). The lift force prediction based on the noisy flow field data remains accurate without noticeable difference from the prediction based on clean data with an error of 8.8%. The drag is also predicted well. The predicted drag curve deviates at later time, but the amplitude of deviation is small compared to the mean of the C_D curve, and the error is 13.2%. The integrating effect of the community detection technique and the centroid-based calculations is further exemplified here. These results show the ability of the network community-based formulation to model forces on a body in a computationally reduced and robust manner.

3.2 Community-based flow modification

In this section, we use the community-based decomposition of the networked-dynamics using intra- and inter-community interaction described in section 2.3.2 to assess the influence of the community-based connector and peripheral structures to modify complex vortical flows. We first analyze the effects of the connector and peripheral communities on the dynamics of a collection of discrete point vortices. Second, we implement the community-based structure extraction procedure on two- and three-dimensional isotropic turbulence to identify connectors and peripherals in turbulent flows. Impulse perturbations are added to the extracted structures to assess their influence on turbulent flow modification. These results demonstrate the ability of the community-based formulation to extract flow modifying structures in a variety of complex vortical flows.

3.2.1 Modification of point-vortex dynamics

We analyze the influence of the connector, peripheral, and hub nodes identified using the network-based measures on the dynamics of a collection of discrete point vortices. We consider the same model problem setup with $n = 100$ discrete point vortices used in section 2.1. Velocity based impulse perturbations are added to the communities corresponding to the influential nodes. Based on the nodes, we refer to the perturbations as connector, peripheral, and hub-based perturbations. Positions of the perturbed communities at initial time are shown in figure 2.6 (b). We identify the influential nodes only at initial time as we are interested to explore the influence of the nodes on the system dynamics.

Impulse perturbations at discrete time $n_\mathrm{t}\Delta t$ are added to the velocity field with time step Δt and $n_\mathrm{t} = 0, 1, 2, \ldots$. The velocity of a perturbed node i at time t is given by $\boldsymbol{u}(\boldsymbol{r}_i, t) + \tilde{\boldsymbol{u}}(\boldsymbol{r}_i, t)$, where $\tilde{\boldsymbol{u}}(\boldsymbol{r}_i, t) = \alpha \hat{e}_{\boldsymbol{u}(\boldsymbol{r}_i,t)} \delta(t - n_\mathrm{t}\Delta t)$, α is the amplitude of perturbation, and $\hat{e}_{\boldsymbol{u}(\boldsymbol{r}_i,t)}$ is the unit vector in the direction of $\boldsymbol{u}(\boldsymbol{r}_i, t)$. Time is non-dimensionalized as

$t\Gamma_{\text{tot}}/(2\pi R_0^2)$. Amplitude of perturbation α is computed for a given energy ratio E of

$$E = \frac{\sum\limits_{i,c_i \in \hat{C}_p} \|\tilde{\boldsymbol{u}}(\boldsymbol{r}_i, t)\|_2^2}{\sum\limits_{i}^{n} \|\boldsymbol{u}(\boldsymbol{r}_i, t)\|_2^2}, \tag{3.10}$$

where $\hat{C}_p$ is the set of the perturbed community. We have analyzed the system dynamics with E varied between $0.01 - 0.1$ and have found qualitative similarity in the results. Here, we show the results of perturbations with $E = 0.1$ to portray significant changes in the vortex trajectories. The time step between each perturbation is $\Delta t\Gamma_{\text{tot}}/(2\pi R_0^2) = 0.024$.

The effect of the perturbations on system dynamics is assessed by observing the change in trajectories of the community centroids, as shown in figure 3.5. The centroid location $\boldsymbol{\xi}_k(t)$ of each community k is computed as

$$\boldsymbol{\xi}_k(t) = \frac{\sum_{i,c_i \in \hat{C}_k} \Gamma_i \boldsymbol{r}_i(t)}{\sum_{i,c_i \in \hat{C}_k} \Gamma_i}. \tag{3.11}$$

The connector-based perturbations achieve the largest deviations on the trajectories. The peripheral and hub-based perturbations have significant influence only on their neighbouring communities, communities 3 and 1, respectively. Regardless of the central location of the hub community at initial time, the system dynamics is not changed compared to the extent achieved by connector-based perturbations. This demonstration highlights the need to consider the strengths and relative positions in a systematic manner to identify the influential nodes.

Let us compare the community centroid trajectories in time, as shown in figure 3.6 (a). The trajectories of all other communities show the most deviation from baseline with connector-based perturbation, except for community 5. The trajectory of community 5, the peripheral community, is modified significantly when it is perturbed. We have evaluated the $P - Z$ map using the in-edges (not shown), which also gives community 5 to be the peripheral community. Thus, other communities have less influence on community 5. We concentrate on the results at early times to assess the characteristics of the connector to influence its

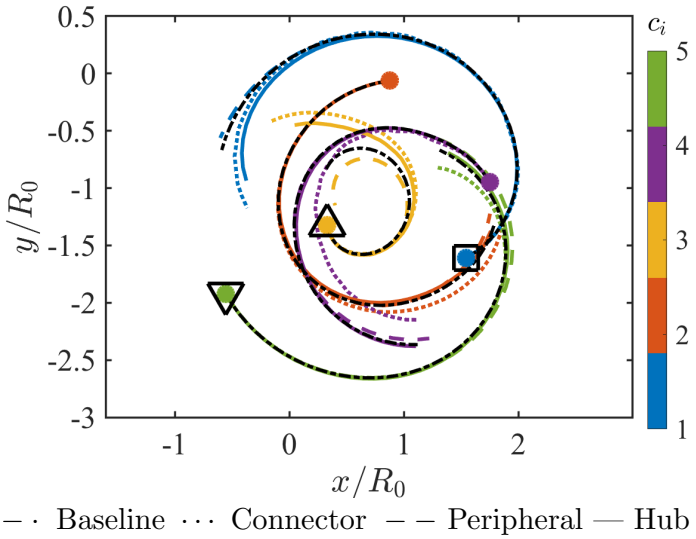

Figure 3.5: Trajectories of community centroids without and with connector (□), peripheral (▽), and hub-based (△) perturbations. Filled circles show initial position of the community centroids.

neighbour and connect with other communities. The trajectory of community 4 is changed significantly earlier in time with connector-based perturbations. This change in the trajectory of communities 4, the spatially closest community to the connector, at early times demonstrates the ability of a connector community to significantly influence its neighbour. Neither of the peripheral and hub-based perturbations influence other communities, particularly their respective neighbours, at early times. Later, the connector-based perturbations also significantly change the dynamics of community 3 by connecting through community 4, even though communities 1 and 3 are spatially far apart. The inter-community influence demonstrates the connecting characteristics of a connector community.

Deviation of the trajectories from baseline is quantified in figure 3.6 (b). The observations quantitatively show the larger deviations in trajectories resulting from connector-based perturbations. Considering the neighbours of the perturbed communities, a total change between $10-12\%$ of the baseline is achieved for communities 3 and 4 using connector-based perturbations. The corresponding changes using peripheral and hub-based perturbations are around 5% for communities 3 and 1, respectively. The largest effect of the hub community is on its own trajectory. These observations demonstrate the inference from the $P-Z$ map that the hub community can portray characteristics of a peripheral. The magnitude of change

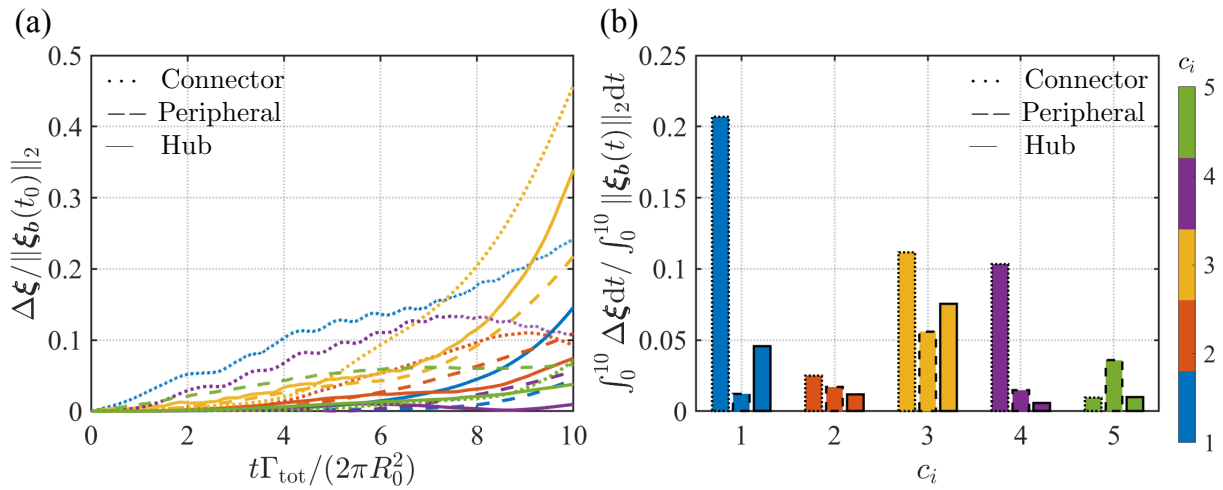

Figure 3.6: (a) Trajectories of community centroids subjected to perturbations compared with baseline, $\boldsymbol{\xi}_b$. Here, $\Delta\boldsymbol{\xi} = \|\boldsymbol{\xi}(t) - \boldsymbol{\xi}_b(t)\|_2$. (b) Total change in trajectory of community centroids with respect to the baseline.

achieved by the connector-based perturbation on its own trajectory is more than thrice that produced by peripheral and hub communities. Furthermore, the total change in trajectory of community 3 is the highest using connector-based perturbation. For this model problem, we have demonstrated that the connector node effectively modifies the global vortex dynamics. The present finding motivates the use of inter-community interactions to instigate changes in the global system dynamics, based on the community-based decomposition of system dynamics to identify key structures.

3.2.2 Flow modification of isotropic turbulence

Let us now consider the application of community-based flow modification to two- and three-dimensional decaying homogeneous isotropic turbulence. The highly complex and multi-scale properties of isotropic turbulence make it an apt choice to demonstrate the capability of the present community-based framework. Isotropic turbulence is a canonical model problem for a range of turbulent flows encountered in nature and engineering applications.

3.2.2.1 Numerical setup

For the two- and three-dimensional isotropic turbulent flows, we use the Fourier spectral and pseudo-spectral algorithms, respectively, to numerically solve the Navier-Stokes equations [133, 23]. Direct numerical simulations (DNS) of the flows are performed in bi-periodic and tri-periodic square and cubic domains of length L. For the simulations, the flow fields are resolved such that $k_{\max}\eta \geq 1$, where $k_{\max}$ is the maximum resolvable wavenumber of the grid and η is the Kolmogorov length scale. We non-dimensionalize the spatial variables by L, time by the large eddy turn-over time at initial time $\tau_e(t_0)$.

The two-dimensional turbulent flows with an initial Taylor microscale based Reynolds number of $Re_\lambda(t_0) \approx 4000$ are obtained from DNS performed at a grid resolution of 1024×1024. We use snapshots of the vorticity field, uniformly sub-sampled to a resolution of 128×128, to construct the vortical network. For three-dimensional isotropic turbulence, flow fields with $Re_\lambda(t_0) \approx 40$ are obtained from DNS performed with a grid resolution of $64 \times 64 \times 64$. The three-dimensional flow fields are uniformly sub-sampled to a resolution of $32 \times 32 \times 32$ for constructing the vortical network. Sub-sampling is performed in a manner such that the network representation is not influenced.

The network representation can be made independent of the Reynolds number following the non-dimensionalization of the edge weights using equation 2.6. We choose the characteristic velocity

$$u^* = V^{1/n_{\mathrm{d}}}\Omega_{\mathrm{tot}}^{1/2} = V^{1/n_{\mathrm{d}}}\left(\frac{\int_{\|\boldsymbol{\omega}\|_2 \geq \omega_{\mathrm{th}}} \|\boldsymbol{\omega}(\boldsymbol{r},t)\|_2^2 \, \mathrm{d}V}{V}\right)^{1/2}, \tag{3.12}$$

where Ω_{tot} is the total enstrophy per unit area or volume of all the vortical elements enclosed in a region of vorticity threshold ω_{th}. We concentrate on vortical elements with high vorticity [85], extracted through vorticity thresholding [67]. We can capture the overall interaction behavior of the flow field even with the threshold. For both two- and three-dimensional flow fields, we use a threshold of $\omega_{\mathrm{th}} = 0.05||\boldsymbol{\omega}(\boldsymbol{r})||_\infty$. Detailed assessment on the influence of the Reynolds number, grid, and ω_{th} is provided in Appendix C.

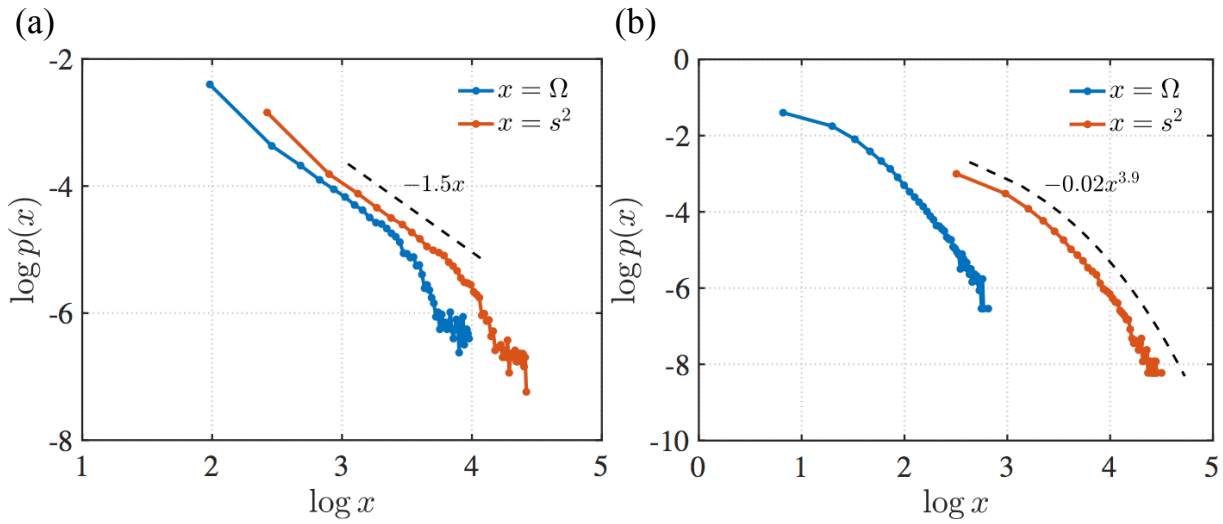

Figure 3.7: Enstrophy and node strength (squared) distributions of two- (a) and three-dimensional (b) isotropic turbulence.

3.2.2.2 Network characterization of isotropic turbulence

Let us first characterize the interactions amongst the vortical elements in two- and three-dimensional isotropic turbulence. Following equation 2.9, we evaluate the node strength and enstrophy distributions of the flow fields at an instant in time, presented in figure 3.7. The node strength-enstrophy relations from equation 2.9 is shown here for isotropic turbulence. Benzi *et al.* [12] found a power-law profile for the enstrophy distribution of two-dimensional decaying isotropic turbulence. The distribution $p(s^2)$ also follows a power-law behavior as observed in figure 3.7 (a). Taira *et al.* [133] analyzed the network structure of two-dimensional decaying isotropic turbulence and found the undirected node strength (average of in- and out-strength) distribution $p(s)$ to follow a scale-free behavior if the energy spectrum follows the k^{-3} profile.

For three-dimensional isotropic turbulence, the enstrophy distribution follows a stretched-exponential profile, $p(\Omega) \propto \exp(-a_\Omega \Omega^b)$ [29]. We observe a stretched exponential profile for $p(s^2)$ with the same exponent b as that of the enstrophy distribution, as shown in figure 3.7 (b). The difference of $p(s^2)$ for two- and three-dimensional flows can be attributed to the components of vorticity. For three-dimensional turbulence, vorticity is spread over wide scales of structures due to vortex stretching and tilting, which are absent in two-dimensional

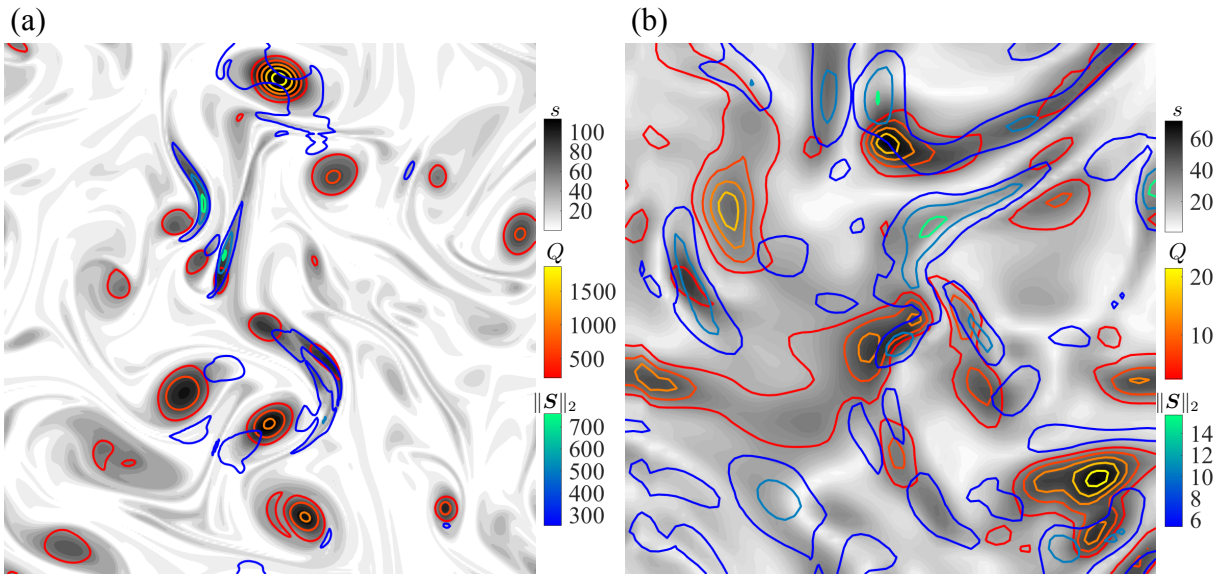

Figure 3.8: Comparing vortical structures with high node strength (gray contours), Q-criterion (red-yellow contours), and strain (blue-green contours) for (a) two- and (b) three--dimensional isotropic turbulence. Only a slice is shown for (b).

flows.

The node strength distributions can be used to highlight vortical elements with high node strength, as shown in figure 3.8. Isocontours of node strength, positive Q-criterion, and magnitude of strain rate tensor $\|\boldsymbol{S}\|_2$, for the two- and three-dimensional flow fields are shown. For both flows, the high node strength regions align with those of high positive Q-criterion (vortex core) and $\|\boldsymbol{S}\|_2$ (high shear regions). The node strength-enstrophy relation attributes to the alignment of the node strength with the Q and $\|\boldsymbol{S}\|_2$ measures in physical space. The observations show that the network-based node strength can indeed identify strong vortex cores and shear-layers in turbulent flows.

Let us now use the community-based framework to extract vortical communities in isotropic turbulence and identify influential regions to modify the flow using inter- and intra-community strength measures. A demonstration of the community detection algorithm and the corresponding $P-Z$ map applied to a three-dimensional flow field are shown in figure 3.9 (a) and (b). Here, the initial community detection procedure coarsely identifies regions in the flow field. A clear distinction between connectors and peripherals is not observed using the $P-Z$ map. The continuous nature of the flow field and vortical structures

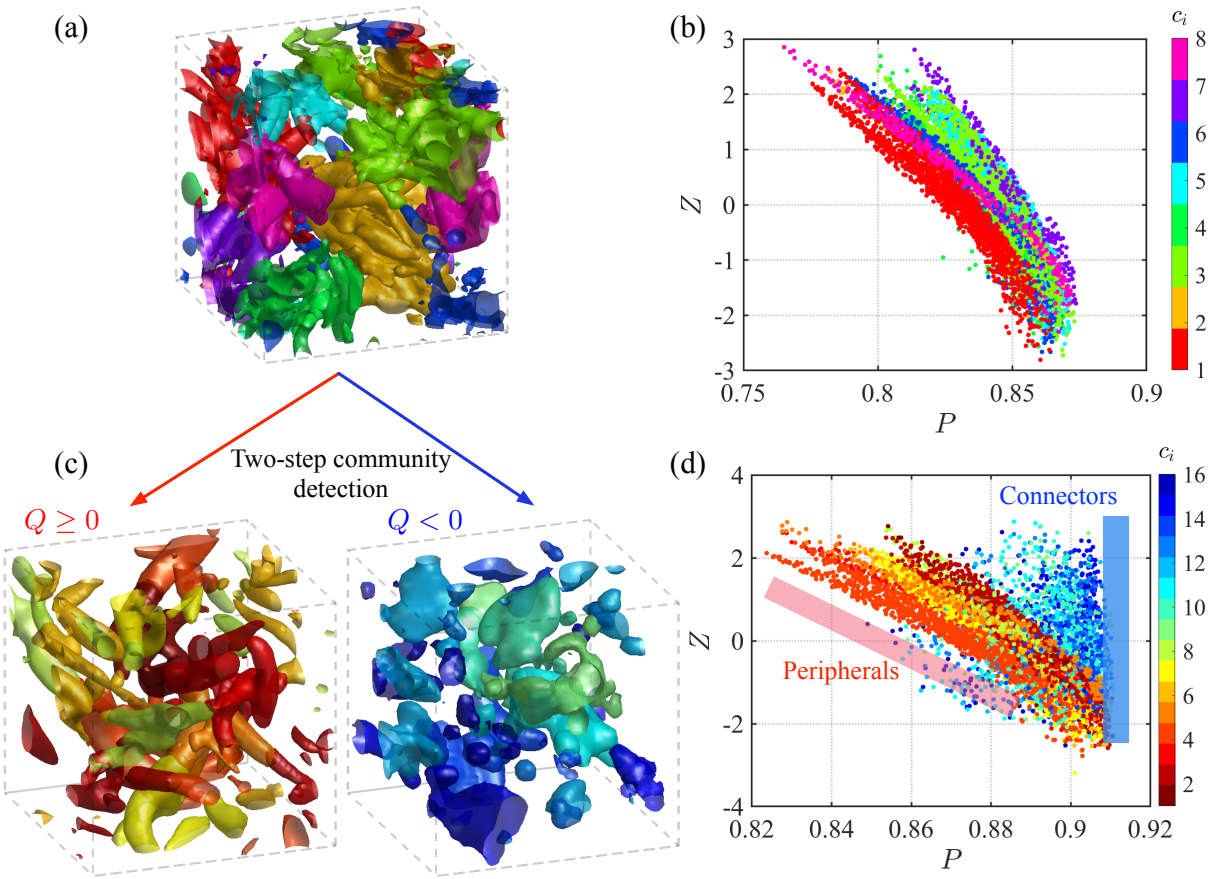

Figure 3.9: (a) Community detection in a three-dimensional isotropic turbulence and (b) the corresponding $P - Z$ map. (c) Two-step community detection and (d) the corresponding $P - Z$ map. Connector and peripheral communities have distinct distributions in the $P - Z$ map.

being spatially close to each other can make it challenging for the community detection algorithm to extract distinct vortical structures. Similar observations were made in a previous study for laminar wakes [38].

We aid the community detection algorithm by decomposing the flow field into nodes with $Q > 0$ and $Q < 0$. This is portrayed in figure 3.9 (c). The communities are identified independently for the two networks. The difference in the number of communities compared to the first step is due to the value of γ_{M} used, which was found to be similar for both the steps for the given Re_λ. The new community labels are used to evaluate the $P - Z$ map for the full adjacency matrix, as shown in figure 3.9 (d). The two-step community detection procedure reveals the communities to broadly follow two correlations in the $P - Z$ map. The

communities on the left side of the map possess a negative correlation in the $P - Z$ feature space and the nodes on the left side exhibit no significant correlation. We classify the former as peripheral and later as connector communities. The first group predominantly contains nodes with $Q > 0$, the second group with $Q < 0$. Thus, most peripheral and connector communities resemble vortex core and shear-layer type structures, respectively. Vortex cores that are spatially isolated in the flow can attribute to their classification as peripherals. Whereas, most shear-layer type structures being located amongst vortical structures make them connectors. We observe similar results for two-dimensional isotropic turbulence and for other cases at various Re_λ. Given the classification of vortical structures into connector and peripheral communities, we can now identify the important communities and analyze their influence on the flow field.

3.2.2.3 Turbulent flow modification

We compute the $\overline{P_k}$ of each community k to quantify the strength of influence. The connector and peripheral communities are the ones with $\max_k \overline{P_k}$ and $\min_k \overline{P_k}$, respectively, as highlighted in figure 3.10 (a). The dominant nodes of the communities are determined based on Z. The peripheral community corresponds to the vortical structure visualized in red and the connector community is comprised of low circulation multi-vortical structures with both strain and rotational regions visualized in blue in figure 3.10 (b).

We compare the influence of the connector structure to modify the flow with the strongest vortex tube and shear-layer based regions, which are known to cause high flow modifications. The vortex tube and shear-layer structures are identified by large amplitudes of $Q > 0$ and $Q < 0$, respectively, herein denoted as Q^+ and Q^-. We do not present cases for the peripheral structures as they usually align with Q^+.

We add perturbations to the identified influential structures and track the changes to the flow. Impulse perturbations at discrete time $n_\mathrm{t}\Delta t$ are added to the velocity field with time step Δt and $n_\mathrm{t} = 0, 1, 2, \ldots$. The perturbed velocity field at time t is given by $\boldsymbol{u}(\boldsymbol{r}, t) + \tilde{\boldsymbol{u}}(\boldsymbol{r}, \boldsymbol{r}^*, t)$, where $\tilde{\boldsymbol{u}}(\boldsymbol{r}, \boldsymbol{r}^*, t) = \alpha \tilde{\boldsymbol{f}}(\boldsymbol{r}, \boldsymbol{r}^*, t)$, α is the amplitude of the perturbation added

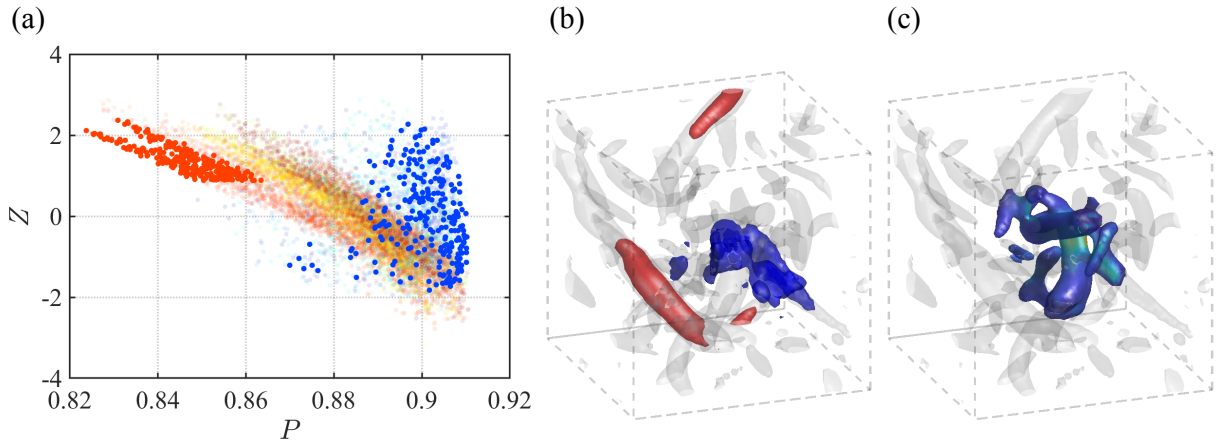

Figure 3.10: (a) Identifying the connector and peripheral in the $P - Z$ map and (b) the structures in physical space. (c) Local region around the connector structure.

to the perturbation $\tilde{\boldsymbol{f}}(\boldsymbol{r}, \boldsymbol{r}^*, t)$, and $\boldsymbol{r}^*$ is the location of the influential structure. The perturbation is given by

$$\boldsymbol{f}(\boldsymbol{r}, \boldsymbol{r}^*, t) = \frac{\hat{\boldsymbol{e}}_{\boldsymbol{u}(\boldsymbol{r},t)}}{\sqrt{2\pi\Delta V^2}} \sum_{i=1}^{n_\mathrm{p}} \exp\left(\frac{-\|\boldsymbol{r} - \boldsymbol{r}_i^*\|_2^2}{2\Delta V^2}\right) \delta(t - n_\mathrm{t}\Delta t), \tag{3.13}$$

where $\hat{\boldsymbol{e}}_{\boldsymbol{u}(\boldsymbol{r},t)}$ is the unit vector in the direction of $\boldsymbol{u}(\boldsymbol{r}, t)$, ΔV is the volume of the vortical node (grid size), and $\boldsymbol{r}_i^*$ are the locations of the n_p perturbed nodes. We normalize $\boldsymbol{f}(\boldsymbol{r}, \boldsymbol{r}^*, t)$ to give $\tilde{\boldsymbol{f}}(\boldsymbol{r}, \boldsymbol{r}^*, t)$ such that $\int_V \|\tilde{\boldsymbol{f}}(\boldsymbol{r}, \boldsymbol{r}^*, t)\|_2^2 \mathrm{d}V = 1$. A prescribed forcing energy E of

$$E = \frac{\int\limits_V \|\tilde{\boldsymbol{u}}(\boldsymbol{r}, \boldsymbol{r}^*, t)\|_2^2 \mathrm{d}V}{\int\limits_V \|\boldsymbol{u}(\boldsymbol{r}, t)\|_2^2 \mathrm{d}V} \tag{3.14}$$

is used to compute the amplitude of perturbation α.

We first analyze the influence of the structures with a single perturbation at the initial time. The perturbation amplitude α is chosen such that $E = 0.04$, which is a reasonable magnitude for control. Based on the observations, we then employ multiple pulses. The influential structures are tracked in time for given isocontours (or isosurfaces) of Q-criterion and are subjected to impulse perturbations with time step $\Delta t/\tau_e(t_0) = 1$ and 0.2 for two- and three-dimensional flows, respectively. We have chosen the time step for these turbulent

flows based on the single perturbation analysis to obtain significant flow modification. The difference in time step for two- and three-dimensional isotropic turbulence is to consider the distinct predictability horizon of small-scale motion in the flows [86, 80, 84]. While the two-dimensional flow would have predictability horizons spanning over a few eddy turn-over times, the present three-dimensional flow has a shorter time horizon.

We concentrate on the flow evolution around the neighbourhood of the perturbed structures, as shown in figure 3.10 (c). The peripheral-based or Q^+ perturbations increases the circulation of the vortex core. In contrast, modification of the behavior of multiple vortical structures by the connector-based and Q^- perturbations enhances local mixing in the flow, as we discuss below. Based on the observations from the present study (for which the influential structures are identified only at initial time), we have also performed preliminary analyses with the structure identification procedure repeated as the flow evolves. We observe similar results showing perturbation of the connector structures significantly enhancing turbulent mixing compared to perturbing Q^+ and Q^- structures. In the present study, we concentrate on the structures identified at initial time to characterize the influence of the network-based structures on turbulence.

Local mixing enhancement

Mixing enhancement in turbulent flows plays a key role in various engineering applications. Mixing enhancement by stirring have been attributed to generation of shear dominated filaments in the flow field [126, 4, 112, 32]. Here, we analyze the effect of the perturbations to enhance local mixing in isotropic turbulence based on the present network-based framework. We use fluid particle tracking to quantify local mixing in the flow field. To quantify mixing, we consider the use of two-species fluid tracking [27]. The first species is initialized one integral length scale around the centroid of the perturbed structure, the region previously shown in figure 3.10 (c), and the second over the rest of the flow field. Given the velocity

field $\boldsymbol{u}(\boldsymbol{r}, t)$, the time evolution of the fluid particle at $\boldsymbol{r}_p$ is given by

$$\frac{\mathrm{d}\boldsymbol{r}_p}{\mathrm{d}t} = \boldsymbol{u}(\boldsymbol{r}_p, t). \tag{3.15}$$

A second-order accurate Runge–Kutta scheme is implemented for time integration [138].

Local mixing is quantified by measuring the information entropy using the two species of particles in the domain [72, 26]. The flow field is discretized into cells and the entropy of the two species of particles is evaluated for each cell. The total information entropy of the whole domain at an instant in time is given by

$$S = -\sum_{i=1}^{n_\mathrm{c}} \left[w_i \sum_{k=1}^{2} \left(n_{i,k} \log n_{i,k} \right) \right], \tag{3.16}$$

where n_c is the number of cells with which the full domain is discretized, $n_{i,k}$ is the number of particles of kth species in ith cell, and w_i is the weight factor. If the ith cell contains no particles or only particles of a single species, $w_i = 0$, else $w_i = 1$. Moreover, the relative entropy measure κ [72] is given by

$$\kappa(t) = \frac{S(t) - S(t_0)}{S_\mathrm{max} - S(t_0)}, \tag{3.17}$$

where $S(t_0)$ is the entropy for initial particle distribution and S_max is the maximum possible entropy increase over the domain, which is achieved when each cell contains equal number of particles of each species. For each perturbation setup, we normalize κ by the baseline κ_base as $\tilde{\kappa}(t) = \left[\kappa(t) - \kappa_\mathrm{base}(t)\right] / \|\kappa_\mathrm{base}(t)\|_\infty$, thus measuring the mixing enhancement compared to the baseline flow. The baseline flow field is initialized with particles in the same pattern as each perturbed simulation to evaluate the respective κ_base.

Ensemble averages of $\tilde{\kappa}$ for connector, Q^+, and Q^--based perturbations performed on a number of two- and three-dimensional isotropic turbulent flows are shown in figure 3.11. For the two-dimensional isotropic turbulence with a single perturbation at initial time, the connector-based perturbation achieves mixing enhancement similar to that of Q^-. Both connector-based and Q^- perturbations outperforms Q^+ for local mixing enhancement. With

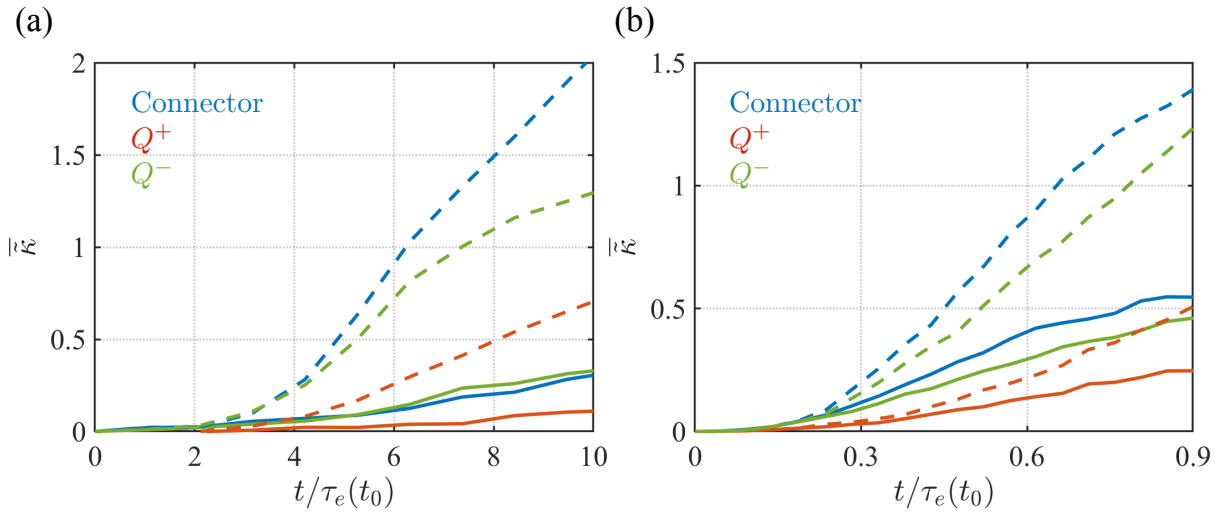

Figure 3.11: Ensemble average of normalized relative particle entropy in time for (a) two- and (b) three-dimensional isotropic turbulent flows subjected to connector-based, Q^+, and Q^- perturbations. Lines — denote results for single perturbation and −− for multiple perturbation. Ensemble is computed using 10 cases.

multiple pulses, connector-based perturbation generates entropy two times compared to the baseline flow, which is 54% more than the Q^- perturbations. The perturbation using Q^+ just leads to strengthening of vortex cores without significant spreading of particles, which will be visualized shortly.

Using the results of two-dimensional flows as a guideline, we perform the analysis on three-dimensional flows, as shown in figure 3.11 (b). A single pulse add to the connector at initial time generates $\tilde{\kappa}$ values 0.55 times that of the baseline flow, which is 20% more than Q^- perturbation. With multiple pulses, connector-based perturbations increase the entropy by 1.4 times compared to the baseline flow, which is 17% more than the Q^- perturbations. Multiple pulses of Q^+ perturbation under-performs compared to even the single connector-based perturbation. According to the studies on mixing enhancement using stirrers [4, 32], we expect the Q^- perturbation to achieve better mixing. The present results are in agreement with these studies.

With the above observations quantifying the effectiveness of connectors to modify turbulence and enhance local turbulence mixing, let us analyze the flow fields. We consider the time evolution of a two-dimensional isotropic decaying turbulent flow subject to mul-

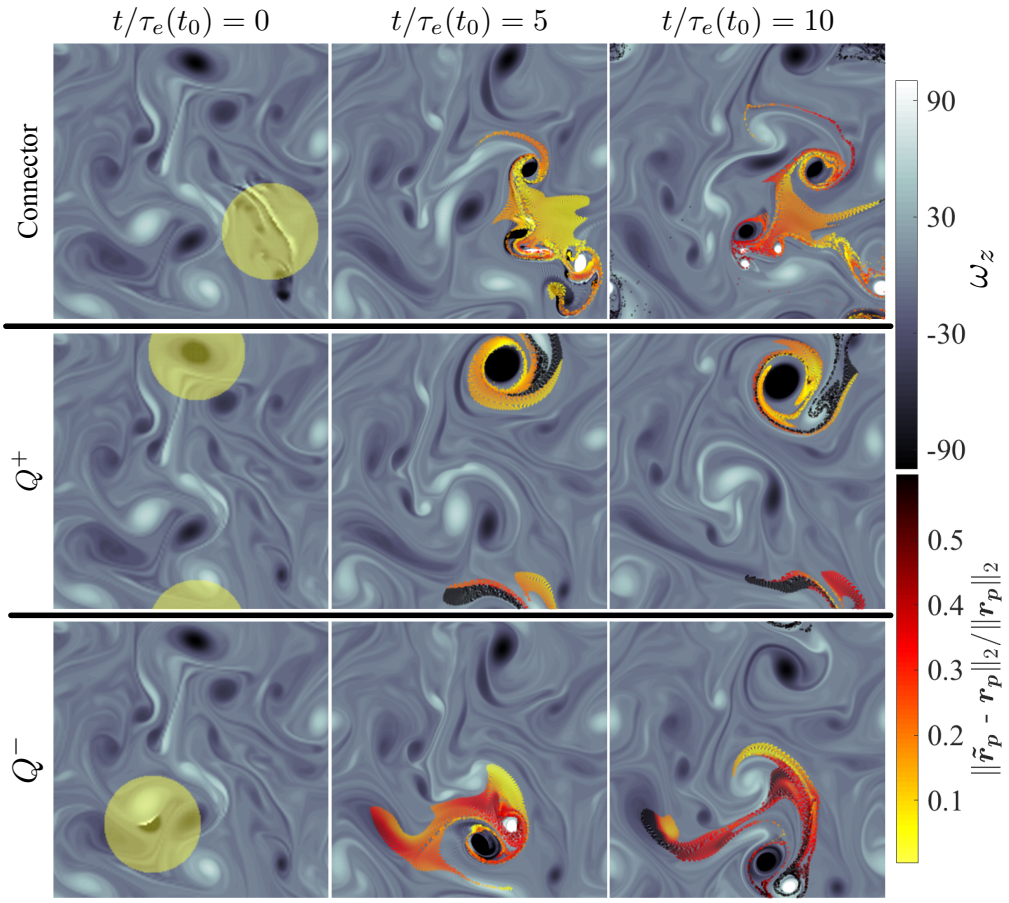

Figure 3.12: Time evolution of a two-dimensional isotropic turbulent flow subjected to multiple perturbations. Fluid tracers initialized around the perturbation are coloured by the change in trajectory compared to the corresponding baseline trajectory.

tiple pulses of connector-based, Q^+, and Q^- perturbations, as shown in figure 3.12. The fluid particle species initialized one integral length around the perturbation is shown. The yellow-red colour gradient represents the amount of change in trajectories compared to the corresponding baseline trajectory. A uniform colour distribution indicates effective mixing. The connector-based perturbation achieves the narrowest range in colour distribution at the final instant. Whilst Q^+ and Q^- perturbations achieve higher magnitudes of change in trajectories for certain particles, highlighted in black, some particles are spread out least, as highlighted in bright yellow.

Multiple pulses on the Q^+ structure strengthens the vortex core, making a large distinct vortex. The tracers rotate around the vortex core due to the vorticity. Only the tracers at the boundary of the vortex are spread out significantly. The Q^- perturbation, comprising

of the strained region between the vortex-dipoles, forms a jet-like flow. With multiple perturbations, the jet-like flow spreads the tracers more effectively compared to that achieved in the baseline and Q^+ perturbations. These observations are in agreement with recent findings that vortex-dipole like structures in two-dimensional isotropic turbulence promote effective flow modification [66]. The connector structures are comprised of a long shear-layer type vortical structure and near-by vortices of low vorticity. Multiple perturbations of the shear-layer type structure lead to the formation of small scale vortices, which enhances flow mixing compared to the baseline as well as Q^+ and Q^- perturbations.

The evolution of particle tracers in a three-dimensional turbulent flow subjected to multiple perturbations on connector, Q^+, and Q^- structures are presented in figure 3.13. Here, the Q^+, Q^-, and connector structures are spatially located close to each other at the initial time. The flow field at the final instant corresponding to connector-based perturbation has the narrowest range in colour distribution of the tracers, depicting highest mixing enhancement. The broadest range in colour distribution corresponds to Q^+ perturbation, which denotes the least mixing enhancement achieved. Multiple pulses of connector-based perturbations lead to the generation of small scale structures. On the other hand, the vortical structures decay in time with Q^+ and Q^- perturbations.

Next, let us examine the local flow region around the perturbation to analyze the effect of the network-based connector to modify its neighbouring vortical structures. We analyze the time evolution of the local flow region around the connector, Q^+, and Q^- structures, as presented in figure 3.14. The vortical structures are tracked using the isosurface of Q-criterion, with a constant value of Q in time. A single pulse is added to the connector, Q^+, and Q^- structures at the initial time. The perturbed structures at the initial time are shown on the left column, visualized by the green isosurfaces. The neighbouring vortex tubes under consideration in each case (row) are depicted by the blue and red isosurface. The growth of maximum enstrophy, $\|\Omega\|_\infty$, is also evaluated to observe modification of the vortex cores [33, 6]. We note that at time $t/\tau_e(0) = 0.34$, the connector structure leads to modification of both the neigboring vortex tubes and formation of smaller scale structures. These small-scale structures induce enhanced local spreading of the fluid particles, as observed in figure 3.13.

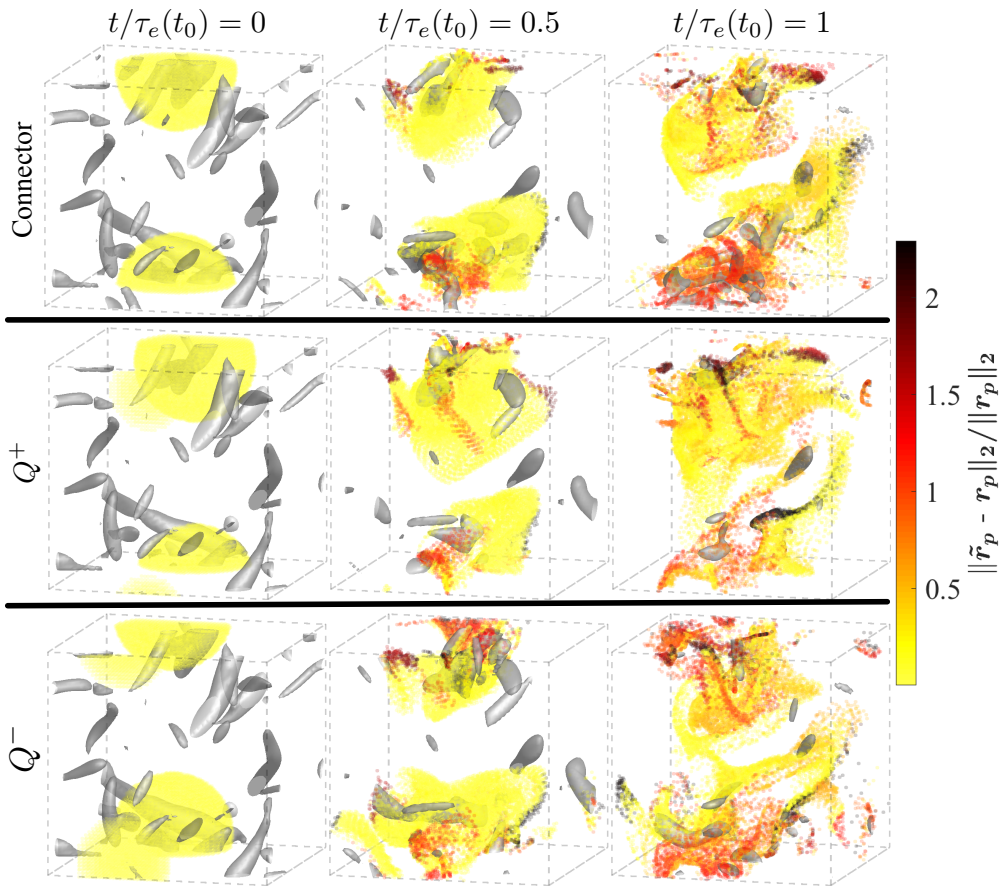

Figure 3.13: Time evolution of a three-dimensional isotropic turbulent flow subjected to multiple perturbations. Vortical structures are depicted by isosurface of Q-criterion. Fluid tracers initialized around the perturbation are coloured by the change in trajectory compared to the corresponding baseline trajectory.

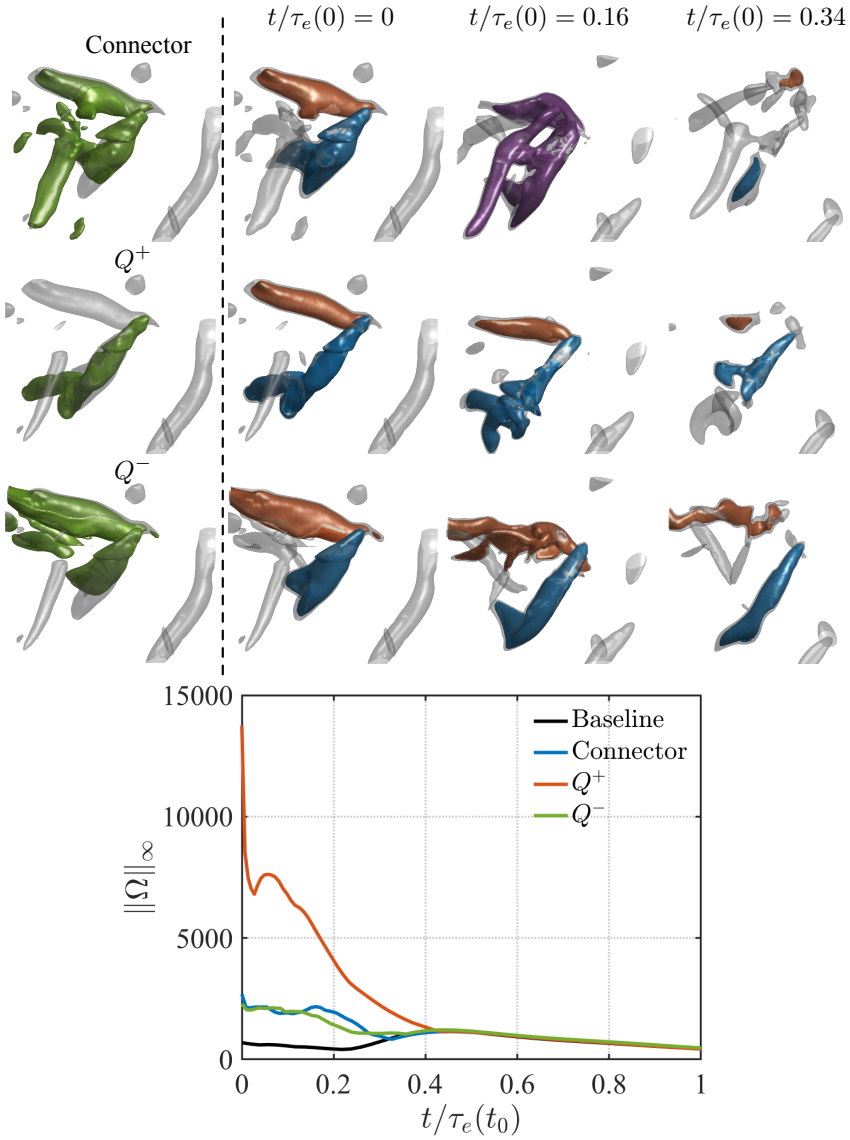

Figure 3.14: Modification of two vortex tubes in a three-dimensional isotropic turbulent flow using Q^+, Q^-, and connector-based perturbations. The connector effectively modifies both the vortex cores as shown using the isosurface of Q-criterion and local growth of maximum enstrophy $\|\Omega\|_\infty$ between time $t/\tau_e(0) = 0.12$ and 0.2.

Perturbation of the Q^+ structure (shown in blue) leads to the increase in circulation of the vortex core and eventual break-up of the blue isosurface at time $t/\tau_e(0) = 0.16$. The modification of the Q^+ structure is also observed by the peak of $\|\Omega\|_\infty$ at $t/\tau_e(0) = 0.05$. The curved geometry of the Q^+ vortex core at the initial time may instigate instabilities when perturbation is added, resulting in the significant modification of the vortex core. Nonetheless, the Q^+ perturbation has negligible influence on the neighbouring vortex highlighted in red. Note that these observations are similar to the characteristics of a network-based peripheral structure. The Q^- structure is the strongest shear-layer structure, which is located between the two neighbouring vortex tubes. Thus, the Q^- perturbation results in the modification of both the blue and red isosurfaces. Both the vortex cores decay in time with no peaks appearing for $\|\Omega\|_\infty$ over time, suggesting lower modification of the vortex cores achieved by the Q^- structure compared to Q^+ perturbation.

The connector structure is comprised of the shear-layer region between the two neighbouring vortex tubes and an adjacent vortical structure with low circulation. This adjacent vortical structure merely decays within a short time in the Q^+ and Q^- simulations. With connector-based perturbation, the adjacent vortical structure connects with the two neighbouring vortex tubes through the shear-layer, forming one large vortical structure highlighted in purple at time $t/\tau_e(0) = 0.16$. Eventually, the connection results in the significant break-up of both the blue and red isosurfaces, leading to the formation of smaller scales of vortical structures. The observations show the advantage of connectors to modify multiple vortical structures compared to Q^+ perturbations. The local growth of $\|\Omega\|_\infty$ between $t/\tau_e(0) = 0.13$ and 0.2 denotes effective modification of the vortex cores compared to that achieved by Q^- perturbation. The connection amongst the vortical structures, in the form of vorticity, is not aligned with the direction of rotation of the two neighbouring vortex tubes, which may result in instabilities, leading to significant break-up of the vortex cores. The above illustrative examples demonstrate the ability of network-based methodologies to extract vortical structures of low circulation that can effectively influence neighbouring vortical structures in turbulent flows.

CHAPTER 4

Concluding remarks

4.1 Summary

A network community-based formulation was introduced for reduced-order modelling and extracting flow modifying structures in laminar and turbulent flows. Network theory was used to represent the vortical interactions in two- and three-dimensional laminar and turbulent flows, namely discrete point vortex system, laminar wake flows, and decaying isotropic turbulence, as a vortical network. The network framework considered the vortical elements in a flow as nodes of a graph and captured the web of interactions amongst them, quantified by the induced velocity, as the weighted edges. The full vortical network representation (following either an Eulerian or Lagrangian description) was used to identify the communities or modular structures in the unsteady flows through the modularity maximization algorithm. The general dynamics equation for a networked system was recast using the community information to obtain reduced-order models and modify the system dynamics.

A network-community based reduce-order formulation was considered to distill the high-dimensional complex nonlinear interactions in unsteady vortical flows. We collapsed the full vortical network through the centroid of each communities, considerably reducing the dimension of the fluid flow. Furthermore, we extended the formulation to model and predict observable variables of the system, such as lift and drag on bodies, relying solely on the community-centroid properties. The network-community based reduce-order formulation was applied to canonical vortical flow problems for validation. First, the current approach was applied to model the dynamics of a collection of discrete point vortices. Instead of tracking the dynamics of a large number of vortices, the overall dynamics of the discrete

vortex communities was modeled using community-based networked dynamics. Second, we have also modeled the lift and drag on bodies in wake flows using the community-based reduced-order formulation. Relying on the properties of the community centroids in the wake, models predicting lift and drag on the body were formulated through nonlinear regression analysis. These formulations were applied on the two-dimensional flow field data of flow over a circular cylinder and an airfoil with a Gurney flap. The community-based formulation was able to effectively identify the key vortical communities in both the wake flows. Also, the reduced-order force model could predict lift and drag forces on the cylinder as well as airfoil with considerable accuracy. The resilience of these formulations against perturbations or noise were also examined by adding artificial noise to the input data to simulate experimental noise or turbulence. The proposed formulation can serve as a basis to tackle highly chaotic and aperiodic flows. However, it is likely that techniques such as uncertainty quantification needs to be incorporated to assess the confidence of the model.

Furthermore, we decomposed the governing equation for a networked system using the intra- and inter-community interactions. The strengths of these interactions were used to identify the connector and peripheral nodes, which have the highest and least influence on other communities, respectively. The node with the maximum total interaction strength was identified as the hub. The ability of these influential nodes to modify the networked dynamics was demonstrated on a model fluid flow of a collection of discrete point vortices. Impulse velocity perturbations were added to the connector, peripheral, and hub nodes identified at the initial time. The connector community effectively modified trajectories of the other communities compared to the hub and peripheral-based perturbations. We then applied the community-based formulations to identify influential structures in two- and three-dimensional isotropic turbulence. The connector and peripheral structures were found to resemble shear-layer and vortex core type structures, respectively. Adding perturbations to the connector structures, which have low vorticity, led to enhanced local flow mixing compared to the effect of perturbing the strongest shear-layer and vortex tube.

4.2 Broader impacts and future work

The demonstrations of the community-based formulations, even though considered only for fluid flow problems in the current work, have implications to applicability to high-dimensional, nonlinear systems with intrinsic community-based coherent structures. Recently, we are applying the community-based formulations to explore clustering of particles in three-dimensional particle-laden turbulence [8]. Detailed assessment of the life time of particle clusters can be revealed by quantifying the interactions amongst the clusters. Efforts are also taking place to incorporate the Lagrangian coherent structure extraction technique to aid the community-detection procedure in turbulent flows [97]. Our study alludes towards using the reduced-order methodology in effectively tracking the overall dynamics of such systems and modeling observable variables. Furthermore, these models can possibly be influenced by altering the interactions among the elements in the system. Coupling the formulations for the dynamics and observable variables may also motivate studies on closed-loop control by altering the inter-community interactions as demonstrated for open-loop control by community-based flow modification. Within the current work, we have not addressed the necessary computational effort for performing the network-based analysis. However, there are emerging network-based characterization [7] and modeling techniques [94] for fluid flows that can be leveraged to perform the present analysis with reduced computational resource. With these developments, the present characterization and open-loop control offers a pathway for future closed-loop flow control efforts to modify the dynamics of vortical structures residing in a complex turbulent flow field.

APPENDIX A

Analytical vortex solutions and network strength

Using equations 2.5 and 2.9, the node strength for vortical elements in two-dimensional flows is given by

$$s_i = \frac{\omega_{z,i}\mathrm{d}x\mathrm{d}y}{2\pi}\sum_j \frac{1}{\|\Delta \boldsymbol{r}_{ij}\|_2}. \tag{A.1}$$

For the Lamb–Oseen type of vortices, the vorticity distribution is given by

$$\omega_z(r,t) = \frac{\Gamma}{2\pi r_c^2(t)}\exp\left(-\frac{r^2}{r_c^2(t)}\right). \tag{A.2}$$

where $r_c = \sqrt{4\nu t + r_c(0)^2}$ is the core radius of the vortex. The strength of nodes in such a flow field is given by

$$s(r) = C_1 \exp\left(-\frac{r^2}{a^2}\right) \tag{A.3}$$

for a particular instant in time, where $a = r_c$ and

$$C_1 = \frac{\Gamma}{2\pi a^2}\left(\frac{\mathrm{d}x\mathrm{d}y}{2\pi}\sum \frac{1}{\|\Delta \boldsymbol{r}\|_2}\right). \tag{A.4}$$

Let X be an absolutely continuous random variable with support R_X and probability density function (pdf) $f_X(x)$, and g be a function monotonously decreasing and differentiable on the support of X. Then, for $Y = g(X)$, the support of Y is

$$R_Y = \{y = g(x) : x \in R_X\} \tag{A.5}$$

and the pdf of Y is

$$f_Y(y) = \begin{cases} -f_X(g^{-1}(y))\frac{\mathrm{d}g^{-1}(y)}{\mathrm{d}y} & \text{if } y \in R_Y \\ 0 & \text{if } y \notin R_Y. \end{cases} \tag{A.6}$$

Now, for the strength of nodes, we have an invertible, monotonously decreasing form

$$\begin{aligned} s &= g(r) = C_1 \exp(-\frac{r^2}{a^2}) && \text{(A.7)} \\ \Rightarrow \log s &= \log C_1 - \frac{r^2}{a^2} && \text{(A.8)} \\ \Rightarrow r &= \left[C_2 - a^2 \log s\right]^{1/2} = g^{-1}(s) && \text{(A.9)} \end{aligned}$$

where $C_2 = \log C_1 a^2$. Thus, the pdf of s is given by

$$\begin{aligned} f_S(s) &= \begin{cases} -f_{RR}(g^{-1}(s))\frac{\mathrm{d}g^{-1}(s)}{\mathrm{d}s} & \text{if } s \in R_S \\ 0 & \text{if } s \notin R_S \end{cases} && \text{(A.10)} \\ &= \begin{cases} -f_{RR}(r)\frac{\mathrm{d}g^{-1}(s)}{\mathrm{d}s} & \text{if } s \in R_S \\ 0 & \text{if } s \notin R_S \end{cases} && \text{(A.11)} \\ \text{OR} \quad &= \begin{cases} -F'_{RR}(r)\frac{\mathrm{d}g^{-1}(s)}{\mathrm{d}s} & \text{if } s \in R_S \\ 0 & \text{if } s \notin R_S \end{cases}. && \text{(A.12)} \end{aligned}$$

Now, to find $f_{RR}(r)$ or $F_{RR}(r)$, we take the probability of finding a random point in a circular or square two-dimensional domain or a spherical or cubic three-dimensional domain, with a characteristic length (radius or length of square) of D. The cumulative density function of a point inside the circle at a distance r from the center is given by

$$F_D(r) = P(D \leq r) = \frac{\text{area of circle with radius } r}{\text{total area of circle}} = \frac{r^2}{D^2}. \tag{A.13}$$

For a sphere, this would be $F(r) = r^3/D^3$. Thus, we can obtain the pdf as

$$f_D(r) = F'(r)\mathrm{d}r \tag{A.14}$$

$$= \begin{cases} \frac{2r}{D^2} & \text{for 2D} \\ \frac{3r^2}{D^3} & \text{for 3D} \end{cases}. \tag{A.15}$$

Also, for the Lamb–Oseen vortex considered,

$$\frac{\mathrm{d}g^{-1}(s)}{\mathrm{d}s} = -\frac{a^2}{2s}\left(C_2 - a^2 \log s\right)^{-1/2}. \tag{A.16}$$

Thus, the pdf of node strength for the Lamb–Oseen vortex is given by

$$f(s) = \begin{cases} \frac{a^2 r}{D^2 s}\left(C_2 - a^2 \log s\right)^{-1/2} & \text{if } s \in R_S \\ 0 & \text{if } s \notin R_S \end{cases} \tag{A.17}$$

$$= \begin{cases} \frac{a^2}{D^2} s^{-1} & \text{if } s \in R_S \\ 0 & \text{if } s \notin R_S \end{cases} \left(\because r = \left[C_2 - a^2 \log s\right]^{1/2}\right). \tag{A.18}$$

Thus, we can write $p(s) = Cs^{-1}$ which follows the power-law distribution observed through the numerical solution to the strength distribution shown in figure A.1. The distribution is also observed for other analytical vortex solutions and laminar wakes.

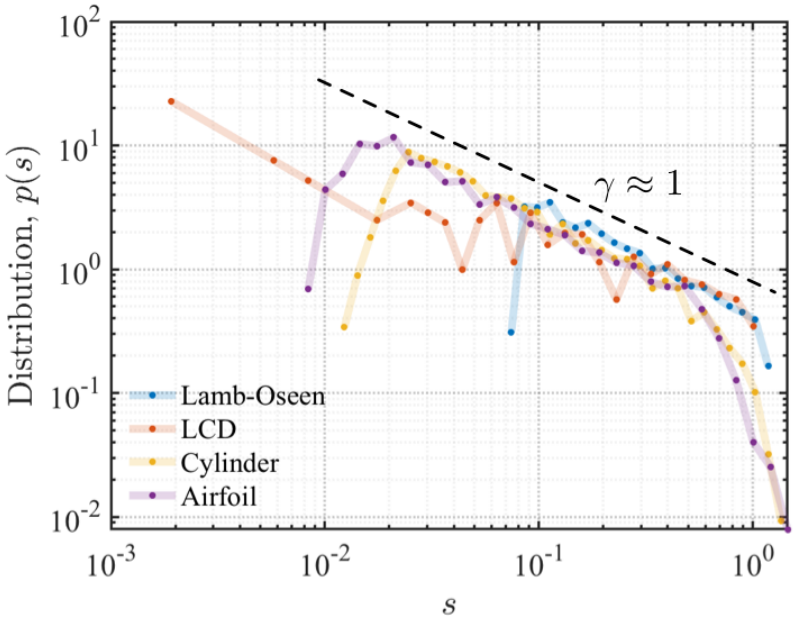

Figure A.1: Strength distribution of analytical and laminar wake flows.

APPENDIX B

Airfoil wake modification with Gurney flap at low-Reynolds number

In the present chapter, which is excerpted from our previous publication [41], we perform an extensive parametric study to examine the influence of Gurney flap on the aerodynamic characteristics and two-dimensional wake patterns behind NACA 0000, 0006, 0012 and 0018 airfoils. In the section below, the computational approach and setup for the study is described. This is followed by the discussion of results from two-dimensional direct numerical simulations (DNS) in Section B.2, where we first classify the four characteristic wake modes observed. A detailed discussion of each wake mode is also provided. We then examine the effects of the Gurney flap on lift, drag and lift-to-drag ratio for all airfoils. We also provide in Section B.3 a brief analysis on the spanwise effects on the wake modes by performing companion three-dimensional simulations. Concluding remarks are offered at the end of the paper to summarize the findings and to discuss potential uses of Gurney flaps.

B.1 Computational approach

Two-dimensional DNS

We investigate the influence of Gurney flaps on the two-dimensional wake behind four different symmetric airfoils of NACA 0000 (flat plate), 0006, 0012 and 0018 at a chord-based Reynolds number of $Re \equiv u_\infty c/\nu = 1000$. Wide range of values for the Gurney flap height and angle of attack are considered in this study for the setup shown in figure B.1(a). The flow field and force data obtained for each case are analyzed in detail to acquire a knowledge

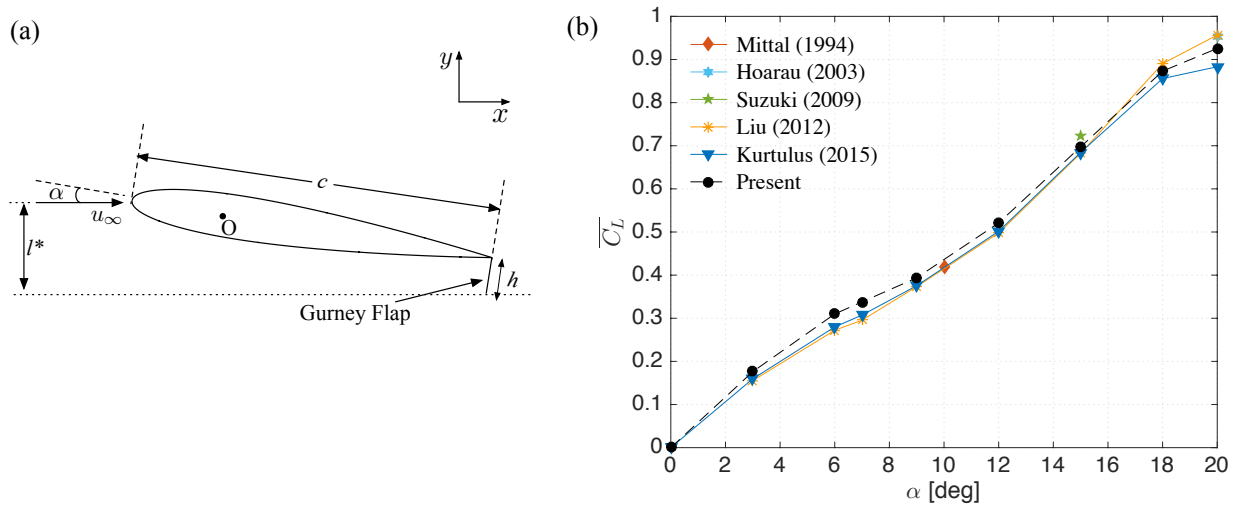

Figure B.1: (a) A representative setup with NACA 0012 airfoil at $\alpha = 9°$ with Gurney flap of $h/c = 0.1$ attached to the trailing-edge; (b) comparison of mean lift coefficient, $\overline{C_L}$, for NACA 0012 airfoil at $Re = 1000$ with previous studies in literature [87, 56, 128, 82, 77].

on the underlying effect of flow control from the use of the Gurney flap on the airfoils for aerodynamic performance enhancement.

The problem setup for the current work is depicted in figure B.1(a). Throughout this paper, the length, time, and velocity are non-dimensionalized by the chord length c, convective time scale c/u_∞, and the free stream velocity u_∞, respectively unless otherwise noted. Angles of attack α between 0° to 20° are considered for all the airfoils, of which Gurney flap is attached to the trailing-edge perpendicular to the chord line. For all cases, Gurney flap height of h/c between 0 to 0.15 are considered. The wing is placed in the domain with its quarter chord at the origin with uniform flow prescribed at the inlet.

For the current analysis, the immersed boundary projection method [130, 25] is used to simulate the flow. This method is based on a finite volume formulation and incorporates the no-slip boundary condition along the immersed boundary into the projection operation. The scheme is second-order accurate in time and has a spatial accuracy of higher than first-order in the L_2 norm. Moreover, a multi-domain technique is used to simulate the flow over a body in free space. The scheme has been validated for a number of cases [131, 63], and has been found robust and accurate [25]. Five nested levels of multi-domains

are used with the finest level being $(x/c, y/c) \in [-1, 1] \times [-1, 1]$ and the largest domain being $(x/c, y/c) \in [-16, 16] \times [-16, 16]$ in size. The time step for all cases is limited to a maximum CFL number of 0.3.

In the current study, the drag and lift coefficients are defined as

$$C_D \equiv \frac{F_x}{\frac{1}{2}\rho u_\infty^2 c} \quad \text{and} \quad C_L \equiv \frac{F_y}{\frac{1}{2}\rho u_\infty^2 c}, \tag{B.1}$$

respectively. The shedding frequency f_s of lift is non-dimensionalized as the Strouhal number

$$St \equiv \frac{f_s l^*}{u_\infty}, \tag{B.2}$$

where the characteristic frontal length l^* is taken to be

$$l^* = c \sin(\alpha) + h \cos(\alpha), \tag{B.3}$$

as illustrated in figure B.1(a). Grid convergence study was performed on the NACA 0012 airfoil without a flap at $\alpha = 10^\circ$ for grid size ranging from 200×200 to 500×500. A domain with 360×360 grid resolution was found to be sufficient with less than 1% error in $\|C_L\|_\infty$ and St values, also capturing the wake structures effectively. Figure B.1(b) shows the comparison of mean C_L values of NACA 0012 airfoil at $Re = 1000$ with past studies [87, 56, 128, 82, 77]. The results obtained from the current simulations are in agreement with the data from literature.

Three-dimensional DNS

We also perform three-dimensional direct numerical simulations on selected cases from the two-dimensional analysis to acquire an understanding of the spanwise effects on the wakes. The analysis is performed on the NACA 0006 airfoil with Gurney flap of $h/c = 0.08$ and $\alpha = 6^\circ, 12^\circ$ and 18° at $Re = 1000$. The cases are selected to represent the characteristic wake modes observed from the two-dimensional analysis. We use a finite-volume incompressible flow solver, Cliff (CharLES software package), developed by Stanford University and Cascade

Technologies to solve the three-dimensional incompressible Navier–Stokes equation [52, 53, 89, 73]. A spatial domain of $(x/c, y/c, z/c) \in [-30, 30] \times [-30, 30] \times [0, 4]$ is considered. The spanwise extent of $4c$ is chosen based on three-dimensional analysis for the baseline cases without Gurney flap at similar Re range [98, 110]. A two-dimensional unstructured spatial grid discretization is utilized and extruded in the spanwise direction with $\Delta z/c = 0.0625$. The largest non-dimensional wall spacings along the suction side of the airfoil are $\Delta x = 0.004,\ \Delta y = 0.007$ and $\Delta z = 0.0625$. The time step for all the simulations is set to a maximum CFL number of 1.0. No-slip boundary condition is specified on the airfoil and Gurney flap surfaces. An inflow boundary condition of $\boldsymbol{u}/u_\infty = (1, 0, 0)$ is prescribed at the inlet and symmetric boundary conditions at the far-field boundaries (top and bottom). A convective outflow boundary condition is specified at the outflow to allow the wake structures to leave the domain without disturbing the near-field solution. The flow is set to be periodic in the spanwise direction.

A three-dimensional perturbation is introduced to ensure the three-dimensional structures are sufficiently developed. Temporal convergence of the simulations is ensured through the rms and time-averaged values of pressure and velocities, obtained from a probe data located at the mid-span and $1c$ downstream of the trailing edge, having variations less than 2% in time. The solver is validated with previous studies in literature [82, 77] and current two-dimensional analysis for the NACA 0012 airfoil at $\alpha = 20^\circ$ with the time-averaged $\overline{C_L}$ having less than 2% difference.

B.2 Analysis of two-dimensional flows

Findings from the two-dimensional numerical experiments performed for flow over the four NACA airfoils with and without the Gurney flap attached to the trailing edge are discussed here. The addition of the Gurney flap and changes in angle of attack and airfoil thickness bring about various changes to the aerodynamic forces experienced by the airfoils. These variations in the aerodynamic forces are caused by the flow modifications to the airfoil wake. The observations on the airfoil wake modifications are first discussed followed by detailed

analysis of the wake dynamics involved through the wake modifications. The effects on the aerodynamic forces are analyzed towards the end of this section.

Wake mode classification

First, let us analyze the vorticity field around the airfoils at $Re = 1000$ for various Gurney flap heights and angles of attack. We observe the formation of four distinct types of wakes develop over the airfoil both with and without the Gurney flap.

The numerical simulations reveal that the flow fields can be characterized into four different regimes depending on the characteristics of vortex shedding. The far field wake developments of different regimes for a representative airfoil setup (NACA 0000 with Gurney flap of $h/c = 0.06$) are summarized in figure B.2. The four types of flow regimes observed are:

- Steady;
- 2S - periodic von Kármán vortex shedding;
- P - periodic shedding of single vortex pairs; and
- 2P - periodic shedding of two distinct vortex pairs.

These wake modes are classified on the basis of the flow structure of the wake, vortex shedding frequency and force fluctuations. In this section, we discuss the difference in the flow structure of the wake modes along with the vortex shedding frequencies corresponding to each mode. The frequency spectra of the lift history for selected cases of all airfoils are depicted in figure B.3. Sampling time sufficient to capture 30-50 dominant shedding cycles is used to perform the spectral analysis. The flow transition through the regimes are clearly evident by the abrupt changes in the St values with α for NACA 0000 case.

The nomenclature of the modes follows the wake mode classification performed by Williamson and Roshko [136] on the analysis of wakes behind a cylinder in forced oscillation. The wake modes observed in the current study correspond to the 2S, P and 2P wake modes defined

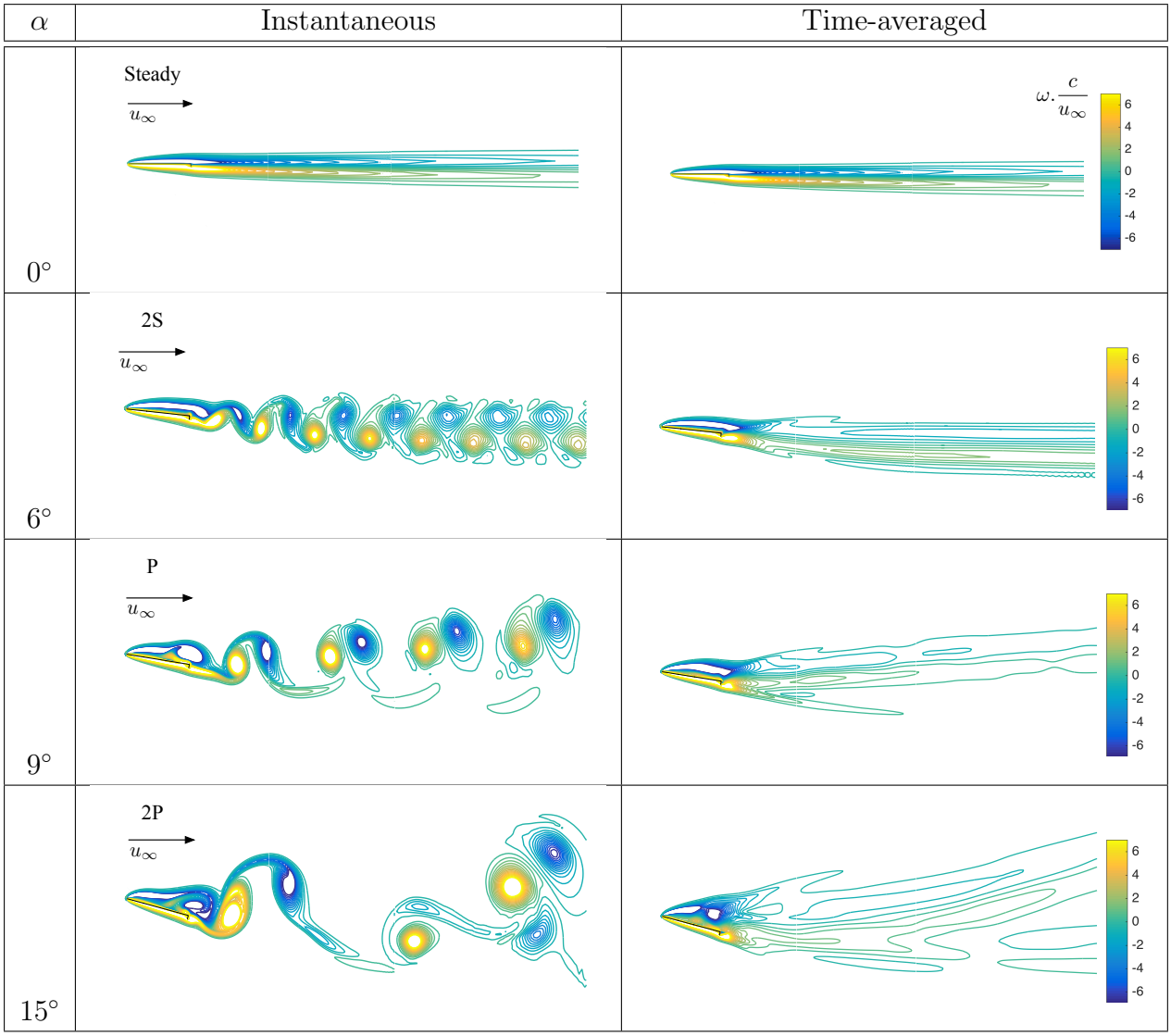

Figure B.2: Instantaneous and time-averaged two-dimensional vorticity fields $\omega c/u_\infty$, around NACA 0000 with a Gurney flap of $h/c = 0.06$ at various α. The contour plots represent the four characteristic regimes: steady, 2S, P and 2P.

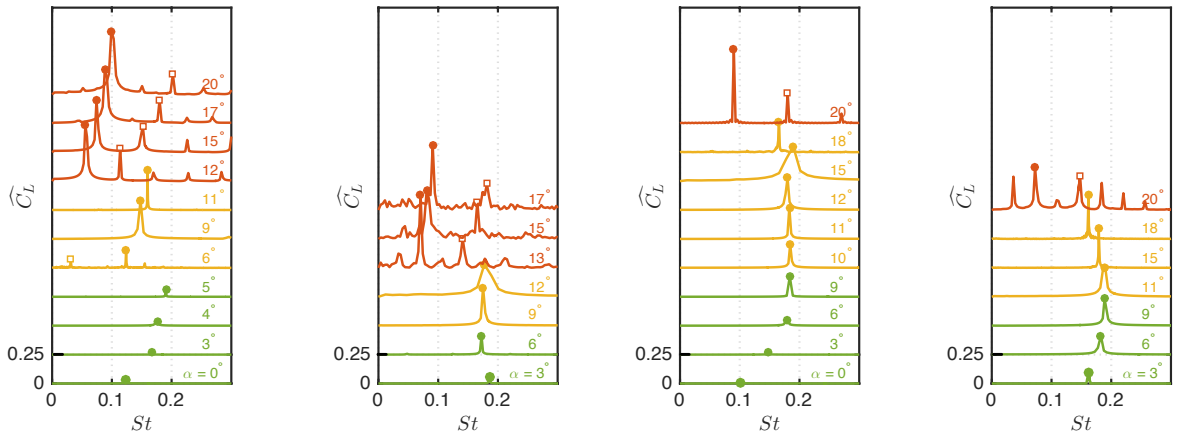

(a) NACA 0000, $h/c = 0.10$ (b) NACA 0006, $h/c = 0.15$ (c) NACA 0012, $h/c = 0.10$ (d) NACA 0018, $h/c = 0.15$

Figure B.3: Frequency spectra for a range of α for NACA 0000, 0006, 0012, and 0018 airfoils with Gurney flap. Dominant vortex shedding frequency - ●, harmonic vortex shedding frequency - □. Regions with dominant $St \in [0.12, 0.18]$ are classified as 2S and P regimes by the green and yellow regions respectively, and $St \in [0.06, 0.10]$ as 2P regime by the red region.

by Williamson and Roshko. These 2S, P and 2P modes are previously observed in studies involving oscillating cylinder [109, 136, 19] as well as airfoils [74, 68, 77, 78]. In particular, the wake modes have also been observed for the baseline case of NACA 0012 airfoil at $Re = 1000$ by Kurtulus [77, 78].

In the steady regime (figure B.2, $\alpha = 0°$), the wake is steady and the flow is attached to the airfoil surface. This flow regime attributes to the lowest magnitude of drag experienced by the airfoil compared to that in the other unsteady modes. With increase in α or h/c values, the flow starts to become unsteady. With this, the wake is classified into the next regime, the 2S mode.

The 2S mode (figure B.2, $\alpha = 6°$) is characterized by unsteady flow with periodic von Kármán vortex shedding of alternating clockwise and counter-clockwise rotating vortices (2S represents two single vortices). The time-averaged vorticity contour lines are below the center of the wake. The wake height, observable from the time-averaged vorticity fields, is larger compared to that of the steady regime denoting increase in drag experienced by the airfoil. The smaller wake height for the 2S regime compared to the other unsteady regimes is also

noticed. Also, a single peak in the frequency spectra, corresponding to the vortex shedding phenomena, for the cases classified into the 2S regime can be observed in figure B.3. The St values corresponding to the dominant vortex shedding frequency lie between $[0.12, 0.18]$ with increase in angle of attack through this regime. With further increase in α and h/c values, the wake transitions to the next regime, the P mode.

The P mode (figure B.2, $\alpha = 9°$) is distinguished by periodic von Kármán shedding of a single vortex pair (P represents a single vortex pair). The spatial separation between two vortex pairs is distinctly larger compared to that observed between the single vortices in the 2S mode. The time-averaged vorticity contour lines of the regime shifts above the center of the wake, portraying decrease in lift experienced by the airfoil. Height of the wake increases considerably compared to the 2S regime. This increases the drag force experienced by the airfoil. Similar to the 2S regime, the cases classified in the P regime are characterized by the occurrence of single peaks in the frequency spectra as seen from figure B.3. The St corresponding to these dominant vortex shedding frequency saturates to values in $[0.12, 0.18]$ for this regime. Further increase in α and h/c values causes the wake transition to the complex 2P mode.

The 2P mode (figure B.2, $\alpha = 15°$) is characterized by two pairs of vortices convecting above and below the center of the wake (2P represents two vortex pairs). The time-averaged vorticity field for the 2P regime evidently depicts the vortex pairs convecting away from the center of the wake. Compared to all other regimes, the 2P wake is most prominent and has the largest height amongst the four wake regimes. Consequently, the drag force experienced by the airfoils for this regime is the highest compared to that of all the other modes. Moreover, the downward force acting on the airfoil due to the upward displacement of the mean flow reduces the lift enhancement. The frequency spectra for cases classified in the 2P regime exhibits two prominent peaks, portraying the shedding of the two pairs of vortices. Also, the St values corresponding to the dominant vortex shedding frequency drop sharply from $[0.12, 0.18]$ and saturates at values $St \in [0.06, 0.1]$. These observations from the frequency spectra of lift compared to that of the 2S and P modes signify the occurrence of the 2P mode. The occurrence of the 2P mode is found in baseline cases (without Gurney

flap) for NACA 0012 at $Re = 1000$ by Kurtulus [77, 78], but only at very high angles of attack, $\alpha \in [23°, 41°]$. By adding the Gurney flap, emergence of the 2P regime is seen for lower α. This 2P mode may be a predominantly two-dimensional phenomenon and may be suppressed by spanwise (three-dimensional) instabilities. We provide discussions on the influence of three-dimensionality on the 2P wake in Section B.3. Thus, the emergence of the 2P mode should be used as a cautionary guide for the need of three-dimensional simulations to further analyze the flow. In fact, one should avoid operating an airfoil in such 2P regime in most cases, due to the large-scale unsteadiness. Nonetheless, we provide discussions on the wake dynamics and aerodynamic characteristics of the 2P mode in Sections B.2 and B.2 to paint a complete description of the four wake regimes observed in two-dimensional flows.

We use the examination of the flow structure of the wake and the lift spectra to summarize the wake regimes of all four airfoils using a wake classification diagram on the $(\alpha, h/c)$ plane. Figure B.4 provides an overview of the simulations performed and the influence of the Gurney flap on the wake modes for different airfoils. The baseline cases without flap are plotted on the x-axis. Representative vorticity fields of different wake regimes observed are also portrayed for each airfoil case. With the addition of the Gurney flap, transition of the unsteady wake modes is shifted to lower angles of attack. The protruding flap disrupts the inflow, causing the flow to be unsteady at lower angles of attack. The wake classification diagram shifts towards the left axis of the $(\alpha, h/c)$ plane with increase in the Gurney flap height.

When the airfoil geometry is changed from flat plate to a thick airfoil, the occurrence of the 2P regime is delayed to higher h/c and α values. Furthermore, the size of the steady regime decreases. Increasing the thickness of the airfoil leads to a decrease in the influence of the Gurney flap as the thickness of the airfoil overshadows the effect of the flap. As a result of this, the complex 2P mode is revealed only at higher α and h/c values for thicker airfoils.

The wake classification diagram provides a broad picture of the effect of adding Gurney flap to the trailing edge of the airfoil. The diagram is useful to determine the nature of flow at different h/c and α values for all the airfoils studied. The overall performance of different airfoil-Gurney flap configurations can be understood from the diagram. This can

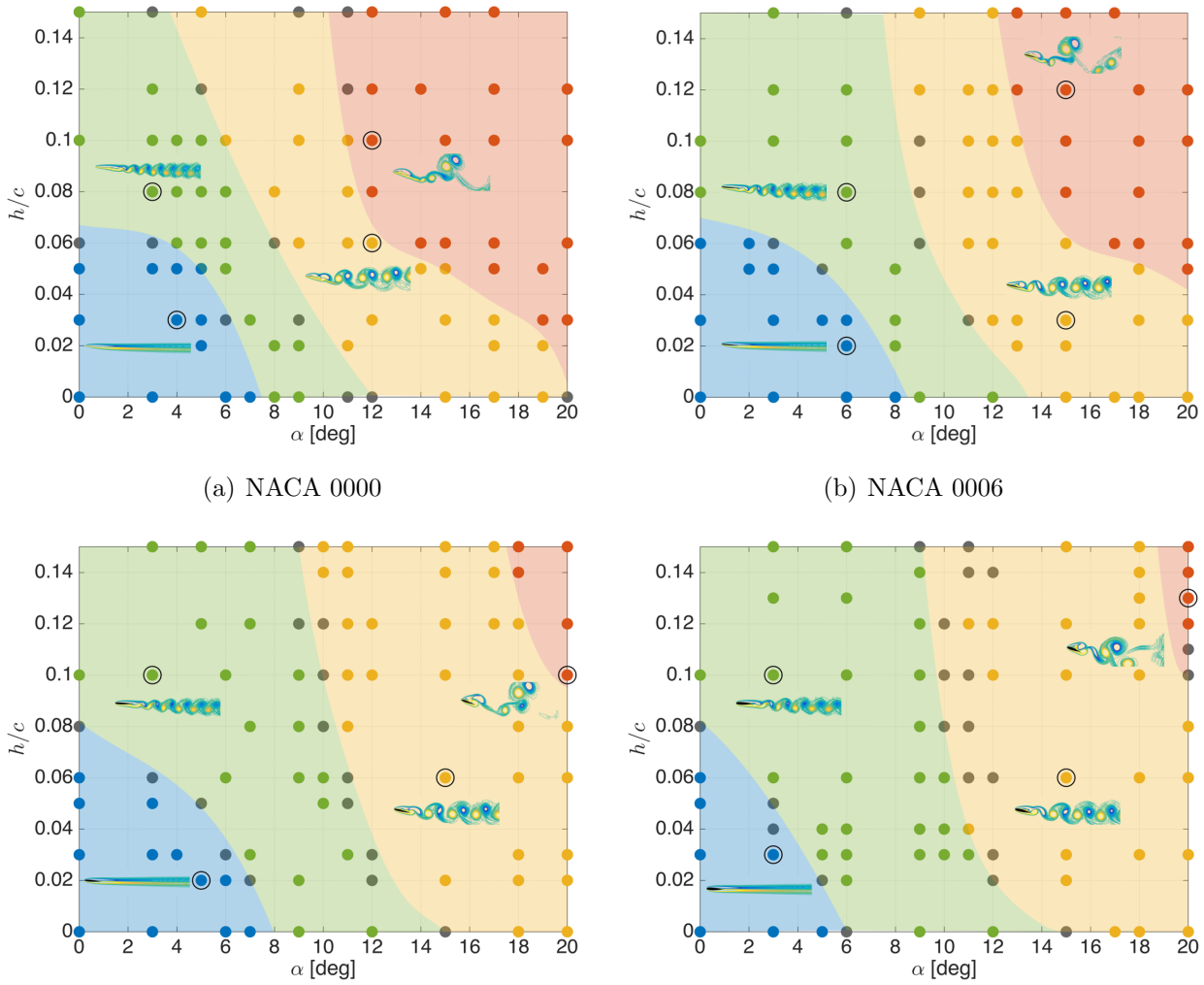

(a) NACA 0000

(b) NACA 0006

(c) NACA 0012

(d) NACA 0018

Figure B.4: Wake classification diagram for NACA 0000, 0006, 0012, and 0018 airfoils are illustrated. All cases simulated in the current study are categorized into different characteristic wake regimes respect to h/c and α values. Different regimes are described by: steady - blue, 2S - green, P - yellow, 2P - red and transition between two regimes - gray. The boundaries for all the regimes are obtained by polynomial curve fitting.

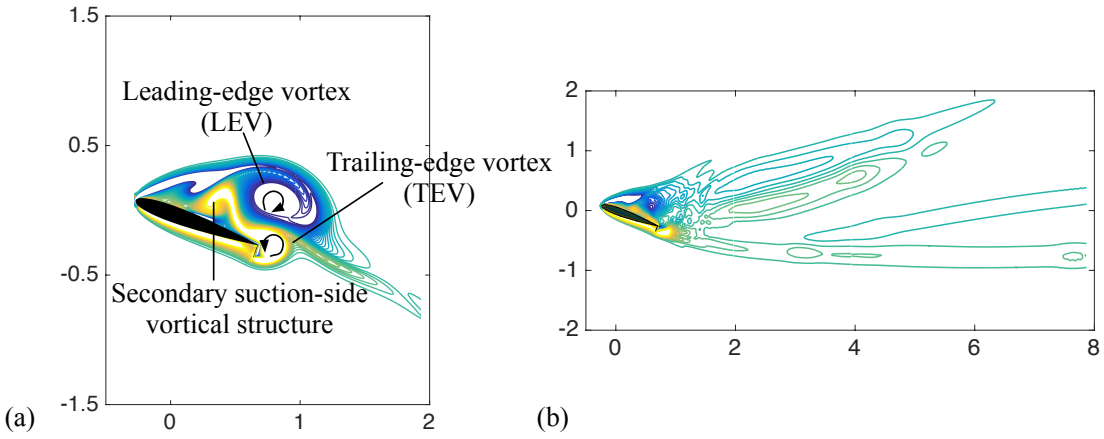

Figure B.5: Near-wake vortices for NACA 0012 with a Gurney flap of $h/c = 0.1$ at $\alpha = 20°$ (2P wake regime): (a) instantaneous vorticity field with (1) leading-edge vortex (LEV), (2) trailing-edge vortex (TEV) and (3) secondary suction-side vortical structure, (b) time-averaged vorticity field.

be used to determine the optimal geometric and angle of attack conditions for different aerodynamic performance requirements. Depending on the necessity, the ideal airfoil and corresponding Gurney flap configuration can be chosen. In Section B.3, we present insights from companion three-dimensional simulations and the influence of three-dimensionality on the wake dynamics.

Near-wake dynamics

Next, let us analyze the wake dynamics influencing the wake mode transitions, which is responsible for the unsteady aerodynamic forces experienced by the airfoils. We in particular focus on the difference in shear-layer roll-up and near-wake vortical structures that lead to the formation of vortices further downstream. Mainly three regions are examined in detail: suction and pressure sides of the airfoil, and vicinity of the Gurney flap. We depict the canonical near-field wake vortical structures analyzed herein in figure B.5.

The main vortical structures observed at the near wake of the airfoil at different angles of attack and Gurney flap heights comprise of the main clockwise rotating leading-edge vortex (LEV) on the suction side and the main counter-clockwise rotating trailing-edge vortex

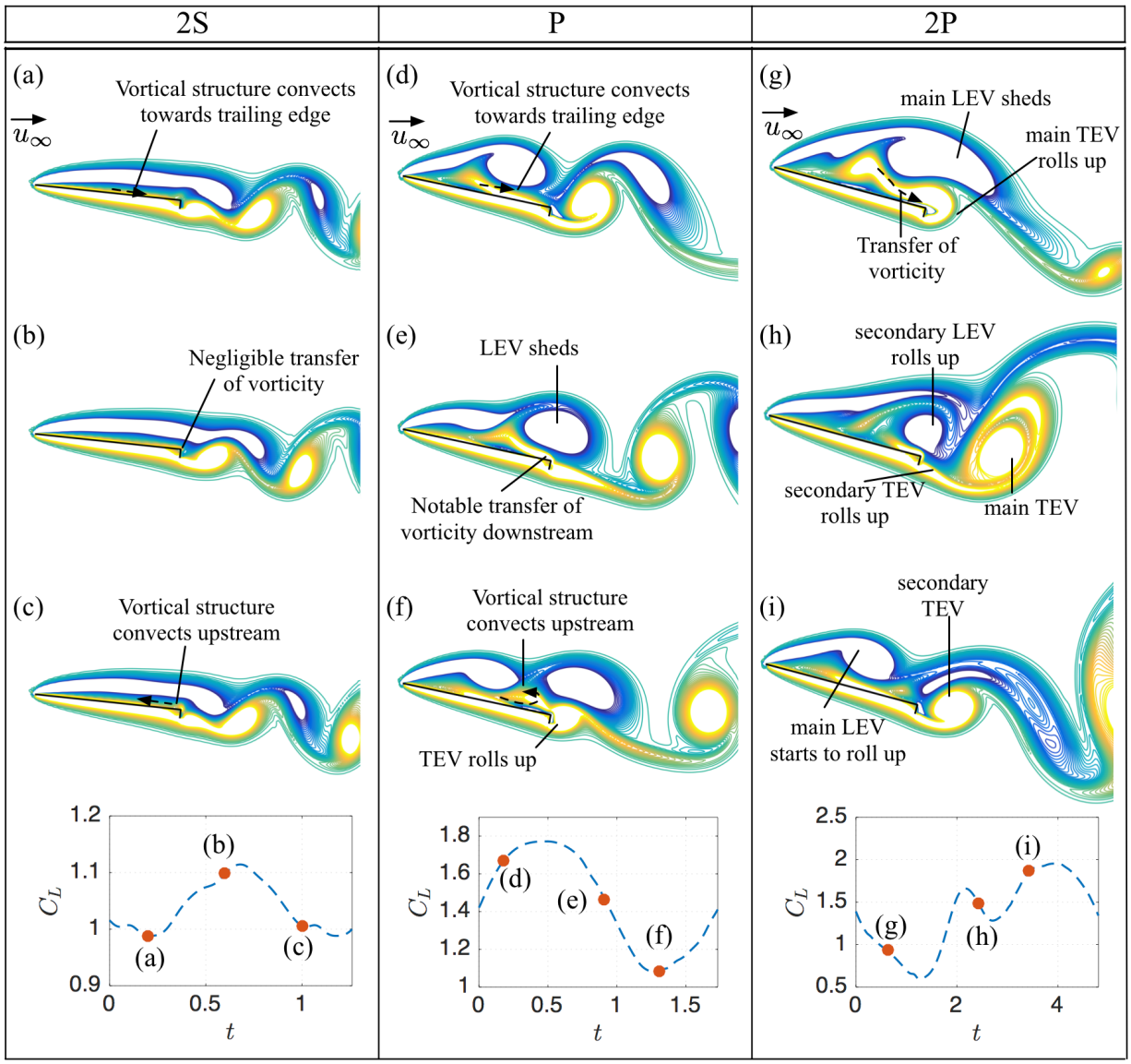

Figure B.6: Illustration of near field flow of three cases classified under the (a) - (c) 2S, (d) - (f) P, and (g) - (i) 2P regimes. The figure depicts instantaneous vorticity contour plots of flow over NACA 0000 airfoil at $\alpha = 6°, 12°$ and $15°$ with a Gurney flap of $h/c = 0.06$. Corresponding instantaneous lift data, represented by the ●, is also displayed on the bottom.

(TEV) on the pressure side, visualized in figure B.5(a). Secondary LEV and TEV also shed from the airfoil at high angles of attack or with a large Gurney flap (in the 2P regime). Apart from these vortical structures, the formation of the secondary suction-side vortical structure with positive vorticity between the leading-edge separation and suction-side wall, as shown in figure B.5(a), is observed to be important for the wake dynamics. The formation of this secondary structure is a result of the roll-up of the large LEV caused by the separated flow. The formation and behavior of the structures vary with transition of the wake regime.

Let us present a brief summary of the near-wake dynamics, followed by specific details for each wake mode. The formation and periodic shedding of LEV and TEV are expected at moderate angles of attack for flow past an airfoil. Once a sufficiently strong LEV is formed, the secondary suction-side vortical structure emerges on the suction surface. The increase of circulation of the secondary vortical structure with substantial increase of strength of the LEV is observed. Moreover, the strong influence of the LEV and the secondary vortical structure at higher α and h/c (in the 2P regime) causes the TEV to roll-up onto the suction side, eventually leading to transfer of vorticity from the secondary vortical structure to the TEV, as depicted in figure B.5(a). Note that the Gurney flap supports this merger by locally delaying the incoming flow as the TEV forms and merges with the secondary suction-side vortical structure. This phenomenon is observed only at very high angles of attack or with a substantially large Gurney flap, particularly in the 2P wake regime. The process results in a broader wake, leading to increase in drag. Moreover, the mean flow is displaced upward with respect to the center of the wake, which is evident for the 2P mode from the time-averaged vorticity field in figure B.5(b), decreasing the lift enhancement.

For the 2S regime, figure B.6 (a)-(c), we observe the roll-up and convection of a vortical structure with positive vorticity between the leading-edge separation and the suction-side wall, visible at the trailing edge in figure 5(c). We refer to this vortical structure as the secondary suction-side vortical structure for the 2S regime. The circulation of the secondary suction-side vortical structure is small and is not strong enough to influence the TEV. The LEV and TEV shed periodically as single vortices, and there is no upward shift of the flow above the center of the wake. These are the reasons for the high lift-to-drag ratios, $\overline{C_L/C_D}$,

observed for cases in the 2S wake mode, which are further described in section B.2.

As the flow transitions to the P regime, figure B.6 (d)-(f), the circulation of the near-wake vortical structures increase. The strengthened LEV and secondary suction-side vortical structure influences the TEV to roll up along the outer walls of the Gurney flap with considerable transfer of vorticity from the secondary structure to the TEV. The LEV and TEV shed periodically but a distinct vortex pair is formed compared to the individual vortices in the wake of the 2S regime. The wake width also increases and the flow shifts above the center of the wake. This leads to the increase in drag, decrease in lift enhancement and fall of the $\overline{C_L/C_D}$ curve, as further discussed in section B.2, for cases in the P regime.

In the 2P regime, figure B.6 (g)-(i), the circulation of the secondary suction-side vortical structure is sizable enough to influence the TEV to roll-up onto the suction side, and the vorticity from the secondary vortical structure is transferred to the TEV. The transfer and accumulation of positive vorticity on the suction-side causes the main LEV to shed, followed by the roll-up of the leading-edge shear layer to form the second LEV. The main TEV sheds after considerable build-up of circulation due to the transfer of vorticity from the secondary vortical structure. This leads to roll-up of the second TEV on the pressure side. By the time the second LEV sheds from the trailing edge, the second TEV rolls-up along the outer walls of the Gurney flap. The influence from the secondary vortical structure is not strong enough for the roll-up of the second TEV onto the suction side. The second LEV convects downward pairing up with the secondary TEV about $10c$ downstream. The wake width is increased considerably compared to the other unsteady regimes, with the flow shifting above and below the center of the wake. This wake dynamics lead to increase of drag, decrease of lift enhancement and degradation of the $\overline{C_L/C_D}$ curve, which are described in section B.2.

Aerodynamic forces

Next, we examine the effects of the wake modifications on the aerodynamic forces from the use of Gurney flaps. The main objective of attaching a Gurney flap to the trailing edge of an airfoil is to enhance the lift force experienced by the airfoil. Current results show that

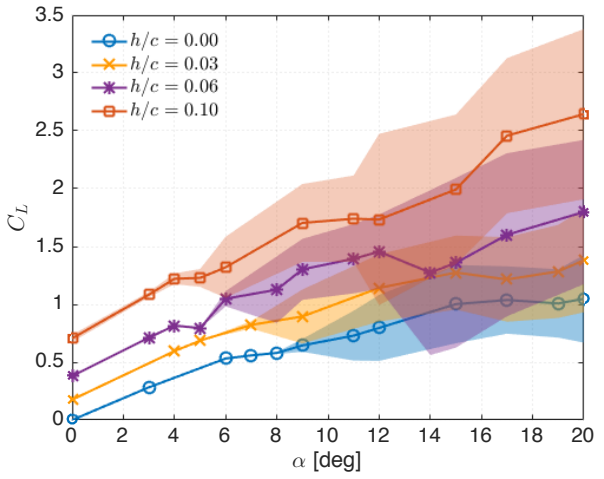

(a) NACA 0000

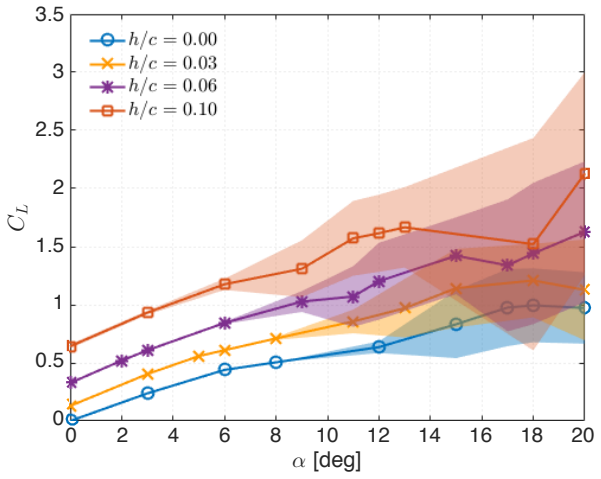

(b) NACA 0006

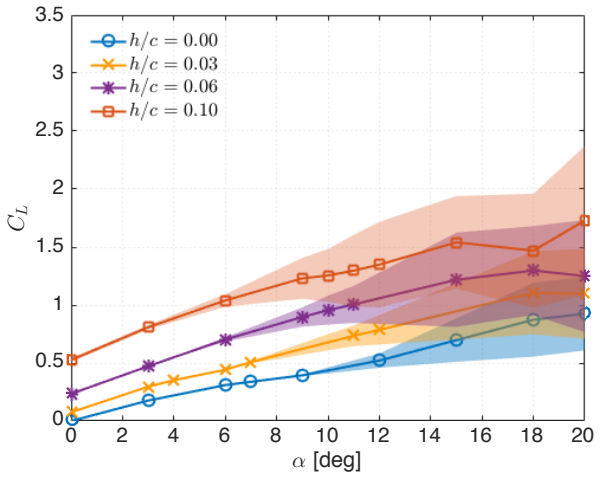

(c) NACA 0012

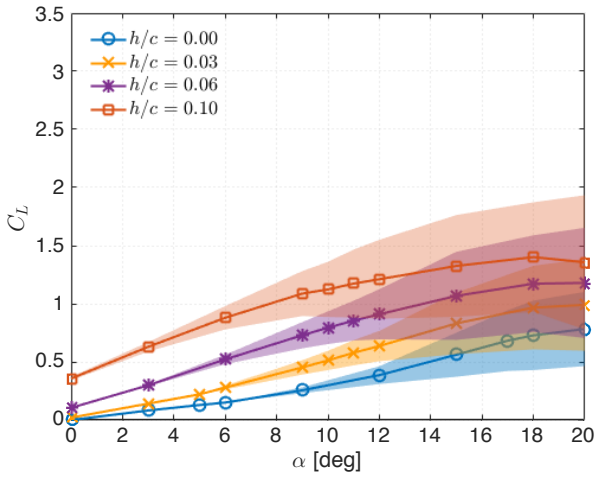

(d) NACA 0018

Figure B.7: Lift coefficient C_L over angle of attack α for NACA 0000, 0006, 0012 and 0018 airfoils with select Gurney flap heights. The time-averaged $\overline{C_L}$ values are represented by the solid lines and fluctuations in C_L are represented by the shaded region for each configuration.

at a low Reynolds number of $Re = 1000$, the Gurney flap is able to generate high levels of lift forces. It is also seen that as the height of the flap is increased, lift also increases. The lift coefficient, C_L, of representative cases for each airfoil is shown in figure B.7, where the time-averaged values, $\overline{C_L}$, are depicted by the solid lines and the fluctuations in the forces are represented by the shaded regions. The blue lines for $h/c = 0.00$ cases depict the baseline results without a Gurney flap for all the airfoils.

As discussed above, $\overline{C_L}$ increases with α and h/c values for all airfoils. Lift force enhancement of more than twice the baseline values is achieved using Gurney flap, particularly at $h/c = 0.10$ for all airfoils in almost all cases. Due to the presence of the Gurney flap, effective camber of the airfoil increases, attributing to lift enhancement. Fluctuations in the lift forces appear when the flow transitions from steady to unsteady state (2S regime). For a given angle of attack, $\overline{C_L}$ as well as the fluctuations of C_L are amplified with increase in Gurney flap height.

At higher angles of attack, sudden jumps or bursts in C_L fluctuations are observed for all the cases. The fluctuations in C_L exhibits trends of sudden increase in magnitude with increase in α, suggesting a transition from one flow regime to another with different Gurney flap heights and angles of attack. The transitions correspond to the wake mode shift from the 2S mode to the P mode, and then to the 2P mode. Thus, the airfoil experiences the highest magnitude of $\overline{C_L}$ as well as the fluctuations of C_L when the wake is classified under the 2P mode. Again, the transition of the wake from the steady regime through the 2P regime can be evidently observed by the jagged growth of C_L fluctuations with α for the NACA 0000 airfoil. The transition of the wake from the P to the 2P mode is clearly observed for the NACA 0006 and 0012 cases at high angles of attack.

The benefit of lift enhancement is however accompanied with a penalty of some drag increase. The drag coefficients, C_D, of representative cases for each airfoil are shown in figure B.8. As it can be observed, $\overline{C_D}$ increases with α and h/c values. The $\overline{C_D}$ for all cases have low values at lower angles of attack. The appearance of fluctuations in C_D in conjunction with the wake transition from the steady regime to the 2S regime is also observed at lower α, but the magnitudes of the fluctuations are small. Also, the sudden and jagged

variations in the fluctuations of C_D with increase in α are small compared to that observed for the C_L fluctuations. The fluctuations in C_D increase suddenly at high angles of attack when the wake transition from the P mode to the 2P mode, also observed above for lift, for all airfoils.

The thickness of the airfoil plays a major role on the aerodynamic forces experienced by the airfoil. With increase in airfoil thickness, the effect of the Gurney flap is overshadowed. As a result, different trends are observed for lift and drag on the airfoils. For the range of angles of attack considered in this study, the magnitudes of $\overline{C_L}$ and fluctuations in C_L decreases for thicker airfoils. Whereas, the drag force increases with airfoil thickness at low angles of attack, which is expected for the baseline cases, but the trend reverses at higher angles of attack and drag generated decreases for thicker airfoils compared to thinner airfoils. Another behavior observed are for the lift and drag slopes. The lift slope, $a = \mathrm{d}\overline{C_L}/\,\mathrm{d}\alpha$ follow a jagged trend for thinner airfoils, whereas the slope is smoother for thicker airfoils. The same is observed for the drag slope, although the fluctuations of the drag slope for thinner airfoils are small compared to that of lift slope. All the above observations further emphasizes the reduced influence from the Gurney flap due to the overshadowing effect of the airfoil thickness.

Lift-to-drag ratio, $\overline{C_L/C_D}$, for all airfoils is examined and depicted in figure B.9. With increase in α, $\overline{C_L/C_D}$ increases drastically, reaching its maximum value, and then decreases gradually. Significant enhancement of $\overline{C_L/C_D}$ is achieved with the utilization of a Gurney flap. The $\overline{C_L/C_D}$ at lower angles of attack, in the range of $\alpha \in [0^\circ, 12^\circ]$, is observed to be higher compared to baseline cases in general for all airfoils and flap heights. This range of α is smaller for thinner airfoils (NACA 0000 and 0006) although the peak value of $\overline{C_L/C_D}$ is higher compared to thicker airfoils (NACA 0012 and 0018). This range of α corresponds to the steady and 2S regime for all the airfoils, where the drag remains low. At higher range of α, $\overline{C_L/C_D}$ decreases and reach values close to the baseline values for the controlled cases of all airfoils. These range of α corresponds to the P and 2P regimes of the respective airfoils where the highest magnitude of drag is experienced by the airfoils. The $\overline{C_L/C_D}$ curves degrade below the baseline cases for NACA 0000 and 0006 at higher α.

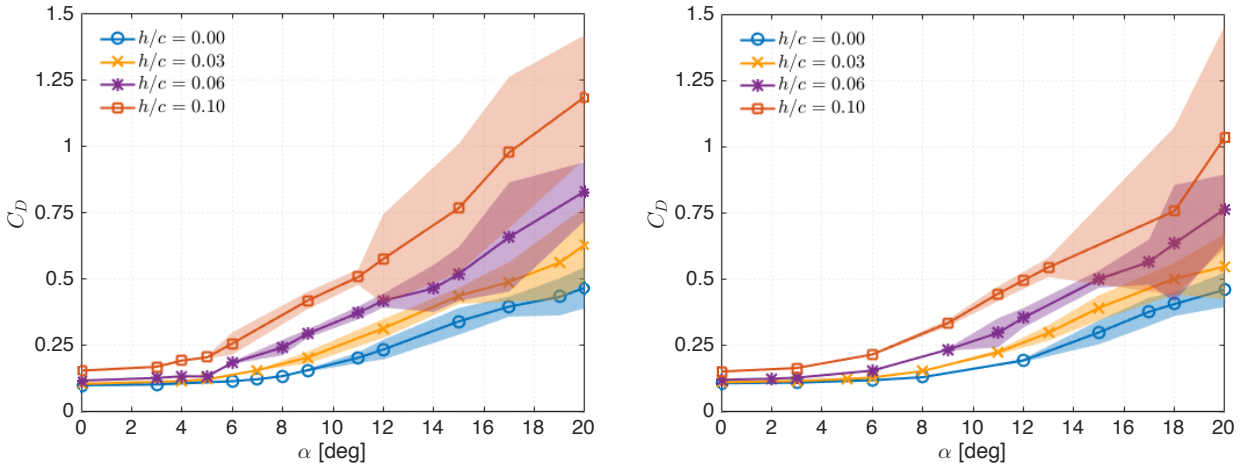

(a) NACA 0000

(b) NACA 0006

(c) NACA 0012

(d) NACA 0018

Figure B.8: Drag coefficient C_D over angle of attack α for NACA 0000, 0006, 0012 and 0018 airfoils with select Gurney flap heights. The time-averaged $\overline{C_D}$ values are represented by the solid lines and fluctuations in C_D are represented by the shaded region for each configuration.

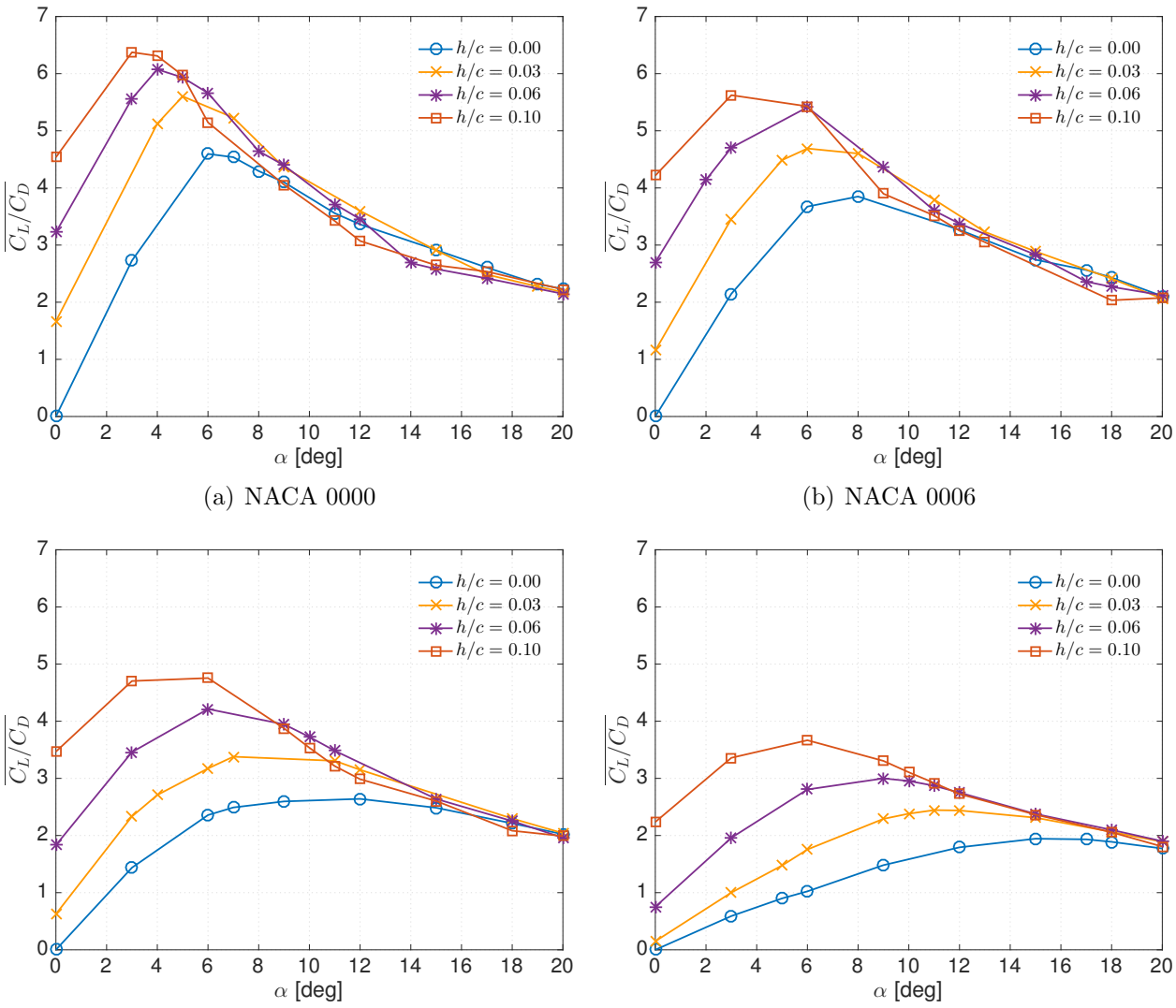

(a) NACA 0000

(b) NACA 0006

(c) NACA 0012

(d) NACA 0018

Figure B.9: Lift-to-drag ratio $\overline{C_L/C_D}$ over angle of attack α for NACA 0000, 0006, 0012 and 0018 airfoils with Gurney flap.

All the above observations show that an airfoil with a large Gurney flap at high angles of attack experiences large forces. With increase in α, thinner airfoils (NACA 0000 and 0006) experience the highest increase in lift and drag, whereas thicker airfoils (NACA 0012 and 0018) attributes with smoother lift and drag slopes. The enhanced lift-to-drag ratio brought about by the Gurney flap is maintained over a wider range of α and h/c values in thicker airfoils, while thinner airfoils experience higher magnitude of $\overline{C_L/C_D}$ over a narrower range of α. Thus, for high levels of lift generation and $\overline{C_L/C_D}$ requirements, thinner airfoils can be suitable amongst the considered airfoils. In contrast, to obtain the enhanced $\overline{C_L/C_D}$ over a wider range of angles of attack and lower drag when Gurney flap is attached, thicker airfoils perform well, although with a relatively lower magnitude of $\overline{C_L/C_D}$.

B.3 Analysis of three-dimensional flows

Three-dimensional analysis is performed on the flow around the NACA 0006 airfoil with Gurney flap of $h/c = 0.08$ at $\alpha = 6°, 12°$ and $18°$ to examine the spanwise effects on the wakes. The chosen angles of attack yield the 2S, P and 2P wake regimes, respectively, for two-dimensional flow as shown in figure B.4(b). The three-dimensional flow fields and the resulting force characteristics are summarized in figure B.10. We utilize the iso-surface of Q-criterion [57] to visualize the three-dimensional airfoil wake. The aerodynamic force characteristics of the three-dimensional flow are also compared to those obtained from the two-dimensional analysis.

The cases with $\alpha = 6°$ and $12°$, classified as the 2S and P wakes, respectively, in two-dimensional flow, remains two-dimensional with spanwise extension of the airfoil. Although the $12°$ case shows some spanwise variations in the flow, it can be considered as nominally two-dimensional. The instantaneous snapshots of the two cases show the presence of the alternating positive and negative vortices leading to the formation of the Kármán vortex street, previously observed in the two-dimensional analysis. The time-averaged flow field also corresponds to that observed for a Kármán wake, and previously observed in the two-dimensional

analysis. These observations suggest that the dominant vortex shedding frequency, lift and drag forces, and the lift-to-drag ratio experienced by the airfoil are similar to those observed in the two-dimensional analysis. This is noted from the similarity in the aerodynamic force characteristics for the two-dimensional and three-dimensional results in figure B.10, further highlighting the two-dimensional nature of the flow. The same criteria used in the two-dimensional analysis are applied to classify the $\alpha = 6^\circ$ and 12° cases under the 2S and P wake regimes.

The case with $\alpha = 18^\circ$, classified under the 2P regime for two-dimensional flow, is influenced by the spanwise instabilities in the flow and results in a fully three-dimensional flow with an underlying Kármán wake. The formation of the 2P wake mode is not observed. The 2P wake structure is disrupted by the spanwise instabilities and the wake structure is suppressed to a Kármán vortex street with spanwise variations. As seen from the top-view of figure B.10, the cores of the positive and negative vortices in the Kármán street also show spanwise variations. The time-averaged flow field depicts the reduction in the wake thickness considerably compared to that observed in the two-dimensional 2P wake structure (see figure B.2). This reflects in considerable reduction in the drag force experienced by the airfoil compared to that for the two-dimensional 2P regime. The altered dynamics of the shear layer roll-up leads to a reduction in the lift force compared to the two-dimensional 2P case. These inferences are observed from the aerodynamic force characteristics of the $\alpha = 18^\circ$ case in figure B.10. The considerable decrease in the drag force compensates for the reduction in the lift enhancement experienced by the airfoil to maintain the lift-to-drag ratio. The dominant shedding frequency of $St = 0.155$, similar to the values observed for that of the 2S and P wake structures, substantiates the Kármán wake behavior for the dominant vortical structures of the three-dimensional flow field.

We have observed that the two-dimensional analysis provides a foundation to understand the occurrence of the 2S and P wake regimes for the three-dimensional spanwise-periodic setup. The deviation with three-dimensional flow appears for the fully three-dimensional flow for what would be the 2P wake regime in the two-dimensional setting. Nonetheless, it should be noted that at higher Re, three-dimensionality of the wake structures can be

instigated to even the flow classified as two-dimensional wake regimes at this Re. This transition of the flow field of each particular wake regime from two-dimensional to three-dimensional is beyond the scope of the current work, and the readers are referred to studies which focus in such analyses [36, 18, 56]. Further analyses have to be performed to completely understand these effects for the current problem. The novelty of the current work is in understanding the transition of the wake regimes from steady through 2P or Kármán vortex street having spanwise variations with change in different parameters of airfoil thickness, angle of attack, effects of the Gurney flap and the flap height, and associated effects on the force characteristics of the airfoil in an incompressible flow at $Re = 1000$.

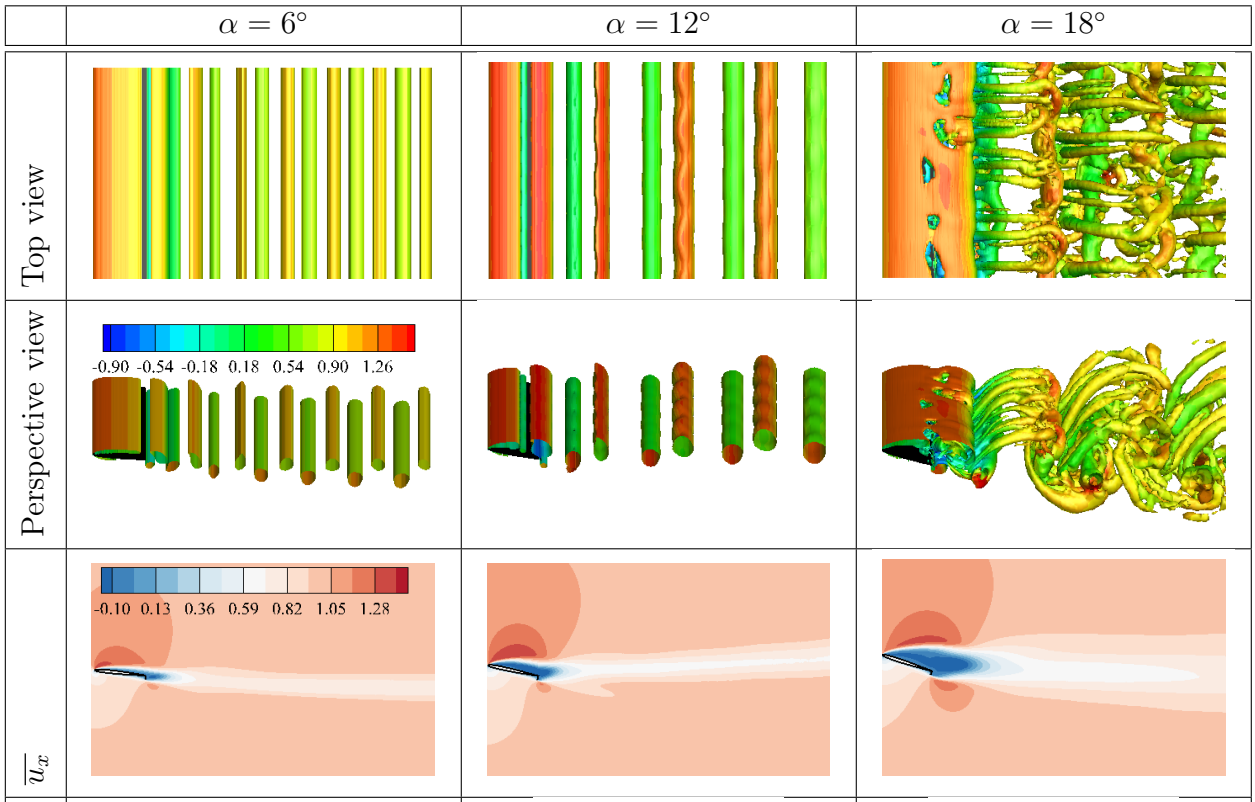

	2D	3D
$\overline{C_L}$	1.01	1.03
$\overline{C_D}$	0.18	0.19
$\overline{C_L/C_D}$	5.54	5.51
St	0.18	0.19

	2D	3D
$\overline{C_L}$	1.41	1.49
$\overline{C_D}$	0.42	0.44
$\overline{C_L/C_D}$	3.35	3.37
St	0.16	0.16

	2D	3D
$\overline{C_L}$	1.76	1.19
$\overline{C_D}$	0.77	0.51
$\overline{C_L/C_D}$	2.32	2.33
St	0.08	0.15

Figure B.10: Flow visualization and aerodynamic force characteristics of flow over the NACA 0006 airfoil with Gurney flap of $h/c = 0.08$ at $\alpha = 6°, 12°$ and $18°$ with three-dimensional DNS. Each row consists of the top and perspective views of instantaneous snapshots of Q-criterion isosurface colored with u_x, the time-averaged $\overline{u_x}$ and the comparison of aerodynamic force characteristics between the respective cases of two-dimensional and three-dimensional analysis.

APPENDIX C

Reynolds number and dimension reduction independence of network measures

We assess the effect of Reynolds number on the network representation of vortical interactions in isotropic turbulence by evaluating the node strength distribution for three- and two-dimensional flow fields with various Re_λ, as shown in figures C.1 (a) and (b), respectively. The strength distributions of flows with different Reynolds numbers collapse to a single curve with the use of appropriate non-dimensionalization for the edge weights. The results suggest that the network formulation is able to capture the key characteristics of the universal scaling of isotropic turbulence. The fine resolution of spatial discretization required to simulate turbulent flows also pose a challenge to analyze the interactions amongst the vortical elements. We subsample the flow field to reduce the dimension of the flow field being analyzed.

The effect of sub-sampling the turbulent flow field on the network measures is evaluated by comparing the node strength distribution of various low resolution flow fields. A three-dimensional flow field of $Re_\lambda = 40$ with a grid resolution of $256 \times 256 \times 256$ is used. We sub-sample the data to various smaller grid resolutions and compute the node strengths, as shown in figure C.1 (c). The node strength computed based on the non-dimensionalized edge weight allows scaling of the distributions. The node strength distributions collapse into a single distribution and converge with higher grid resolution. The $k_{\max}$ for each low-resolution grid used in the node strength distribution computation is depicted in the energy spectra in figure C.1 (d). The grid resolution using a $64 \times 64 \times 64$ grid satisfies the $k_{\max}\eta \geq 1$ condition. Similar observations are also made for two-dimensional isotropic turbulence, as depicted in figure C.1 (e). The results also demonstrate the application of network-based formulation

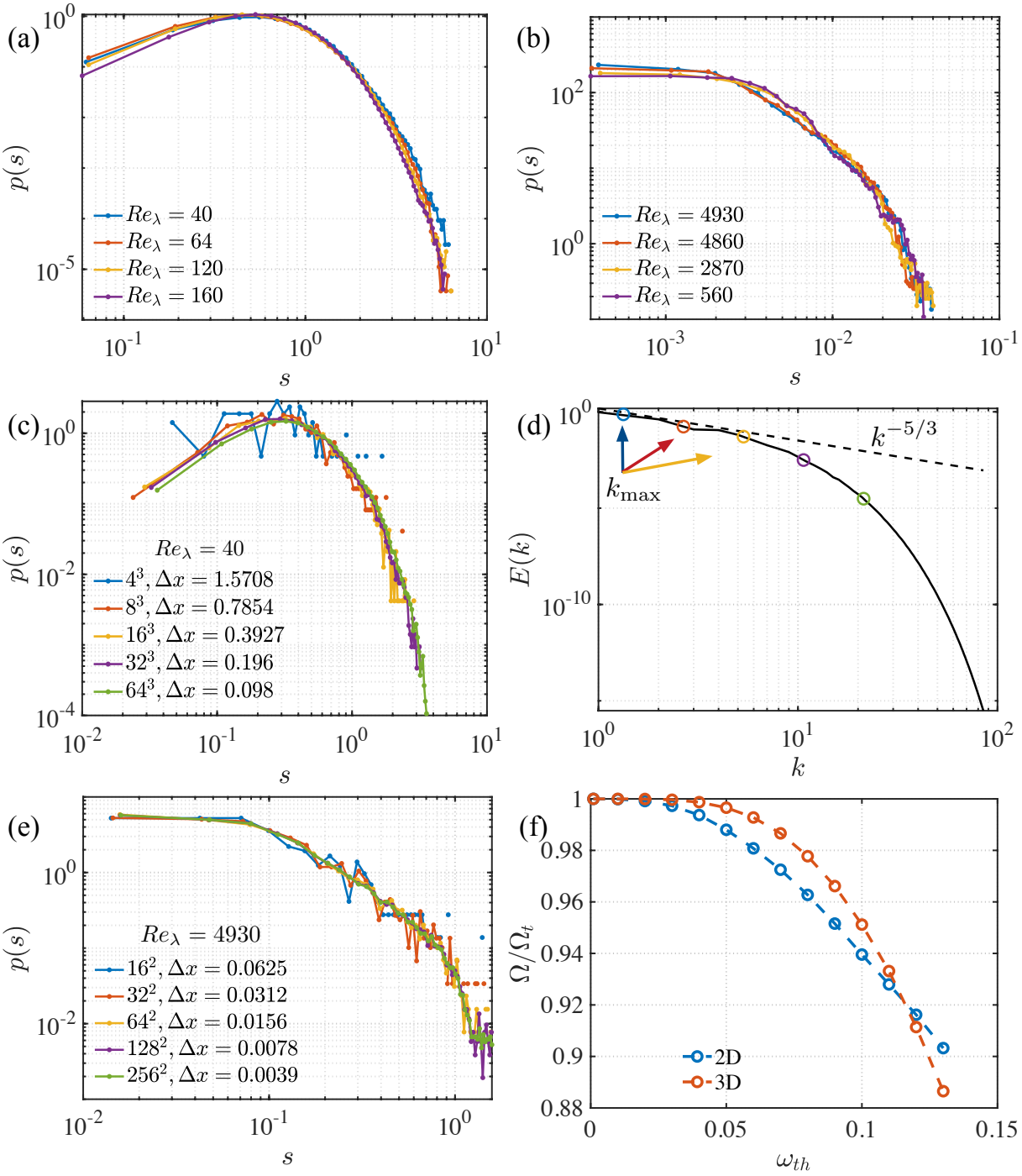

Figure C.1: Collapse of node strength distribution with increase in Reynolds number for (a) three- and (b) two-dimensional isotropic turbulence. (c) Convergence of node strength distribution over sampling rate in three-dimensional turbulence of $Re_\lambda = 40$. (d) Maximum resolvable wave number for various grid resolution or sampling rate. (e) Convergence of node strength distribution over sampling rate in two-dimensional turbulence of $Re_\lambda = 4930$. (f) Variation of enstrophy with vorticity threshold in two- and three-dimensional turbulence.

from a discrete to continuous description of the flow field.

We only analyze vortical elements in the flow field with high vorticity, extracted through vorticity threshold. The choice of the vorticity threshold of $\omega_{th} = 0.05||\boldsymbol{\omega}(\mathbf{r})||_\infty$ is given by analyzing the effect of thresholding on the total enstrophy of the flow field, as shown in figure C.1 (f). For both two- and three-dimensional turbulence, $\omega_{th} = 0.05||\boldsymbol{\omega}(\mathbf{r})||_\infty$ results in retaining more than 98% of the enstrophy of the original flow field. This is similar to the values used to analyze structures of high vorticity [67, 88], capturing the influential regions of the flow.

REFERENCES

[1] R. Albert, I. Albert, and G. L. Nakarado. Structural vulnerability of the north american power grid. *Physical Review E*, 69(2):025103, 2004.

[2] R. Albert, H. Jeong, and A.-L. Barabási. Error and attack tolerance of complex networks. *Nature*, 406:378–382, July 2000.

[3] J. D. Anderson Jr. *Fundamentals of aerodynamics*. McGraw-Hill, 2010.

[4] H. Aref. Stirring by chaotic advection. *Journal of Fluid Mechanics*, 143:1–21, 1984.

[5] H. Aref. Point vortex dynamics: a classical mathematics playground. *Journal of Mathematical Physics*, 48(6):065401, 2007.

[6] D. Ayala and B. Protas. Extreme vortex states and the growth of enstrophy in three-dimensional incompressible flows. *Journal of Fluid Mechanics*, 818:772–806, 2017.

[7] Z. Bai, N. B. Erichson, M. Gopalakrishnan Meena, K. Taira, and S. L. Brunton. Randomized methods to characterize large-scale vortical flow networks. *PLOS One*, 14(11), 2019.

[8] L. Baker, A. Frankel, A. Mani, and F. Coletti. Coherent clusters of inertial particles in homogeneous turbulence. *Journal of Fluid Mechanics*, 833:364–398, 2017.

[9] A.-L. Barabási. *Network science*. Cambridge University Press, 2016.

[10] G. K. Batchelor. *An introduction to fluid dynamics*. Cambridge university press, 2000.

[11] D. M. Bates and D. G. Watts. *Nonlinear regression analysis and its applications*, volume 2. Wiley Online Library, 1988.

[12] R. Benzi, S. Patarnello, and P. Santangelo. On the statistical properties of two-dimensional decaying turbulence. *Europhysics Letters*, 3(7):811, 1987.

[13] S. Bhattacharjee, B. Scheelke, and T. R. Troutt. Modification of vortex interactions in a reattaching separated flow. *AIAA Journal*, 24(4):623–629, 1986.

[14] V. D. Blondel, J.-L. Guillaume, R. Lambiotte, and E. Lefebvre. Fast unfolding of communities in large networks. *Journal of Statistical Mechanics: Theory and Experiment*, 2008(10):P10008, 2008.

[15] S. Boccaletti, V. Latora, Y. Moreno, M. Chavez, and D.-U. Hwang. Complex networks: Structure and dynamics. *Physics Reports*, 424(4):175–308, 2006.

[16] B. Bollobás. *Modern graph theory*. Springer, 1998.

[17] E. M. Bollt. Combinatorial control of global dynamics in a chaotic differential equation. *International Journal of Bifurcation and Chaos*, 11(08):2145–2162, 2001.

[18] M. Braza, D. Faghani, and H. Persillon. Successive stages and the role of natural vortex dislocations in three-dimensional wake transition. *Journal of Fluid Mechanics*, 439:1–41, 2001.

[19] D. Brika and A. Laneville. Vortex-induced vibrations of a long flexible circular cylinder. *Journal of Fluid Mechanics*, 250:481–481, 1993.

[20] S. L. Brunton and B. R. Noack. Closed-loop turbulence control: progress and challenges. *Applied Mechanics Reviews*, 67(5):050801, 2015.

[21] S. L. Brunton, J. L. Proctor, and J. N. Kutz. Discovering governing equations from data by sparse identification of nonlinear dynamical systems. *Proceedings of the National Academy of Sciences*, 113(15):3932–3937, 2016.

[22] P. Chakraborty, S. Balachandar, and R. J. Adrian. On the relationships between local vortex identification schemes. *Journal of Fluid Mechanics*, 535:189–214, 2005.

[23] S. G. Chumakov. A priori study of subgrid-scale flux of a passive scalar in isotropic homogeneous turbulence. *Physical Review E*, 78(3):036313, 2008.

[24] A. Clauset, M. E. J. Newman, and C. Moore. Finding community structure in very large networks. *Physical Review E*, 70(6):066111, 2004.

[25] T. Colonius and K. Taira. A fast immersed boundary method using a nullspace approach and multi-domain far-field boundary conditions. *Computer Methods in Applied Mechanics and Engineering*, 197:2131–2146, 2008.

[26] A. N. Cookson, D. J. Doorly, and S. J. Sherwin. Efficiently generating mixing by combining differing small amplitude helical geometries. *Fluids*, 4(2):59, 2019.

[27] G. Coppola, S. J. Sherwin, and J. Peiró. Nonlinear particle tracking for high-order elements. *Journal of Computational Physics*, 172(1):356–386, 2001.

[28] R. De Smet and K. Marchal. Advantages and limitations of current network inference methods. *Nature Reviews Microbiology*, 8(10):717–729, 2010.

[29] D. A. Donzis, P. K. Yeung, and K. R. Sreenivasan. Dissipation and enstrophy in isotropic turbulence: resolution effects and scaling in direct numerical simulations. *Physics of Fluids*, 20(4):045108, 2008.

[30] S. N. Dorogovtsev and J. Mendes. *Evolution of networks: From biological nets to the Internet and WWW*. Oxford University Press, 2013.

[31] Y. Dubief and F. Delcayre. On coherent-vortex identification in turbulence. *Journal of Turbulence*, 1(1):011–011, 2000.

[32] M. F. Eggl and P. J. Schmid. A gradient-based framework for maximizing mixing in binary fluids. *Journal of Computational Physics*, 368:131–153, 2018.

[33] C. Foias and R. Temam. Gevrey class regularity for the solutions of the Navier–Stokes equations. *Journal of Functional Analysis*, 87(2):359–369, 1989.

[34] S. Fortunato. Community detection in graphs. *Physics Reports*, 486(3):75–174, 2010.

[35] S. Fortunato and M. Barthélemy. Resolution limit in community detection. *Proceedings of the National Academy of Sciences*, 104(1):36–41, 2007.

[36] P. Freymuth. On transition in a separated laminar boundary layer. *Journal of Fluid Mechanics*, 25(4):683–704, 1966.

[37] V. Godavarthi, V. R. Unni, E. A. Gopalakrishnan, and R. I. Sujith. Recurrence networks to study dynamical transitions in a turbulent combustor. *Chaos: An Interdisciplinary Journal of Nonlinear Science*, 27(6):063113, 2017.

[38] M. Gopalakrishnan Meena, A. G. Nair, and K. Taira. Network community-based model reduction for vortical flows. *Physical Review E*, 97:063103, 2018.

[39] M. Gopalakrishnan Meena and K. Taira. Characterizing influential networked structures in isotropic turbulence. In *11th International Symposium on Turbulence and Shear Flow Phenomena, Southampton, UK*, 2019.

[40] M. Gopalakrishnan Meena and K. Taira. Identifying vortical network connectors for turbulent flow modification. *in review*, arXiv:2005.02514, 2020.

[41] M. Gopalakrishnan Meena, K. Taira, and K. Asai. Airfoil-wake modification with Gurney flap at low Reynolds number. *AIAA Journal*, 56(4):1348–1359, 2017.

[42] M. Gopalakrishnan Meena, K. Taira, and K. Asai. Low Reynolds number wake modification using a Gurney flap. In *AIAA paper 2017-0543*, 2017.

[43] L. Graftieaux, M. Michard, and N. Grosjean. Combining PIV, POD and vortex identification algorithms for the study of unsteady turbulent swirling flows. *Measurement Science and Technology*, 12(9):1422, 2001.

[44] R. Guimera and L. A. N. Amaral. Functional cartography of complex metabolic networks. *Nature*, 433(7028):895, 2005.

[45] R. Guimera, S. Mossa, A. Turtschi, and L. A. N. Amaral. The worldwide air transportation network: anomalous centrality, community structure, and cities' global roles. *Proceedings of the National Academy of Sciences*, 102(22):7794–7799, 2005.

[46] Ö. D. Gürcan. Nested polyhedra model of turbulence. *Physical Review E*, 95(6):063102, 2017.

[47] Ö. D. Gürcan. Nested polyhedra model of isotropic magnetohydrodynamic turbulence. *Physical Review E*, 97(6):063111, 2018.

[48] Ö. D. Gürcan, Y. Li, and P. Morel. Turbulence as a network of Fourier modes. *Mathematics*, 8(4):530, 2020.

[49] A. Hadjighasem, D. Karrasch, H. Teramoto, and G. Haller. Spectral-clustering approach to lagrangian vortex detection. *Physical Review E*, 93(6):063107, 2016.

[50] G. Haller. An objective definition of a vortex. *Journal of Fluid Mechanics*, 525:1–26, 2005.

[51] G. Haller. Lagrangian coherent structures. *Annual Review of Fluid Mechanics*, 47:137–162, 2015.

[52] F. Ham and G. Iaccarino. Energy conservation in collocated discretization schemes on unstructured meshes. *Annual Research Briefs*, 2004:3–14, 2004.

[53] F. Ham, K. Mattsson, and G. Iaccarino. Accurate and stable finite volume operators for unstructured flow solvers. *Annual Research Briefs*, pages 243–261, 2006.

[54] T. Hastie, R. Tibshirani, and J. Friedman. Overview of supervised learning. In *The elements of statistical learning*, pages 9–41. Springer, 2009.

[55] M. Hecker, S. Lambeck, S. Toepfer, E. Van Someren, and R. Guthke. Gene regulatory network inference: data integration in dynamic models—a review. *Biosystems*, 96(1):86–103, 2009.

[56] Y. Hoarau, M. Braza, Y. Ventikos, D. Faghani, and G. Tzabiras. Organized modes and the three-dimensional transition to turbulence in the incompressible flow around a NACA0012 wing. *Journal of Fluid Mechanics*, 496:63–72, 2003.

[57] J. C. R. Hunt, A. A. Wray, and P. Moin. Eddies, stream, and convergence zones in turbulent flows. Technical Report CTR-S88, Center for Turbulence Research, 1988.

[58] B. E. Husic, K. L. Schlueter-Kuck, and J. O. Dabiri. Simultaneous coherent structure coloring facilitates interpretable clustering of scientific data by amplifying dissimilarity. *PLOS One*, 14(3), 2019.

[59] A. K. M. F. Hussain. Coherent structures and turbulence. *Journal of Fluid Mechanics*, 173:303–356, 1986.

[60] G. Iacobello, S. Scarsoglio, J. G. M. Kuerten, and L. Ridolfi. Spatial characterization of turbulent channel flow via complex networks. *Physical Review E*, 98(1):013107, 2018.

[61] G. Iacobello, S. Scarsoglio, J. G. M. Kuerten, and L. Ridolfi. Lagrangian network analysis of turbulent mixing. *Journal of Fluid Mechanics*, 865:546–562, 2019.

[62] G. Iacobello, S. Scarsoglio, and L. Ridolfi. Visibility graph analysis of wall turbulence time-series. *Physics Letters A*, 382(1):1–11, 2018.

[63] R. T. Jantzen, K. Taira, K. Granlund, and M. V. Ol. Vortex dynamics around pitching plates. *Physics of Fluids*, 26:053696, 2014.

[64] J. Jeong and F. Hussain. On the identification of a vortex. *Journal of Fluid Mechanics*, 285:69–94, 1995.

[65] J. Jiménez. Machine-aided turbulence theory. *Journal of Fluid Mechanics*, 854, 2018.

[66] J. Jiménez. Monte-carlo science. *arXiv preprint arXiv:2001.09437*, 2020.

[67] J. Jiménez, A. A. Wray, P. G. Saffman, and R. S. Rogallo. The structure of intense vorticity in isotropic turbulence. *Journal of Fluid Mechanics*, 255:65–90, 1993.

[68] K. Jones, C. Dohring, and M. Platzer. Wake structures behind plunging airfoils: a comparison of numerical and experimental results. In *AIAA paper 1996-0078*, 1996.

[69] R. D. Joslin and D. Miller, editors. *Fundamentals and applications of modern flow control*. Progress in Astronautics and Aeronautics. AIAA, 2009.

[70] E. Kaiser, B. R. Noack, L. Cordier, A. Spohn, M. Segond, M. Abel, G. Daviller, and R. K. Niven. Cluster-based reduced-order modelling of a mixing layer. *Journal of Fluid Mechanics*, 754:365–414, 2014.

[71] T. Kajishima and K. Taira. *Computational fluid dynamics: Incompressible turbulent flows*. Springer, 2017.

[72] T. G. Kang and T. H. Kwon. Colored particle tracking method for mixing analysis of chaotic micromixers. *Journal of Micromechanics and Microengineering*, 14(7):891, 2004.

[73] J. Kim and P. Moin. Application of a fractional-step method to incompressible Navier–Stokes equations. *Journal of Computational Physics*, 59(2):308–323, 1985.

[74] M. M. Koochesfahani. Vortical patterns in the wake of an oscillating airfoil. *AIAA Journal*, 27(9):1200–1205, 1989.

[75] M. A. Kramer, U. T. Eden, S. S. Cash, and E. D. Kolaczyk. Network inference with confidence from multivariate time series. *Physical Review E*, 79(6):061916, 2009.

[76] A. Krishnan, R. Sujith, N. Marwan, and J. Kurths. On the emergence of large clusters of acoustic power sources at the onset of thermoacoustic instability in a turbulent combustor. *Journal of Fluid Mechanics*, 874:455–482, 2019.

[77] D. F. Kurtulus. On the unsteady behavior of the flow around NACA0012 airfoil with steady external conditions at $Re = 1000$. *International Journal of Micro Air Vehicles*, 7(3):301–326, 2015.

[78] D. F. Kurtulus. On the wake pattern of symmetric airfoils for different incidence angles at $Re = 1000$. *International Journal of Micro Air Vehicles*, 8(2):109–139, 2016.

[79] E. A. Leicht and M. E. J. Newman. Community structure in directed networks. *Physical Review Letters*, 100(11):118703, 2008.

[80] M. Lesieur and O. Metais. New trends in large-eddy simulations of turbulence. *Annual Review of Fluid Mechanics*, 28(1):45–82, 1996.

[81] R. H. Liebeck. Design of subsonic airfoils for high lift. *Journal of Aircraft*, 15(9):547–561, 1978.

[82] Y. Liu, K. Li, J. Zhang, H. Wang, and L. Liu. Numerical bifurcation analysis of static stall of airfoil and dynamic stall under unsteady perturbation. *Communications in Nonlinear Science and Numerical Simulation*, 17(8):3427–3434, 2012.

[83] J. L. Lumley. The structure of inhomogeneous turbulent flows. *Atmospheric Turbulence and Radio Wave Propagation*, 1967.

[84] L. Machiels. Predictability of small-scale motion in isotropic fluid turbulence. *Physical Review Letters*, 79(18):3411, 1997.

[85] J. C. McWilliams. The emergence of isolated coherent vortices in turbulent flow. *Journal of Fluid Mechanics*, 146:21–43, 1984.

[86] O. Métais and M. Lesieur. Statistical predictability of decaying turbulence. *Journal of the Atmospheric Sciences*, 43(9):857–870, 1986.

[87] S. Mittal and T. E. Tezduyar. Massively parallel finite element computation of incompressible flows involving fluid-body interactions. *Computer Methods in Applied Mechanics and Engineering*, 112(1-4):253–282, 1994.

[88] F. Moisy and J. Jiménez. Geometry and clustering of intense structures in isotropic turbulence. *Journal of Fluid Mechanics*, 513:111–133, 2004.

[89] Y. Morinishi, T. S. Lund, O. V. Vasilyev, and P. Moin. Fully conservative higher order finite difference schemes for incompressible flow. *Journal of Computational Physics*, 143(1):90–124, 1998.

[90] P. J. Mucha, T. Richardson, K. Macon, M. A. Porter, and J.-P. Onnela. Community structure in time-dependent, multiscale, and multiplex networks. *Science*, 328(5980):876–878, 2010.

[91] P. M. Munday and K. Taira. On the lock-on of vortex shedding to oscillatory actuation around a circular cylinder. *Physics of Fluids*, 25, 2013.

[92] M. Musolesi and C. Mascolo. A community based mobility model for ad hoc network research. In *Proceedings of the 2nd International Workshop on Multi-hop Ad Hoc Networks: From Theory to Reality*, pages 31–38. ACM, 2006.

[93] A. G. Nair, S. L. Brunton, and K. Taira. Networked-oscillator-based modeling and control of unsteady wake flows. *Physical Review E*, 97(6):063107, 2018.

[94] A. G. Nair and K. Taira. Network-theoretic approach to sparsified discrete vortex dynamics. *Journal of Fluid Mechanics*, 768:549–571, 2015.

[95] A. G. Nair, C.-A. Yeh, E. Kaiser, B. R. Noack, S. L. Brunton, and K. Taira. Cluster-based feedback control of turbulent post-stall separated flows. *Journal of Fluid Mechanics*, 875:345–375, 2019.

[96] O. Nelles. *Nonlinear system identification: From classical approaches to neural networks and fuzzy models*. Springer Science & Business Media, 2013.

[97] D. A. Nelson and G. B. Jacobs. DG-FTLE: Lagrangian coherent structures with high-order discontinuous-Galerkin methods. *Journal of Computational Physics*, 295:65–86, 2015.

[98] D. H. Neuhart and O. C. Pendergraft Jr. A water tunnel study of gurney flaps. *NASA Technical Memorandum 4071*, 1988.

[99] M. E. J. Newman. The structural and function of complex networks. *SIAM Review*, 45(2):167–256, 2003.

[100] M. E. J. Newman. Analysis of weighted networks. *Physical Review E*, 70(5):056131, 2004.

[101] M. E. J. Newman. Fast algorithm for detecting community structure in networks. *Physical Review E*, 69(6):066133, 2004.

[102] M. E. J. Newman. Finding community structure in networks using the eigenvectors of matrices. *Physical Review E*, 74(3):036104, 2006.

[103] M. E. J. Newman. Modularity and community structure in networks. *Proceedings of the National Academy of Sciences*, 103(23):8577–8582, 2006.

[104] M. E. J. Newman. *Networks: An introduction*. Oxford University Press, 2010.

[105] M. E. J. Newman. Spectral methods for community detection and graph partitioning. *Physical Review E*, 88(4):042822, 2013.

[106] M. E. J. Newman, A.-L. Barabási, and D. J. Watts. *The structure and dynamics of networks*. Princeton University Press, 2011.

[107] M. E. J. Newman and M. Girvan. Finding and evaluating community structure in networks. *Physical Review E*, 69(2):026113, 2004.

[108] P. K. Newton. *The N-vortex problem: Analytical techniques*. Springer Science & Business Media, 2013.

[109] A. Ongoren and D. Rockwell. Flow structure from an oscillating cylinder part 2: Mode competition in the near wake. *Journal of Fluid Mechanics*, 191:225–245, 6 1988.

[110] D. Oshiyama, D. Numata, and K. Asai. Lift-enhancing mechanism of mini flaps at low reynolds number. In *The Japan Society for Aeronautical and Space Science 2015-D12-1087*, 2015.

[111] E. Otte and R. Rousseau. Social network analysis: a powerful strategy, also for the information sciences. *Journal of Information Science*, 28(6):441–453, 2002.

[112] J. M. Ottino. Mixing, chaotic advection, and turbulence. *Annual Review of Fluid Mechanics*, 22(1):207–254, 1990.

[113] P. Pons and M. Latapy. Computing communities in large networks using random walks. *Journal of Graph Algorithms and Applications*, 10(2):191–218, 2006.

[114] J. Reichardt and S. Bornholdt. Detecting fuzzy community structures in complex networks with a potts model. *Physical Review Letters*, 93(21):218701, 2004.

[115] J. Reichardt and S. Bornholdt. Statistical mechanics of community detection. *Physical Review E*, 74(1):016110, 2006.

[116] M. P. Rockwood, K. Taira, and M. A. Green. Detecting vortex formation and shedding in cylinder wakes using lagrangian coherent structures. *AIAA Journal*, 55(1):15–23, 2016.

[117] M. Rubinov and O. Sporns. Complex network measures of brain connectivity: uses and interpretations. *Neuroimage*, 52(3):1059–1069, 2010.

[118] P. G. Saffman. *Vortex dynamics*. Cambridge university press, 1992.

[119] M. Salathé and J. H. Jones. Dynamics and control of diseases in networks with community structure. *PLOS Computational Biology*, 6(4):e1000736, 2010.

[120] S. Scarsoglio, F. Cazzato, and L. Ridolfi. From time-series to complex networks: application to the cerebrovascular flow patterns in atrial fibrillation. *Chaos: An Interdisciplinary Journal of Nonlinear Science*, 27(9):093107, 2017.

[121] K. L. Schlueter-Kuck and J. O. Dabiri. Coherent structure colouring: identification of coherent structures from sparse data using graph theory. *Journal of Fluid Mechanics*, 811:468–486, 2017.

[122] P. J. Schmid. Dynamic mode decomposition of numerical and experimental data. *Journal of Fluid Mechanics*, 656:5–28, 2010.

[123] P. J. Schmid, A. García-Gutierrez, and J. Jiménez. Description and detection of burst events in turbulent flows. In *Journal of Physics: Conference Series*, volume 1001, page 012015, 2018.

[124] E. Ser-Giacomi, V. Rossi, C. López, and E. Hernández-García. Flow networks: a characterization of geophysical fluid transport. *Chaos: An Interdisciplinary Journal of Nonlinear Science*, 25(3):036404, 2015.

[125] J. Singh, R. Belur Vishwanath, S. Chaudhuri, and R. I. Sujith. Network structure of turbulent premixed flames. *Chaos: An Interdisciplinary Journal of Nonlinear Science*, 27(4):043107, 2017.

[126] R. S. Spencer and R. M. Wiley. The mixing of very viscous liquids. *Journal of Colloid Science*, 6(2):133–145, 1951.

[127] O. Sporns. The human connectome: a complex network. *Annals of the New York Academy of Sciences*, 1224(1):109–125, 2011.

[128] T. Suzuki, H. Ji, and F. Yamamoto. Unsteady PTV velocity field past an airfoil solved with DNS: Part 1. Algorithm of hybrid simulation and hybrid velocity field at $Re \approx 10^3$. *Experiments in Fluids*, 47(6):977–994, 2009.

[129] K. Taira, S. L. Brunton, S. T. M. Dawson, C. W. Rowley, T. Colonius, B. J. McKeon, O. T. Schmidt, S. Gordeyev, V. Theofilis, and L. S. Ukeiley. Modal analysis of fluid flows: an overview. *AIAA Journal*, pages 4013–4041, 2017.

[130] K. Taira and T. Colonius. The immersed boundary method: a projection approach. *Journal of Computational Physics*, 225:2118–2137, 2007.

[131] K. Taira and T. Colonius. Three-dimensional flows around low-aspect-ratio flat-plate wings at low reynolds numbers. *Journal of Fluid Mechanics*, 623:187–207, 2009.

[132] K. Taira, M. S. Hemati, S. L. Brunton, Y. Sun, K. Duraisamy, S. T. M. Bagheri, Shervin amd Dawson, and C.-A. Yeh. Modal analysis of fluid flows: applications and outlook. *AIAA Journal*, pages 998–1022, 2020.

[133] K. Taira, A. G. Nair, and S. L. Brunton. Network structure of two-dimensional decaying isotropic turbulence. *Journal of Fluid Mechanics*, 795:R2, 2016.

[134] R. Tibshirani. Regression shrinkage and selection via the lasso. *Journal of the Royal Statistical Society. Series B (Methodological)*, pages 267–288, 1996.

[135] E. A. Variano, J. H. McCoy, and H. Lipson. Networks, dynamics, and modularity. *Physical Review Letters*, 92(18):188701, 2004.

[136] C. H. K. Williamson and A. Roshko. Vortex formation in the wake of an oscillating cylinder. *Journal of Fluids and Structures*, 2:355–381, 1988.

[137] Z. Xie, X. Li, and X. Wang. A new community-based evolving network model. *Physica A: Statistical Mechanics and its Applications*, 384(2):725–732, 2007.

[138] H. Yu, K. Kanov, E. Perlman, J. Graham, E. Frederix, R. Burns, A. Szalay, G. Eyink, and C. Meneveau. Studying lagrangian dynamics of turbulence using on-demand fluid particle tracking in a public turbulence database. *Journal of Turbulence*, (13):N12, 2012.

[139] X. Zhang and M. E. J. Newman. Multiway spectral community detection in networks. *Physical Review E*, 92(5):052808, 2015.

[140] X. Zhu, M. Gerstein, and M. Snyder. Getting connected: analysis and principles of biological networks. *Genes & Development*, 21(9):1010–1024, 2007.